# IMPEDANCE-MISMATCH EXPERIMENTS USING LASER-DRIVEN SHOCKS

By

Gordon S. Y. Chiu

B.A.Sc., The University of British Columbia, 1986

A THESIS SUBMITTED IN PARTIAL FULFILLMENT OF

THE REQUIREMENTS FOR THE DEGREE OF

MASTER OF APPLIED SCIENCE

in

THE FACULTY OF GRADUATE STUDIES

DEPARTMENT OF PHYSICS

We accept this thesis as conforming

to the required standard

THE UNIVERSITY OF BRITISH COLUMBIA

September 1988

In presenting this thesis in partial fulfilment of the requirements for an advanced degree at the University of British Columbia, I agree that the Library shall make it freely available for reference and study. I further agree that permission for extensive copying of this thesis for scholarly purposes may be granted by the head of my department or by his or her representatives. It is understood that copying or publication of this thesis for financial gain shall not be allowed without my written permission.

Department of PHYSICS

The University of British Columbia
1956 Main Mall
Vancouver, Canada
V6T 1Y3

Date Sept 14, 1988.

## Abstract

A series of impedance-mismatch experiments with aluminum-gold targets has been performed. These experiments are used to probe the equation of state (EOS) of gold at high pressure. By measuring the shock breakout time from the target rear surface, the shock trajectory is determined and found to be in good agreement with equation of state predictions. In addition, temperatures derived from temporally resolved luminescence measurements of the shocked target rear surface are compared with two different equation of state theoretical models. Our results indicate that whereas the SESAME (from Los Alamos National Laboratory) EOS seems to overestimate the shock temperature, the equation of state of gold which incoporated both the solid and liquid phases gives much closer agreement with observations. The measurements of gold at a shock pressure of $\sim$6 Mbar and temperature of $\sim$17500 K also represent the first study of gold under shock melting.

## Table of Contents

## List of Tables

## List of Figures

## Acknowledgement

I would like to thank my supervisor, Dr. Andrew Ng for his guidance in the present project and for providing an excellent experimental facility. My indebtedness is to Dr. B.K.Godwal for his many helpful suggestions and assistance in theoretical calculations in this thesis. I am especially grateful to Luiz Da Silva, who has helped me greatly in every phase of the experimental work and thesis preparation. To the other members and visitors of the plasma group, I say thank you for providing lively discussions and insightful comments, work related or otherwise.

This work is supported by the Natural Sciences and Engineering Research Council of Canada.

# Chapter 1

# Introduction

## 1.1 Introduction to High Pressure Research

The generation of high pressure ($10^6$ atmosphere regime) in matter not only finds immediate application in driving implosions in inertial confinement fusion [1, 2], where the thermonuclear fuel must be brought into an extreme state of density and temperature (brought about by high pressure compression) to ignite and sustain the fusion reactions, but also can be of fundamental interest in the study of equations of state (EOS) of matter at high pressure[3], the determination of structural phase transitions in crystals[4], and the investigations of intermolecular forces, electronic, chemical, and optical properties of materials under extreme conditions[5]. Many interesting physical phenomena such as s-d electronic transfer leading to insulator-metallic transition[6, 7], or shock melting from solid to liquid at high pressure[8], have remained mostly unexplored and not well understood (for example, Shaner in reference [9] discusses the various difficulties besetting the measurements in high pressure melting). On the other hand, experimental results are critically needed to resolve diverging predictions among contending EOS theories as well as to extend and to establish the range of applicability of existing calculational techniques. Hence high pressure study can be seen to be of immense importance in both applied and theoretical studies.

The basic principle for obtaining high pressure in various dynamic methods[10], in

contrast to the static techniques (such as the diamond anvil cell[11]), involves the introduction of a rapid impulse (shock wave) through:

1. the denonation of explosive systems, either chemical[12, 13, 14, 15] or nuclear[16, 17],

2. hypervelocity impact using a high-speed projectile from a single or two-stage light-gas gun[18],

3. the energy deposition by an intense ion beam[19],

4. the absorption of an intense pulse of radiation provided by a high-power laser[20].

Generally speaking, the main advantage of dynamic over static techniques is that higher pressure can be attained. This is because the pressure achieved in diamond anvil cells will be ultimately restricted by the plastic deformation limit of diamonds. However, for dynamic pressure studies unique and fast diagnostics (e.g. sub-nanosecond resolution in laser-driven experiments) must also be developed. In addition, dynamic methods are usually much more costly in both capital and operation aspects.

A brief discussion on the merits and shortcomings of the various dynamic methods is in order here. The use of chemical explosives has been one of the earliest methods in high pressure generation[12, 13], but the attainable pressures have been limited to $\sim$10 Mbar (1 Mbar = $10^6$ atmospheres) in metals[15]. Underground nuclear explosions[3, 16, 17] offer the possibility to achieve record-setting pressures (readily exceeding 100 Mbar, and recently, pressures of >4000 Mbar in aluminum[21] have been reported) with good accuracy (<5%), although this method is vastly expensive and obviously inaccessible to many researchers. On the other hand, the two-stage light-gas guns[22] have produced the most precise measurements ($\leq$ 1% accuracy in pressure[18]), but the pressure attained is somewhat limited (up to $\sim$5 Mbar[3]). While heavy ion beams are projected to be capable

of producing dynamic pressure of over 100 Mbar[23], yet no practical demonstration has been performed. Lastly, laser-driven shock waves have been shown to be eminently able to span pressures in the "intermediate" region (tens to hundreds of Mbars[24, 25]) previously inaccessible by the more conventional means, thus bridging the gap between the low presssure region appropriate to gas guns/chemical explosives and the high pressure region characteristic of nuclear explosions. Furthermore, because of its high repetition rate and relative ease of operation, laser has become the sole means of generating pressures in the intermediate region in laboratory-scaled experiments, although the uncertainties in the measurements can be significant ($\geq 10\%$).

As we will be using the laser option in the work of the present thesis, we will elaborate further on the versatility of the use of laser-driven shock waves. A great majority of researches in the past decades have been directed towards understanding the many aspects in laser-matter interactions such as laser absorption efficiency, mass ablation rate, target preheat mechanisms, or thermal transport properties, and hence arriving at the optimal conditions for laser-driven fusion[26, 27, 28, 29]. Nevertheless it is soon recognized that the ability of laser-driven shock waves to generate high pressures is also ideal for equation of state studies of materials at extreme conditions of pressure and density[24, 30]. In addition, electrical properties such as the potential difference between surfaces of deformed dielectrics caused by the motion of a shock wave (this is called shock polarization[31]), or the electronic conductivity in dense plasma[32], have also been studied using laser-driven shock waves. More recent experiments of interest in condensed matter physics and atomic physics, all using laser-driven shocks to achieve the desired material state, include the measurements of lattice compressions and stresses in silicon[33], the temporal evolution of the K-absorption edge in shock compressed potassium chloride[34], or the short range ion correlation effects in aluminum plasma[35].

Finally we will conclude the introductory section by discussing the phenomenon of

shock melting, as it represents one of the principal areas of studies in this thesis. Shock wave propagation in a material leads to the compression and heating of the material above solid density and ambient temperature, and sometimes this heating is sufficient to cause the material to melt. Kormer et al.[36] have suggested the measurement of shock temperature to detect the onset of melting and to resolve different predictions forwarded by solid and liquid states EOS theories. For example, the observations of shock melting along the Hugoniot in materials have been previously reported. The earliest studies of Kormer[36] measured the brightness temperature of the shock front and determined the high-pressure melting curve in a number of transparent alkali halides (NaCl, KBr, LiF, etc.). The Livermore[37] and Los Alamos group[38] have calculated the melting behavior on the Hugoniot of a number of alkali metals as well as aluminum, and have experimentally determined the shock melting range in aluminum through sound speed measurements. The recent investigations of Radousky et.al.[39] also use shock temperature measurements to determine the onset of melting in CsI. In particular, they found that their data were sufficiently sensitive detect an inadequacy in the solid Hugoniot calculation, and have shown the validity of using a liquid theory in the melting regime. Hence, the acquisation of experimental data is crucial in helping to differentiate between the predictions of different theories.

## 1.2 Thesis Objective

The principal aim of this thesis is to utilize intense laser pulses to generate strong shock waves for equation of state investigations in high-Z materials. As an example, we

will focus on the behavior of gold at high pressure and specifically, the process of shock melting. From time-resolved measurements of shock-induced luminous emissions, we will determine the temperature of gold at ~6 Mbar, above its predicted melting transition at ~2 Mbar. The result will be used to assess existing equation of state models and to provide an experimental basis for new models.

A second but strongly related objective is to employ the impedance-mismatch technique[12, 14, 15, 22] in the study of high-Z materials using laser-driven shock waves. The impedance-mismatch technique involves the production of a shock wave in a low-Z (low density and low acoustic impedance) material, which then propagates into the high-Z (high density and high acoustic impedance) material of interest. In this study, gold and aluminum have been chosen as the high-Z and low-Z materials respectively. We will demonstrate the advantages of this technique, namely, pressure enhancement and reduction of radiative preheat. We will examine the proper design of an impedance-mismatched target and identify the critical criterion for optimal pressure generation in the high-Z material of interest.

## 1.3 Thesis Outline

This thesis is organized as follows: Chapter 2 gives a review of the theory on shock waves and the technique of shock production by impedance mismatch. Chapter 3 describes the experimental facility, diagnostics, and the experimental setup. The experimental results and comparison with computer simulations will be presented in chapter 4. Finally, the major conclusions are summarized in chapter 5.

# Chapter 2

# Theory of Laser-driven Shocks

## 2.1 Shock Generation by Laser-Driven Ablation in Solids

The process for generating laser-driven shocks has been examined in details in references [1] and [2]. Here we shall briefly review the three principal physics processes involved:

1. laser energy absorption in a laser-heated target,
2. electron thermal conduction which carries the heat flux from the absorption region into the target interior, effecting ablation, and
3. shock wave generation by the outward expansion of the ablated material.

### 2.1.1 Laser Energy Deposition

Figure 2.1 shows a schematic diagram of a laser-irradiated solid target, where the outer layer of the target is heated by an energy absorption mechanism known as *inverse bremsstrahlung*[40], or free-free absorption. This process can be visualized as electrons oscillating in the electric field of the incident laser light and thereby absorbing the energy of the photon. The electrons subsequently transfer their energies to the rest of the target (i.e. ions) via electron-ion collisions. In this manner, particles in the target absorb the laser energy and become heated, ionized and expand into the vacuum, forming a low density blow-off plasma, called the *corona*. For short wavelength ($\leq 1$ $\mu$m) laser radiation

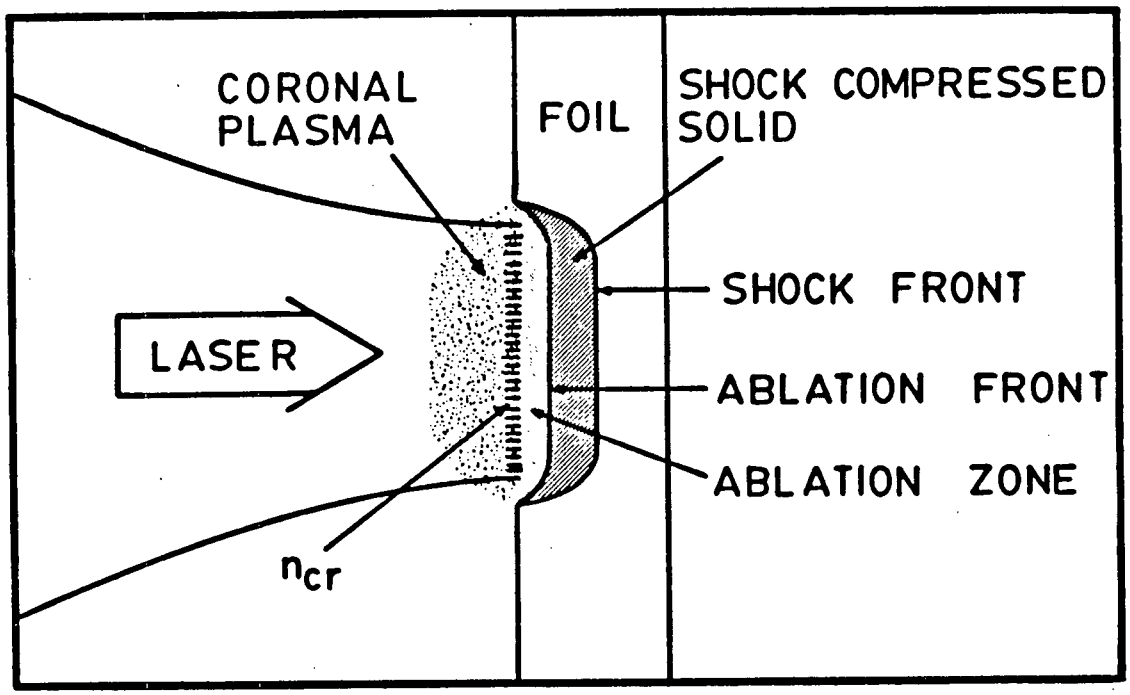


Figure 2.1: Schematic diagram of a laser-driven shock

this process is the dominant absorption mechanism. The laser energy can be absorbed up to the critical density surface where the electron oscillation frequency equals the frequency of the laser radiation and the laser light is reflected. Accordingly, the critical density $n_{crit}$ is defined by

$$n_{crit} = \frac{\omega_L^2 \epsilon_0 m}{e^2} \qquad [MKS \quad units] \tag{2.1}$$

where $\omega_L$ is the laser frequency, $m$ and $e$ are the electron mass and charge respectively, and $\epsilon_0$ is the permittivity of space. Since the plasma density scale length ($l=(\frac{1}{n}\frac{\partial n}{\partial x})^{-1}$, where $n$ is the electron density) in the corona is invariably much larger than the laser wavelength[40], and since the electron-ion energy transferring process becomes more and more efficient as electron density increases (the electron-ion collisional frequency scales approximately linearly with electron density[40]), therefore essentially all of the laser energy is absorbed in the corona before it reaches the critical surface. Consequently, the coronal plasma is very hot ($\sim$ 1 keV)[41].

### 2.1.2 Electron Thermal Conduction

The laser energy absorbed on the surface of the target is transported inward due to large temperature gradient between the hot corona and the cold interior of the target. The deposition of this intense heat flux in the so-called *conduction* or *ablation zone* (see Figure 2.1) causes the target material to be ablated (i.e., vaporized from the solid) which then expands rapidly outward into the corona. The heat conduction is mainly carried out by the electrons, first studied by Spitzer and Härm[42]. They assumed electron thermal conduction to follow the classical Fourier heat law,

$$Q_e = -\kappa_e \cdot \nabla T_e \tag{2.2}$$

where $\kappa_e$ is the Spitzer thermal conductivity which is of the form[43]

$$\kappa_e = 1.955 \cdot 10^{-9} \frac{0.095(Z + 0.24)}{1 + 0.24Z} \frac{T_e^{5/2}}{Z \ln \Lambda} \tag{2.3}$$

where $Z$ is the material atomic number, $T_e$ is the electron temperature, and $\ln \Lambda$ is the Coulomb logarithm. As a result, the specific heat flux will be

$$H_e = -\frac{1}{\rho} \nabla \cdot \kappa_e \nabla T_e \tag{2.4}$$

where $\rho$ is the density.

It has been observed that at high enough intensity ($\geq 10^{14}$ W/cm$^2$) the Spitzer-Härm transport model breaks down[27, 44, 45], so that the actual heat conduction is much less than predicted. (This is because for large temperature gradient, equation (2.3) predicts an excessively large heat flux.) This decrease in heat flux is called electron thermal flux inhibition, and one usually remedies it artifically in simulations by assigning a "flux-limiter" $f$, so that the actual flux $H_a = f \cdot H_e$ is no more than a fraction of the Spitzer flux. Furthermore, at high intensities energetic electrons called suprathermal or hot electrons[28, 46] with energies much greater than the thermal electrons of the plasma corona are produced. These suprathermal electrons represent another means of energy transport in addition to the diffusive heat flow discussed above. These electrons have long mean free paths and will "preheat" the target (i.e. heat up the target before the shock arrives). These two aspects will be further addressed in §2.5.2 and it will be shown that they are negligible in our experiments in §4.1.1.A.

### 2.1.3 Shock Wave Generation

The outward expansion of the ablated material from the ablation front gives rise to a large outward momentum flux. By momentum conservation, this produces a large ablation pressure which drives a shock wave into the interior of the solid target (Figure 2.1).

So long as the ablation pressure increases (due to the increasing laser intensity, for example, in the rising edge of a Gaussian pulse), shock waves of increasing amplitudes will be launched into the target. Now the first launched shock wave travels at slightly exceeding the speed of sound, and being a compressional disturbance, will compress the solid a little. The second stronger shock wave will therefore travel near the corresponding sound speed of the compressed region, which is greater than that in an undisturbed medium, and will recompress the target still further. (The sound speed $c \equiv \sqrt{\partial P/\partial \rho}$ ($P, \rho$ is the pressure and density) equals, in the case of an ideal adiabatic gas for example, $\sqrt{\gamma P/\rho}$, where $\gamma$ is the ratio of specific heat. Hence $c = c_0(\rho/\rho_0)^{\gamma-0.5}$ ($\rho_0, c_0$ is some reference density and corresponding sound speed) $\propto \rho^{\gamma-0.5} = \rho^{1.17}$ for a monatomic gas.) Evidently, the latter waves, propagating at higher speeds, will tend to catch up with the preceeding ones. This leads to a "steepening" of the wave front, or the coalescence of a sequence of multiple shock waves into a single steady shock front. The compressive effects of the individual shock waves also accumulate, and this shock front is characterized by a sharp discontinuity in pressure, density, and temperature between the shocked and unshocked regions.

## 2.2 The Hugoniot

Consider a planar, steady state strong shock wave and further assume that the medium ahead of the shock is at rest whereas the state behind the shock is uniformly compressed as illustrated in Figure 2.2. Then, conservation of mass, momentum, and energy across the shock front in the laboratory frame leads to the Rankine-Hugoniot

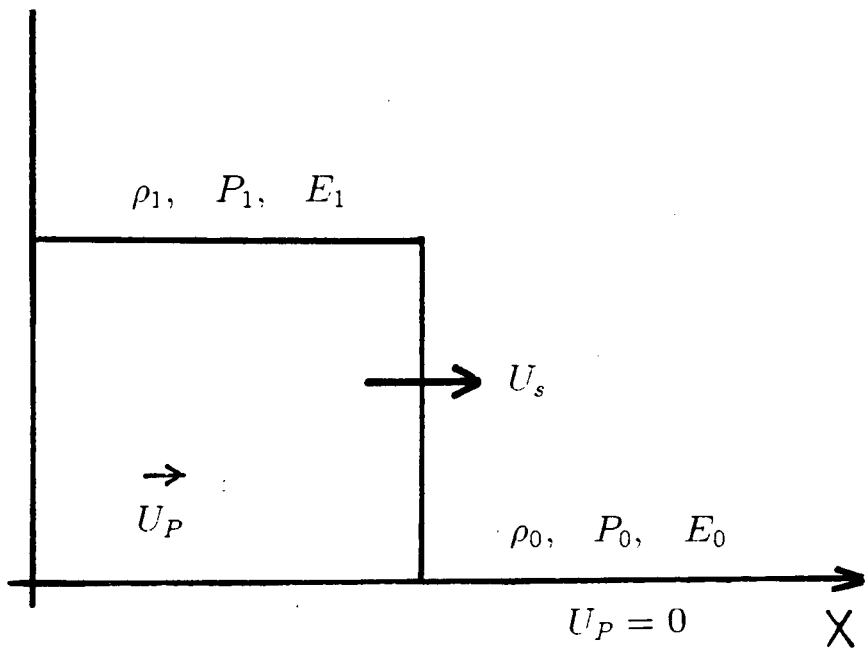


Figure 2.2: An illustration of the shocked and unshocked regions

equations (see e.g.[47, 48]):

$$\rho_0 U_S = \rho_1 (U_S - U_P) \tag{2.5}$$

$$P_1 - P_0 = \rho_0 U_S U_P \tag{2.6}$$

$$E_1 - E_0 = 1/2(P_1 + P_0)(1/\rho_0 - 1/\rho_1) \tag{2.7}$$

where $\rho$, $P$, and $E$ are the density, pressure and internal energy respectively. The subscripts 0 and 1 denote the unshocked and shocked regions, while $U_S$ and $U_P$ are the shock wave velocity and the particle velocity in the compressed region. In the limiting case when $P_1 \gg P_0$, equation (2.6) reduces to

$$P_1 = \rho_0 U_S U_P \tag{2.8}$$

which is a straight line on the $P$ vs $U_P$ plane with slope $\rho_0 U_S$. This condition is easily satisfied when $P_1$ is of the order of Mbar while $P_0$ is at atmospheric pressure in our experiment.

Given an initial condition (e.g. $\rho_0, P_0$, and $P_1$, or some other shock parameter describing the strength of the shock wave), there are five unknown parameters ($\rho_1, E_0, E_1, U_S, U_P$) and three equations (Eqs. (2.5) to (2.7)). Therefore two quantities need to be measured experimentally in order to specify completely the thermodynamical state in the shocked region. For example, the frequently measured quantities in a hypervelocity impact experiment are the shock speed and particle speed. In laser-driven shock experiments, the shock speed and temperature have been measured[49]. Alternatively, if the equation of state (such as $E = E(\rho, P)$) of the material is known or can be calculated, then one can calculate all the unknown quantities. Anyhow, a set of five shock parameters ($\rho_1, P_1, E_1, U_S, U_P$) corresponds to a final state of a shock-compressed material, and the locus of the final states that can be reached by employing shock waves of different strength from the same initial state, plotted using any two of the five shock parameters, is known

as the shock adiabat or the *Hugoniot* curve. That particular curve for which the material is initially at standard temperature (0 K) and pressure (1 bar) is called the principal Hugoniot.

The principal Hugoniots of aluminum using various shock parameters are presented in Figures 2.3 and 2.4. We note the essentially linear relationship between $U_S$ and $U_P$[47, 48]. For aluminum, it is[50]

$$U_S = 0.58 + 1.22U_P \tag{2.9}$$

where both $U_S$ and $U_P$ are given in $10^6$ cm/s. In Figure 2.4(b) the principal Hugoniot of gold is also included as a comparison to that of aluminum. These data are all taken from the SESAME library (details are presented below in §2.4.1).

## 2.3 The Impedance-Mismatch Technique

The impedance-mismatch technique has been variously called the reflection method, the deceleration method[15], or a non-symmetric impact in gas gun experiments[22]. We shall restrict our discussions of this technique as it applies to laser-driven shock wave studies, although it is obviously not limited to laser application[3, 15, 17]. The impedance-mismatch technique refers to the propagation of a shock wave through a target bound together by two (or more) layers of materials of differing shock impedances. In general, the quantity $\rho v$ represents the characteristic impedance of a material, where $\rho$ is the density of the material and $v$ the propagation velocity of the distortional wave through the material. For example, if one replaces $v$ by the sound speed $c$, then $\rho c$ is known as the acoustic impedance, and if one replaces $v$ by $U_S$, the resultant quantity

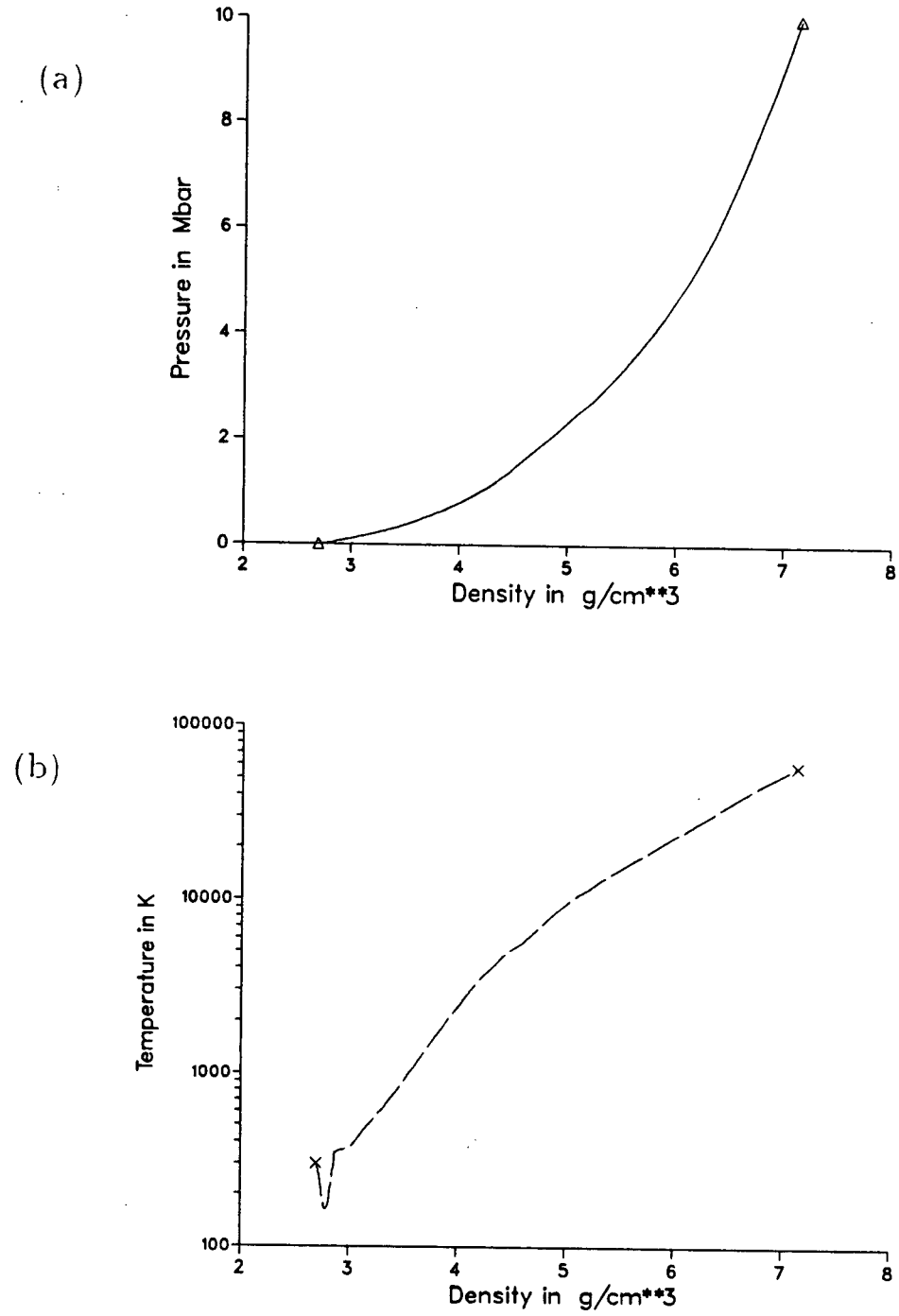


Figure 2.3: The aluminum principal Hugoniot in the (a) $P$ vs $\rho$ plane, and (b) $T$ vs $\rho$ plane, as given in SESAME.

(a)

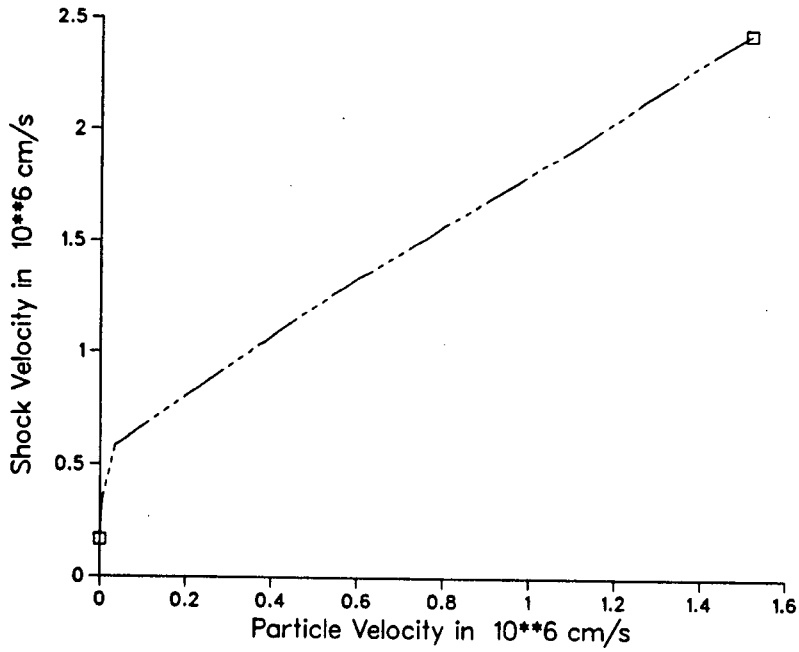


(b)

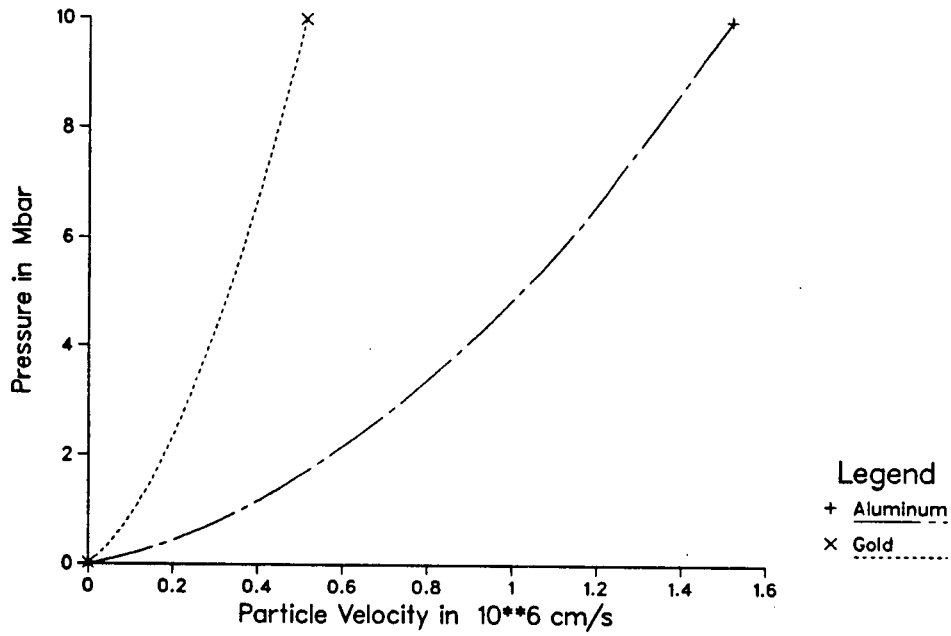


Figure 2.4: The aliminum principal Hugoniot in the (a) $U_P$ vs $U_S$ plane, and (b) $U_P$ vs $P$ plane. Also included in (b) is the principal Hugoniot of gold. Data are from SESAME.

$\rho U_S$ is known as the *shock impedance*. As mentioned in §2.2, it is generally necessary to measure two independent shock variables in order to determine the Hugoniot state of the shocked medium. On the other hand, for the impedance-mismatch technique involving two different materials, the Hugoniot of one material (the sample) can be determined from measurements of only one shock parameter if the equation of state of the other material is known. The latter then serves as a refernence standard. In the context of equation of state studies, a single Hugoniot is by itself insufficient to describe the complete EOS of a material; nevertheless, it serves as a good validating mechanism for theoretical EOS claculations and also as a useful empirical relation at high pressure.

In an impedance-mismatch experiment, the laser generated shock often, though not necessarily, first passes through the standard material and then into the adjacent sample of interest as illustrated in Figure 2.5. In close analogy to other compressional disturbances (see e.g. [51]), the shock impedance can be used to determine the behavior of a shock pressure pulse at the interface where the two materials are joined together. For the laser-driven shock wave propagating through the standard into the sample, when it reaches the interface, it will simultaneously generate a backward-moving, reflected wave into the standard as well as a forward-moving, transmitted wave into the sample. One can then deduce the shock property of the sample material as follows. Assuming again the propagation of a planar and steady shock front, there are a total of ten unknowns ($\rho, P, E, U_P$, and $U_S$ for each of the two materials). Applying the matching conditions of pressure and particle velocity at the interface of the two materials reduces the number of unknowns to eight. In addition, there are three conservation equations (Eqs. (2.5) to (2.7)) governing each of the shocked states in the standard and the sample, plus the EOS for the standard material, giving a total of seven equations. Therefore one needs to measure only one parameter, usually a shock velocity in either one of the two materials, in order to completely specify the final shock-compressed thermodynamic states of both

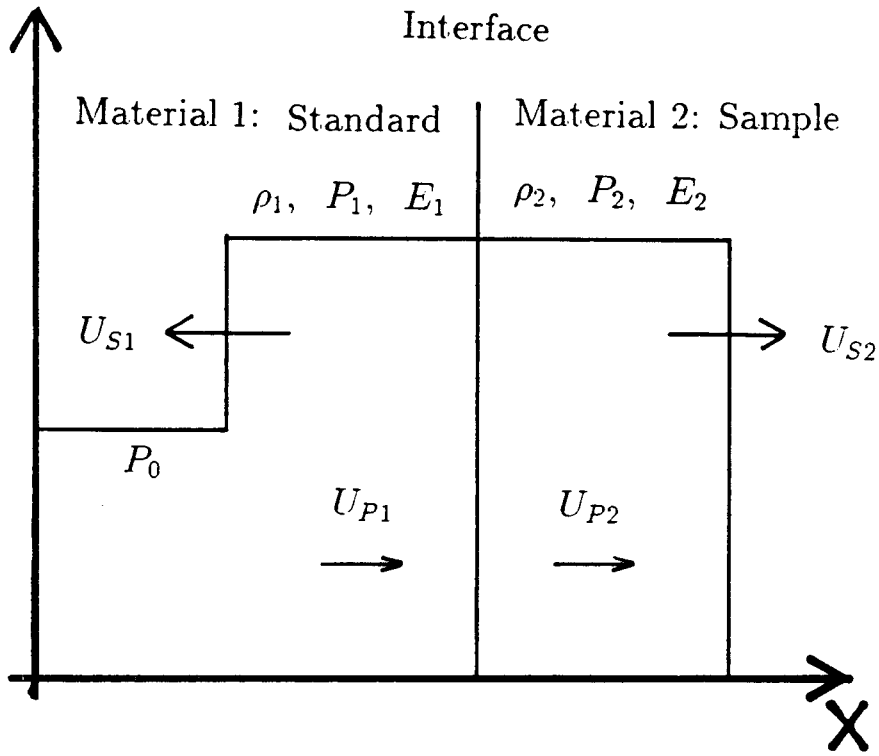


Interface Matching Conditions:

$$P_0 + P_1 = P_2$$

$$U_{P1} = U_{P2}$$

Figure 2.5: Shock propagation and parameters in an impedance-mismatched target

materials.

### 2.3.1 Pressure Enhancement

As mentioned before, a reflected wave and a transmitted wave are generated at the interface of the target. Whether the reflected and transmitted waves are either a rarefaction or second shock depends upon the relative shock impedances of the two materials. Specifically, if $P_0$ is the amplitude of the incoming pressure pulse, and $P_1$ and $P_2$ those of the reflected and transmitted pulses (refer to Figure 2.5) respectively, then[52]

$$P_1 = \frac{(\rho U_S)_2 - (\rho U_S)_1}{(\rho U_S)_2 + (\rho U_S)_1} P_0 \tag{2.10}$$

$$P_2 = \frac{2(\rho U_S)_2}{(\rho U_S)_2 + (\rho U_S)_1} P_0 \tag{2.11}$$

where the subscripts 1,2 denote the regions in front and back of the interface. In any case, the resultant pressure and particle velocity must be continuous across the interface.

It can be seen that pressure enhancement in the sample can be achieved by using a standard which has a lower shock impedance than that of the sample (so that $2(\rho U_S)_2$ is greater than $(\rho U_S)_2 + (\rho U_S)_1$ in equation (2.11).) The transmitted shock pressure can therefore be greatly increased using this technique. The validity of such pressure enhancement was first demonstrated in laser-driven shocks by Vesser et al.[30] with aluminum-gold targets using 1.06 $\mu$m laser irradiation. Subsequent studies include those of Holmes et al.[53] for aluminum-copper targets irradiated with 1.06 $\mu$m laser light and Cottet et al.[25] for 0.26 $\mu$m laser radiation on aluminum-gold targets.

The amount of pressure enhancement can be easily calculated from the Hugoniot of the standard by utilizing the mirror-reflection method, and is graphically illustrated in Figure 2.6. The incoming shock first produces an intermediate state at the point $(U_{P0}, P_0)$

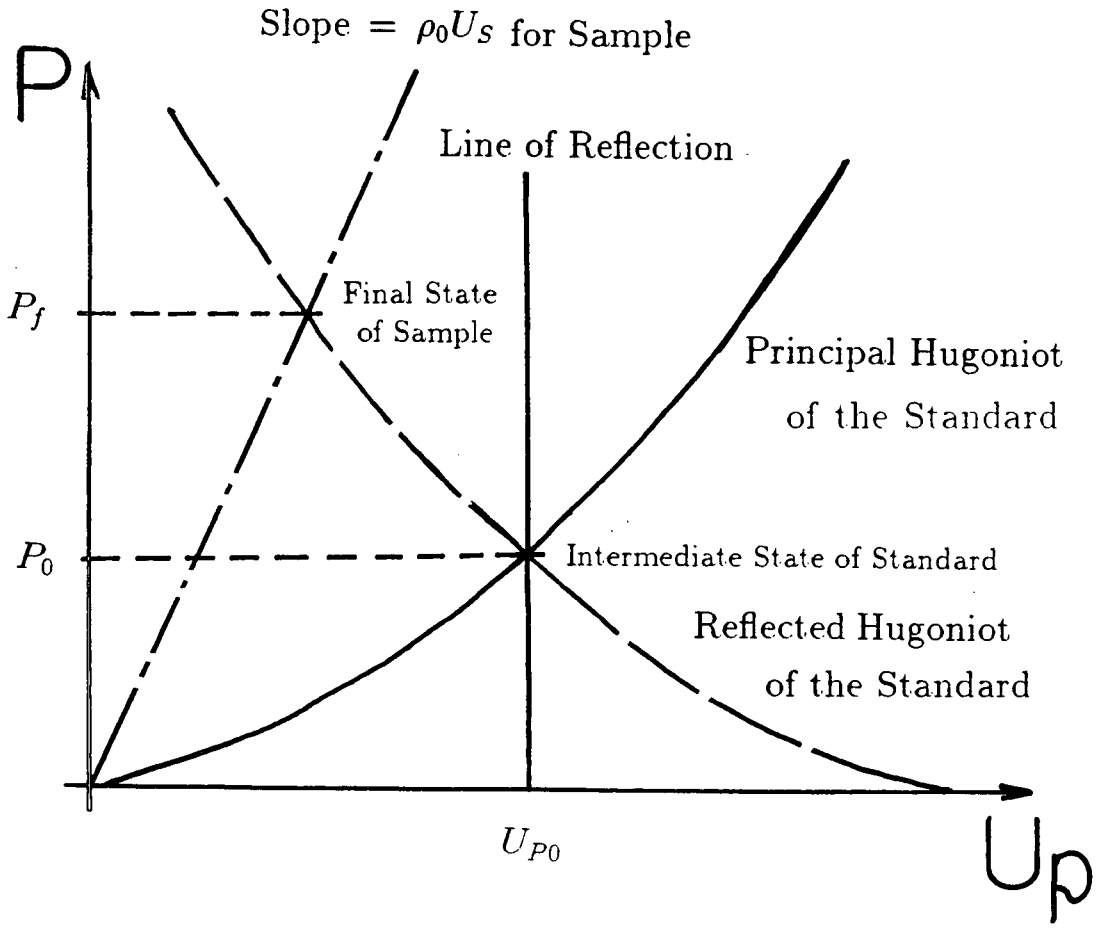


Figure 2.6: The calculation of pressure in the sample using the mirror-reflection method. The slope of the straight line involves the measurement of the shock velocity $U_S$ in the sample.

in the standard. The reflected shock then takes the standard from the new initial state $(U_{P0}, P_0)$ to a final state on the reflected Hugoniot. This reflected Hugoniot can be constructed on the pressure-particle velocity plane from a mirror reflection of the principal Hugoniot of the standard about a vertical line through the point $(U_{P0}, P_0)$[25, 48]. The point of intersection of the reflected Hugoniot of the standard and the straight line with slope $\rho_0 U_S$ (where $\rho_0$ is the initial density of the sample as governed by equation (2.8)) assuming that $U_S$ is measured for the sample, constitutes the state reached in the sample. The method so described is an approximate one since the reflected shock in the standard originates from the point $(U_{P0}, P_0)$ rather than from normal conditions. Such re-shocked states are more isentropic than the states attained in a single shock[3, 48, 54]. However, the difference is negligibly small for low values of $P_0$ ($\leq$ several Mbar[17]). Of course, the method becomes exact if one takes the reflected Hugoniot to be that which originates from the intermediate point $(U_{P0}, P_0)$ but this involves the knowledge of another Hugoniot curve.

Alternatively, one can assume knowledge of the principal Hugoniot of the sample material and uses the experiment for verification. Under such assumption, the final state achieved in the sample is given by the intersection of the reflected Hugoniot of the standard and the principal Hugoniot of the sample as indicated in Figure 2.7. The intersection point then gives the pressure $P_f$ and particle velocity $U_{Pf}$ in the sample, which can be used to correlate with experiments. For example, the shock speed in the sample can be calculated using a relation similar to Eq. (2.9), and can be compared with measurements.

### 2.3.2 Reduction of Radiative Preheat

The impedance-mismatch method is doubly attractive in EOS studies of high-Z materials since it reduces the undesirable effect of radiative preheating ahead of the shock

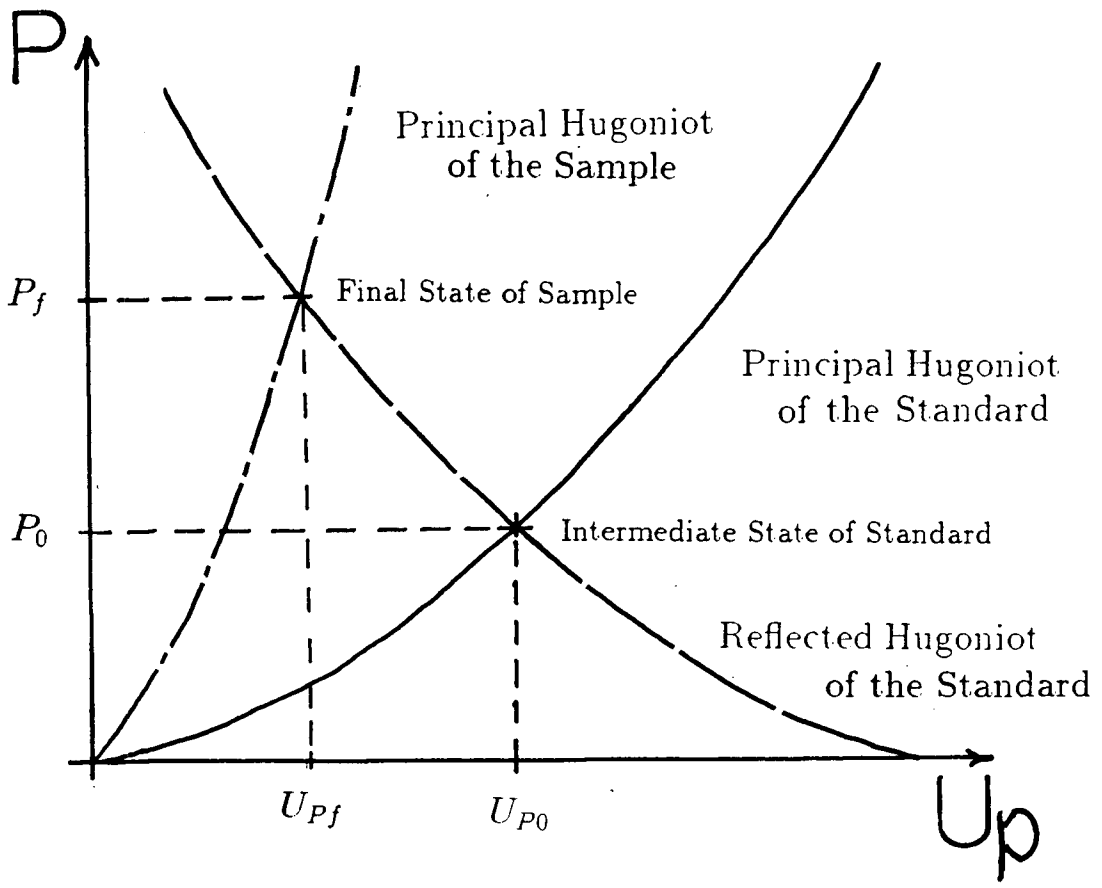


Figure 2.7: The mirror-reflection method with the sample Hugoniot known, eliminating the need to measure $U_S$.

front[55]. As is well demonstrated[29, 56, 57, 58], the conversion from laser light to X-radiation arises due to the various electronic de-excitation and recombination in a partially ionized plasma. The radiation may be due to free-free (bremsstrahlung), free-bound or bound-bound emissions[59]. The first two processes lead to continuum radiation while the last process to line radiation. In general, free-bound and bound-bound radiation dominate over free-free radiation. That the corona and conduction zone are not in a fully ionized state is especially true as the atomic number of the target increases and these regions become a strong source of X-ray. The energetic components of these X-rays (those whose energies exceed $\sim$1 keV), with corresponding long mean free paths, will pass unimpeded through the corona and ablation zone which are optically thin (i.e. transparent to this radiation) and deposit their energy in the material ahead of the shock front. Such preheat of the unshocked region of the target may affect the shock process and obscure the study of shock-induced phenomena. This difficulty can be circumvented in an impedance-mismatched target where the shock is produced by laser-driven ablation in the low-Z material before it propagates into the high-Z material of interest. The laser is then incident on a low-Z material and the resulting plasma is more likely to be fully ionized, hence reducing the generation of X-ray. Moreover, it takes a lower laser irradiance to achieve a given shock pressure in the high-Z material in an impedance-mismatched target than that is required by directly producing the shock in the high-Z material, since the impedance mismatch technique yields the benefit of pressure enhancement at the interface. A lower laser intensity can further diminish the production of harmful X-rays.

## 2.4 Equation of State

An equation of state (EOS) is a relation governing the thermodynamical properties (pressure, temperature, density, etc.) of a substance in equilibrium. Its importance is fundamental since it provides the information in predicting such diverse phenomena as phase transitions or material responses (such as compresibility or thermal conductivity) under various external conditions. Good review articles of the EOS at high pressure can be found in references [47] and [48]. Here we will briefly describe the calculational procedures used in two different EOS models.

### 2.4.1 SESAME Equation of State

The SESAME EOS library from the Los Alamos National Laboratory[50] is an extensive compilation of EOS properties (specific internal energy, pressure, average charge state) and other atomic data (such as thermal and electrical conductivity, opacity) of many different materials over a wide range of density and temperature. It has been widely used to provide EOS data for simulations in many laser-driven shock studies (see, e.g. [25, 60, 61]). We will describe some of the theoretical methods in SESAME as they apply to gold and aluminum.

The SESAME calculations of the total internal energy $E$ of gold are partitioned into three components[62],

$$E = E_c + E_i + E_e \tag{2.12}$$

where the three terms describe the cold (0K) crystalline solid (i.e. the thermodynamic states of the solid is on the zero degree isotherm), the ionic thermal vibration, and the electronic thermal contribution respectively. The cold curve calculations are based on an empirical modified Morse potential model[63], whose pressure term is of the form

$$P = a\eta^{2/3}(\eta e^{b_r\nu} - e^{b_a\nu}) \tag{2.13}$$

where $\eta = \rho/\rho_0, \nu = 1 - \eta^{-1/3}, b_a = 3 + b_r - 3B_0, B_0$ is the bulk modulus at 0K, and $a, b_r$ are two parameters to be fitted by matching on to the cold curve in the TFD (Thomas-Fermi-Dirac) model[64] at high pressures. The thermal ionic EOS model is based on an interpolation between the low temperature (<1 eV) Debye model[65] and the high temperature (>1 eV) Cowan model[65]. Lastly, the electronic contribution is also based on the TFD model.

The SESAME EOS calculations for aluminum also account for its melting transition at high pressure. In fact, seven different theoretical models are used to complete the EOS over a wide range of density and temperature. Figure 2.8 shows the density-temperature regions where each model is applied and expected to be valid. The seven regions are then joined smoothly by interpolation methods (shaded areas in Figure 2.8).

The individual models employed in the various regions are:

1. ACTEX[66] for a strongly coupled plasma (in which the potential energy of the plasma is much larger than its kinetic energy). It is based on a many-body perturbation expansion.

2. For the low density low temperature case, Young's soft sphere model for metals[67] is used. This is a semi-empirical model where free parameters are adjusted to reproduce experimental isobaric data.

3. Saha's ionization model[68] is used in the low density intermediate temperature region.

4. GRAY[69] is a semi-empirical model to treat the region between liquid to two-fold solid density at temperatunres under 1 eV. The solid EOS utilizes the Dugale-MacDonald form[70] of the Grüneisen theory. The melting transition is estimated according to the Lindemann law[71], and experimental data along the Hugoniot

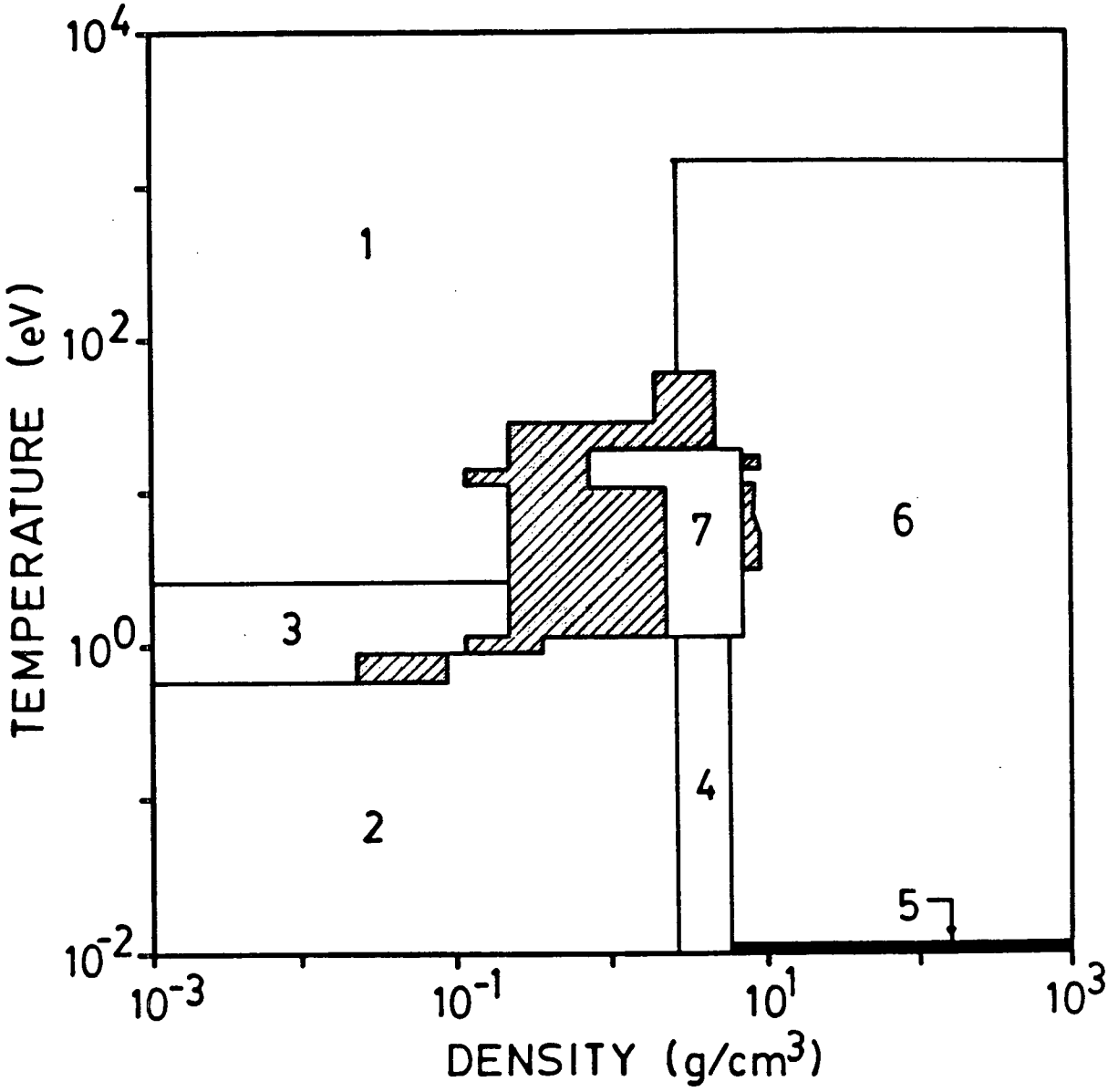


Figure 2.8: The density-temperature regimes of the seven EOS models of aluminum used in SESAME

are analytically fitted. We emphasize that it is in this region where the melting of aluminum is taken into consideration.

5. The zero-degree isotherm at high density is computed by the self-consistent augmented plane wave (APW) method[72].

6. TFNUC[73, 75] is used in the non-zero temperatures and high density case. It adds to the cold solid part (region 5) an electronic thermal contribution using the Thomas-Fermi-Kirzhnits theory [73, 74] and an ionic thermal contribution using a Grüneisen-like theory at low temperatures[75] and a one-component plasma theory at high temperatures[75].

7. The EOS for the remaining dense, partially-ionized liquid is calculated by a variational liquid metal perturbation theory of Ross[76].

### 2.4.2 New EOS Calculations for Gold

Next we discuss our new calculations of the gold EOS. This work is performed by Dr. B.K.Godwal (on leave from the Bhabha Atomic Research Center, India). The new EOS model is developed from both solid and liquid state theories. The solid phase Hugoniot is similarly computed according to the model[62] in which the total internal energy $E$ is given by eq. (2.12) and the total pressure $P$ of the material at a given volume $V$ and temperature $T$ is

$$P = P_c + \gamma E_i/V + \gamma_e E_e/V \tag{2.14}$$

with the $\gamma$'s being the Grüneisen parameters. For the evaluations of $E_c$ and $P_c$ on the cold curve (0K isotherm) as a function of $V$, a first principle energy band structure method, namely, the linearized-muffin-tin-orbital (LMTO) method[77], is used. This is a self-consistent calculation capable of evaluating the ground state properties, namely,

the energy eigenvalue and wavefunction of an ordered crystalline metal (a many body system) by solving the effective one-electron Schrödinger equation. In comparison with the more sophisticated electron band method such as the self-consistent augmented plane wave (APW) method, the LMTO method is at least a hundred times faster with little loss of accuracy. It is therefore adopted here to calculate the zero-degree isotherm.

The LMTO method is formulated within the frame work of the Hohenberg-Kohn-Sham (HKS) local density formalism[78], which provides the theoretical basis for using a variational approach to evaluate the ground state energy in the context of a density functional theory. The muffin-tin orbitals (which are specialized forms of the basis wavefunctions) are constructed using the von Barth-Hedin exchange correlation potential[79] with the ground state of gold assumed to be in a fcc (face center cubic) structure and $5d^{10}6s^{1}$ electronic configuration. The energy and pressure contributions from individual angular momentum states up to l=3 (i.e. s,p,d,f states) in the frozen-core approximation (i.e. a static lattice with immobile atoms) are included. The computations also include corrections due to the intercellular Coulomb interaction based on the model of Glötzel and McMahan[80] as well as corrections due to lattice vibrations (i.e. core is not frozen but can become a valence band state) using a procedure by Sikka and Godwal[81].

Secondly, we have used the classical Dulong and Petit law for the lattice thermal energy : $E_i = 3k_BT$ per atom, where $k_B$ is Boltzmann's constant. The corresponding pressure is $\gamma E_i/V$. Finally, the electronic thermal energy is derived using a free electron gas model (see, e.g. [47]): $E_e = \frac{1}{2}\beta T^2$ where $\beta$ is the electronic specific heat coefficient and is equal to $\frac{1}{3}\pi^2 k_B^2 N(\varepsilon_f)$ with $N(\varepsilon_f)$ being the density of states at the Fermi level. The Grüneisen parameters used above are calculated with Dugale and MacDonald's expression[70],

$$\gamma(V) = -\frac{V}{2}\frac{\partial^2(P_c V^{2/3})/\partial V^2}{\partial(P_c V^{2/3})/\partial V} - \frac{1}{3} \tag{2.15}$$

where the cold pressure $P_c(V)$ is obtained from previous results of the 0K isotherm calculations using the LMTO method.

On the other hand, the liquid phase is modelled by the corrected rigid spheres (CRIS) method[82]. This is a first order perturbation method for calculating the EOS of a fluid from the zero-degree isotherm of the corresponding solid. Like many other perturbation theories, the basic reference system in the CRIS method is that of a hard sphere fluid (a hard sphere fluid is one with "brick-wall" pair potential, i.e. the potential $U(r) = +\infty$ if $r < \sigma_0$ and 0 otherwise, where $\sigma_0 = \sigma_0(\rho, T)$ is the hard sphere diameter) whose properties are known. Yet, the CRIS method is distinguished by the fact that its first order perturbation term is an average over the 0K-isotherm rather than the pair interaction potential, which is more difficult to ascertain. Therefore, the calculation of the zero-degree isotherm using the LMTO method in the solid part can be employed conveniently in the liquid computation. Briefly speaking, the method evaluates the Helmholtz free energy $F$ of the liquid with

$$F = F_0 + N < \phi >_0 \tag{2.16}$$

where $F_0$ is the free energy of the hard sphere fluid, $N$ the total number of particles, and $< \phi >$ the potential energy of a particle in the field of its neighbors, averaged over all configurations. The calculations of the thermodynamic properties then proceed in two steps. First of all, the free energy and corresponding pressure of a hard sphere fluid are given by[82]

$$(\frac{F}{NkT})_0 = -3\ln(1 - \frac{\eta}{\eta_c}) + \sum_{k=1}^{4} A_k (\frac{\eta}{\eta_c})^k \tag{2.17}$$

and

$$(\frac{PV}{NkT})_0 = 1 + \frac{3\eta}{\eta_c - \eta} + \sum_{k=1}^{4} k A_k (\frac{\eta}{\eta_c})^k \tag{2.18}$$

where $\eta = \pi N \sigma_0^3 / 6V$ is the packing fraction and $\eta_c (=0.6452)$ that for randomly close-packed spheres. The coefficients $A_k$ are obtained from a virial expansion and are also

given in [82].

The second step is to calculate $<\phi>_0$, which is the average value of the potential in the hard sphere system. We note that within the CRIS model, each particle is located in a spherical cell of radius $R$ formed by its neighbors. If one further assumes that only the contributions from the nearest neighbors are significant, then $<\phi>_0$ is related to the 0K-isotherm energy $E_c$[82] via

$$<\phi>_0 = \frac{\pi\rho}{3}\int_{\sigma_0}^{R_m} E_c(NR^3/\sqrt{2})g_{s0}(R)R^2dR \tag{2.19}$$

where $R_m$, the cutoff radius and $g_{s0}(R)$, the nearest neighbor contribution to the radial distribution function RDF of the hard sphere fluid (RDF is a measure of the neighbors' distribution and is known) are all fitted analytically in reference [82]. The resultant internal energy and pressure are accordingly,

$$E = F - T(\frac{\partial F}{\partial T}) \tag{2.20}$$

and

$$P = -(\frac{\partial F}{\partial V}) \tag{2.21}$$

Lastly, the melting curve $P_m(T_m)$ is calculated by stipulating that melting occurs at pressures and temperatures where the two phases have equal Gibbs free energies, i.e. $G_{solid}(P_m, T_m) = G_{liquid}(P_m, T_m)$. Results of this new equation of state calculation are plotted in Figure 2.9, with the corresponding SESAME data included for comparison. The calculated solid Hugoniot agrees well with that in SESAME, but the new EOS predicts that melting of gold will begin at ~1.3 Mbar and be completed at ~2.2 Mbar. Therefore it is expected that under a shock pressure of over 2.2 Mbar, the pressure-temperature path will be along the liquid Hugoniot as illustrated in Figure 2.9. Furthermore, it can be seen that for gold at high pressure, say 7 Mbar, the solid and liquid

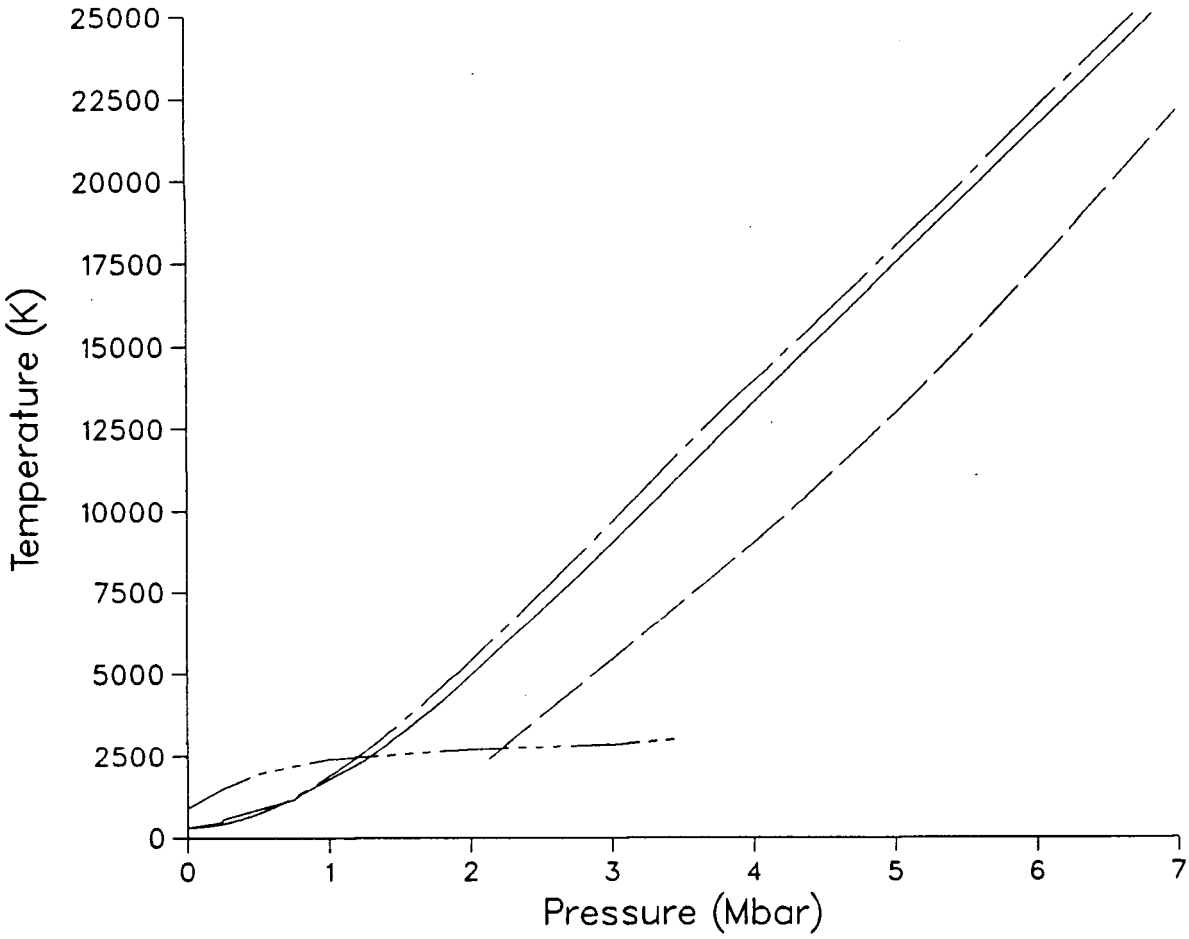


Figure 2.9: The solid (solid line) and liquid (dash) Hugoniot of gold as calculated in §2.4.2, that in SESAME (dot-dash) is also included; also shown is the melting curve (dot-dot-dot-dash)

phases are respectively at a temperature of 25600 K (2.20 eV) and 22400 K (1.93 eV), a difference that should be discernible in experiments.

## 2.5 Computer Simulations

The generally time dependent nature of a laser-driven shock wave renders the steady state assumption of §2.2 unsound. Moreover, the many physical processes involved in the interaction of a laser and a plasma, and the fact that the governing partial differential equations are coupled and nonlinear make analytical calculations extremely restrictive and often unrealistic. Computer simulations offer a viable alternative in providing theoretical support for experiments. Three different codes, SHYLAC, HYRAD, and PUC are used in our studies.

Both SHYLAC and HYRAD strive to model the hydrodynamic and thermodynamic evolutions of a material under shock condition, though they differ by their level of sophistication. Briefly, SHYLAC is a purely fluid code, while HYRAD incoporates laser-matter interactions. Both are one-dimensional, Lagrangian codes. (A Lagrangian system is one in which the fluid elements or cells are assigned coordinates which do not vary with time. In adition, each cell moves with its local fluid (particle) velocity, so that the mass in each cell is conserved. For this reason, a Lagrangian system is sometimes called a comoving system.) Essentially, the two codes integrate the three conservation equations of mass, momentum, and total energy, as well as the radiation transport equation (in HYRAD only), as they apply to either particles (ions or electrons) or radiation field in our one-dimensional planar geometry. On the other hand, the codes differ by the degree as to how

these equations are simplified and the various terms implemented. For instance, both treat the plasma as a single, inviscid and compressible fluid of interpenetrating ions and electrons, but SHYLAC is one-temperature (i.e. it assumes the same temperature for the ions and electrons) whereas HYRAD, in its more complete description, assigns different temperatures to the ions and electrons in view of the finite energy equipartition time between ions and electrons[83] due to the known dominant inverse bremsstrahlung absorption mechanism whereby the laser energy is first deposited in the electrons and later transferred to the ions (as discussed briefly in §2.1.1). In general SHYLAC is simpler and thus relatively fast, while HYRAD is more complex but more complete in its treatment of laser-plasma interaction. Both SHYLAC and HYRAD will be used in chapter 4 to simulate the shock behavior in single and multi-layered targets.

### 2.5.1 SHYLAC Code

SHYLAC is developed by Cottet and Marty[84] at Universite de Poitiers, France. In SHYLAC, the laser-induced ablation pressure is substituted by an equivalent pressure pulse. This is done according to the experimental scaling law between the laser intensity and the ablation pressure[85]

$$P_{abl} \simeq 1.4\,(\frac{\Phi_A}{10^{13}})^{0.8} \qquad [Mbar] \tag{2.22}$$

where $\Phi_A$ (in W/cm$^2$) is the absorbed laser irradiance averaged over an area equal to that of the shock breakout region, that is, the area of the shock front. Furthermore, this code incoporates an artifical viscosity, as well as an analytical (Mie-Grüneisen) equation of state. Although the assumption of an invisid fluid (i.e. no viscous stress) is usually valid, it has been shown[86] that the absence of viscosity in a hydrodynamic treatment of shock waves renders the pressure and density discontinuous at the shock front. This unphysical situation will produce strong oscillations in the density or pressure profiles[87]

(i.e. particles tending to leave their cell) and thus be numerically unstable. A fictitious term – the artificial viscosity[88] – is therefore used to introduce explicitly some amount of dissipation around the shock front in order to "smear out" the shock front, thereby limiting its maximum steepness. The Mie-Grüneisen EOS calculation, of the form

$$P = \frac{\gamma}{V}E \tag{2.23}$$

(where $\gamma$ is the Grüneisen parameter and $V$ the specific volume) has been best fitted with existing high-pressure Hugoniot data to make it more realistic. These approximations – the reduction of the complicated laser-matter interactions into a pressure pulse, the assumption that the state of the material behind the shock lies on the Hugoniot, together with the neglect of radiation transport – make SHYLAC a purely fluid code and therefore much faster and less costly to run.

### 2.5.2 HYRAD Code

HYRAD (HYdrodynamic-RADiation code) is developed at UBC. Details of the code can be found in the theses of Celliers[89] and Da Silva[90]. It is an extensively modified version of the hydrodynamic code MEDUSA[91]. Like SHYLAC, HYRAD is one-dimensional, planar, and Lagrangian in treatment. It models the dynamics of laser-target interactions and solves for the hydrodynamics, ionization state, as well as radiation transport in a self-consistent manner. The hydrodynamics is governed by the usual set of coupled differential equations representing the conservation of mass, momentum, and energy of the ions and electrons in one dimension:

$$\frac{D\rho}{Dt} = -\rho\frac{\partial u}{\partial x} \tag{2.24}$$

$$\frac{Du}{Dt} = -\frac{1}{\rho}\frac{\partial P_t}{\partial x} \tag{2.25}$$

$$\frac{D\varepsilon_i}{Dt} = -P_i\frac{\partial V}{\partial t} + Q_i \tag{2.26}$$

$$\frac{D\varepsilon_e}{Dt} = -P_e\frac{\partial V}{\partial t} + Q_e \tag{2.27}$$

where $D/Dt = \partial/\partial t + u\partial/\partial x$ is the Lagrangian time derivative, $P_t = P_i + P_e$ the total pressure, $V = 1/\rho$ the specific volume, $\varepsilon$ the specific internal energy, and $Q$ the energy source term due to various energy deposition and dissipation processes. For instance, the electron heat flux term $Q_e$ includes contributions from Spitzer heat conduction (see Eq. (2.4)), electron-ion energy exchange (not present in one temperature description), laser energy deposition, and radiative energy input. Equations (2.24) to (2.27) give the temporal evolution of density, fluid velocity, and ion and electron temperature respectively.

The ionization model is that of the collisional-radiative equilibrium (CRE) type[92], which has been shown to best describe laser-produced plasma[58, 93], especially that in the corona. In this model, the average ionization and the associated radiative power are obtained by solving a system of rate equations of the form

$$\frac{dN_i}{dt} = \sum_j W_{ji}N_j - \sum_j W_{ij}N_i \tag{2.28}$$

where $N_i$ is the population density of state i, and $W_{ji}, W_{ij}$ the rate coefficients of various mechanisms which change the system from state j to i and from state i to j respectively. Hence, the first term in Eq. (2.28) represents the population of state i from all other states, and the second term the depopulation of state i into the other states. The various mechanisms affecting state populations include radiative or collisional ionization, recombination, and excitation. The complexity of CRE lies in the fact that a large number of participating energy states and transitions, and consequently a large number of rate equations, need to be considered self-consistently. In the limit of high-temperature and low-density, radiative processes are faster than collisional ones and we will recover the familiar coronal model[59]. On the other hand, in the high-density limit where collisional

processes dominate, the plasma will be in LTE (local thermodynamic equilibrium)[94]. The hydrodynamics and ionization model are coupled as follows. The temperature and density produced by the hydrodynamic part of the calculation are needed to compute the level populations and emission of radiation (since the rate coefficients are density and temperature dependent). The emission power then enters as an energy source term in the $Q_e$ term of equation (2.27).

Finally, a multigroup approximation, which divides the radiation energy spectrum into a discrete set of frequency group, each with its own group-averaged opacity and mean free path, is used to solve the radiative transfer equation,

$$\frac{1}{c}\frac{\partial I_\nu}{\partial t} + \frac{\partial I_\nu}{\partial x} = S_\nu - \chi I_\nu \tag{2.29}$$

where $I$ is the radiation intensity, $S$ the emission source term, $\chi$ the opacity, and subscript $\nu$ the group frequency. The $S_\nu$ term represents radiative emission, and the $\chi I_\nu$ term represents absorption. Of course, the way radiation is transported is influenced by the theromodynamic state of the fluid, which is in turn affected by the radiative energy contribution. The process of radiation transport can also be "switched off" in HYRAD. This may be done to assess the effect of radiation transport. HYRAD has been extensively tested in the simulations of shock behavior in both aluminum[95] and fused silica[96].

HYRAD normally incorporates the SESAME data (LTE calculation) for its EOS. In addition, heat conduction is governed by Spitzer[42] conduction. The numerical scheme is that of the PPM (piecewise parabolic method) type[97]. This is a second order extension of the Godunov's method[98], but improves upon it by introducing the parabolae as the basic spatial interpolation functions, which allows for a steeper representation of discontinuities. The PPM has been shown to be the most accurate method[99] in the treatment of shock hydrodynamics.

Still, some processes are not included in HYRAD: suprathermal electron transport, or

numerical flux limiter. It can be seen (in chapter 3) that our experimental conditions fall within the 'classical' laser-matter coupling regime [20, 100] where $I\lambda^2 \leq 10^{14}$ $\mu$m$^2$-W/cm$^2$ ($I$ is the irradiation intensity and $\lambda$ the laser frequency) and effects such as electron flux inhibition or hot electron generation are negligible.

Although we are not specifically studying radiaion in this thesis, the effect of radiation is worth mentioning. Energy transport by radiation may play an important role particularly in experiments using a relatively long laser pulse[58, 101]. Axial radiative transport can lead to preheating in the target as discussed in §2.3.2, while lateral radiation transport leads to thermal losses, and will thus modify the hydrodynamic and thermodynamic profile of the material (see e.g. [61, 102, 103, 104]). Therefore it may affect our study of temperature due to shock heating and further discussions will be presented in chapter 4.

### 2.5.3 PUC Code

We now describe PUC (Plasma Unloading Code), which is also developed at UBC. It is an improved (in the numerical scheme) version of the PEC (Plasma Expansion Code) described in the thesis of Parfeniuk[85]. Since all of the measurements presented in this work are made at the back or free surface of a target as the shock wave emerges from this surface, a specific code (PUC) is developed in order to obtain an accurate calculation with high spatial and temporal resolution of the plasma profiles at the rear surface of the target. In particular, PUC is used to access the effect of shock unloading on the free surface emission measurements during and subsequent to shock breakout. The one-dimensional hydrodynamic code PUC treats only the hydrodynamics of a compressed target rarefying into the vacuum. The process of laser-matter interactions is not included. The simulation begins at time t = 0, which is defined to be the time of shock breakout at the free surface. At t = 0, the target-vacuum interface is assumed to be a discontinuity with the shocked state of the target specified to have the density and temperature corresponding

to the shocked condition as calculated by, for example, HYRAD. Therefore, PUC can be regarded as a "post-processor" to be used in tandem with HYRAD.

PUC is a Lagrangian, one temperature code and uses the same PPM numerical scheme as in HYRAD. It also solves the hydrodynamic equations for mass, momentum and total internal energy, and uses EOS data from either SESAME or the new equation of state of gold which incoporates the melting transition. Furthermore, the emitted radiation from the unloading material is assumed to originate locally from a blackbody source, i.e., the emitted radiation is in thermodynamic equilibrium with every region (hence local) of the compressed matter. Hence, the emission intensity $I_\lambda$ of wavelength $\lambda$ at time $t$ by a plasma located at position $x$ with temperature $T(x,t)$ is[105]

$$I_\lambda(x,t) = \frac{2hc^2}{\lambda^5}\frac{1}{\exp[hc/\lambda kT(x,t)] - 1} \tag{2.30}$$

We have to account for the fact that the path through which the radiation must traverse on its way to the detector is not optically thin (i.e. radiation does not pass unimpeded). The rarefying plasma will absorb its own radiation. The total luminosity $I_\lambda^T$ detected by a remote detector is thus

$$I_\lambda^T(t) = \int_{-\infty}^{\infty} \sigma(x)\rho(x)I_\lambda(x,t)\exp[-\int_x^{\infty}\sigma(x')\rho(x')dx']\,dx \tag{2.31}$$

where $\sigma(x)$ is the opacity and $\rho(x)$ the density along the detector line of sight. PUC will be used in the brightness temperature study to simulate the time evolution of the rear surface emission intensity (see § 4.2.2.B).

# Chapter 3

# Experimental Facility, Diagnostics, and Setup

## 3.1 Laser Facility

A schematic diagram of the laser system along with the beam diagnostics is shown in Figure 3.10. The Quantel neodymium-glass laser system includes a Nd-YAG (neodymium-doped yttrium aluminum garnet) oscillator, a Nd-YAG preamlifier, four Nd-glass amplifiers, and associated beam expanders and steering optics. The beam diameter at the exit of the final amplifier rod is 45 mm. The laser oscillator is passively Q-switched with a dye-cell and produces a single pulse at 1.064 $\mu$m in the $TEM_{00}$ mode. Three spatial filters are also distributed within the laser chain. They consist essentially of two lenses and a pinhole in vacuum to partially remove the higher spatial frequency intensity moduulations in the laser pulse. For our present experiments, the laser beam is frequency-doubled to yield 0.532 $\mu$m green light using a KD*P (deuterated potassium dihydrogen phosphate) crystal. The system is operated to deliver up to 7 joules at 0.532 $\mu$m, and the energy can be continuously varied by adjusting the amplifier pumping level. The energy of the output beam is monitored by a Gentec energy meter[106], while a fast (350 ps rise time) Hamamatsu photodiode[107] records the laser pulse shape. A typical 0.53 $\mu$m laser pulse as measured with the photodiode is shown in Figure 3.11. It is seen that the pulse shape is approximately Gaussian temporally with a full width half maximum (*FWHM*) of 2.3 ns.

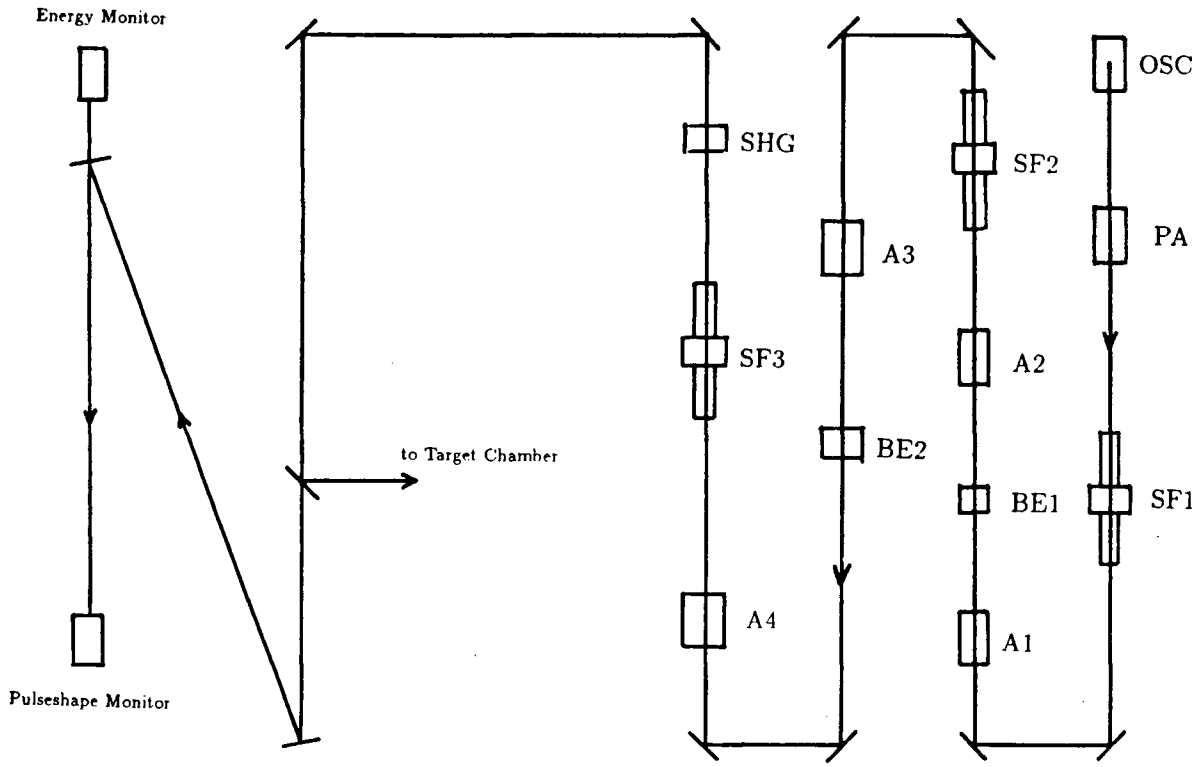


OSC = OSCILLATOR

PA = PRE-AMPLIFIER

A = AMPLIFIER

SF = SPATIAL FILTER

BE = BEAM EXPANDER

SHG = SECOND HARMONIC GENERATOR

Figure 3.10: A schematic of the laser and diagnostics system

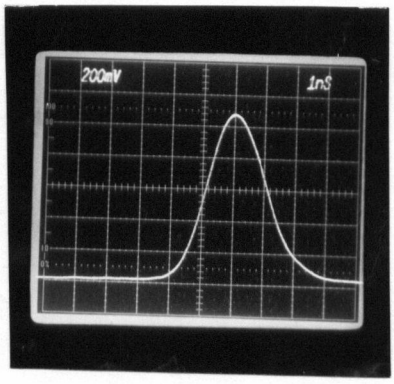


Figure 3.11: A typical laser pulse

## 3.2 Irradiation Conditions

We determine the laser intensity distribution on target by imaging the laser focal spot onto a streak camera in its focus (i.e. static, non-streak) mode. The Hamamatsu ultrafast (resolution limit of 10 ps) camera includes a temporal disperser model C979 and a temporal analyser C1440[108]. The camera is sensitive in the optical and near-UV spectrum. The overall magnification of the optical system is found by placing a grid of known spacings in the target plane. The magnification is then calculated by relating the spacings of the image of the grid as displayed on the video monitor of the streak camera to that of the object. The laser is fired at full energy and appropriately attentuated by ND (neutral density) filters placed before the final focussing lens. The laser is also focussed at the target plane to give the most uniform intensity distribution.

Figure 3.12 shows an intensity distribution of the laser focal spot, time integrated over the entire laser pulse. The spatial resolution in this measurement is $\sim$2.5 $\mu$m. It shows the laser spot to be confined in a region of approximately 80 by 100 $\mu$m. Assuming this laser spot to be approximately azimuthally symmetric, the same distribution is plotted into an equivalent azimuthally symmetric intensity profile in Figure 3.13. Figure 3.14 shows the cross-section of the laser spot of Figure 3.12 across the x- and y-coordinates spanning the central 5 $\mu$m of the spot. The laser profile is approximately trapezoidal spatially, and we calculate the intensity $\Phi_S$ by correlating with the shock breakout region as follows. From §4.1.1.A it will be shown that the shock breakout region corresponds to an area of $\sim$80 $\mu$m in diameter, and the laser intensity in this area will be calculated. On the other hand, it is seen from Figure 3.13 that 80% of the laser energy is contained within a radius $R_{80}$ of $\sim$42 $\mu$m. Therefore, the effective intensity $\Phi_S$ corresponding to the area of shock breakout is

$$\Phi_S = 0.80 \, \frac{E_{laser}}{\tau_{laser} A_{80}} \tag{3.32}$$

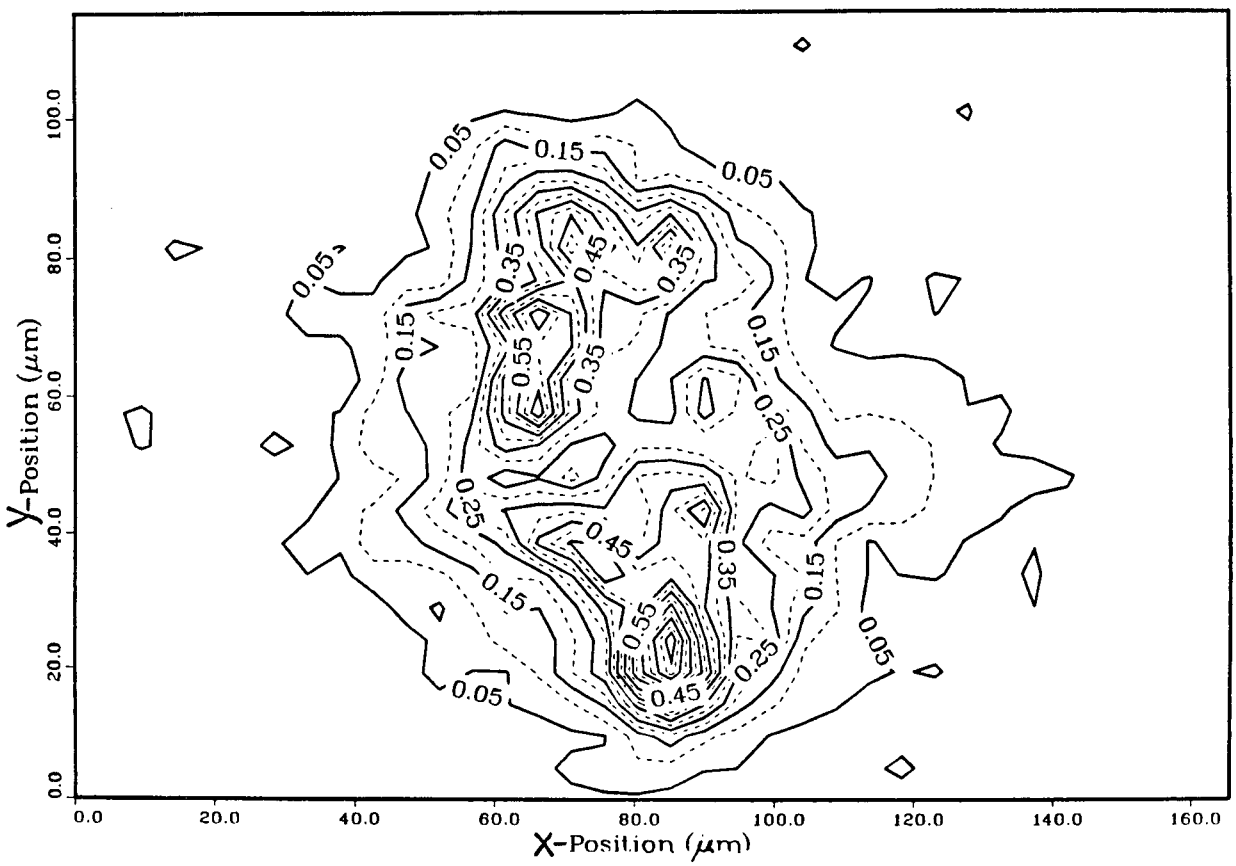


Figure 3.12: A time-integrated laser intensity distribution

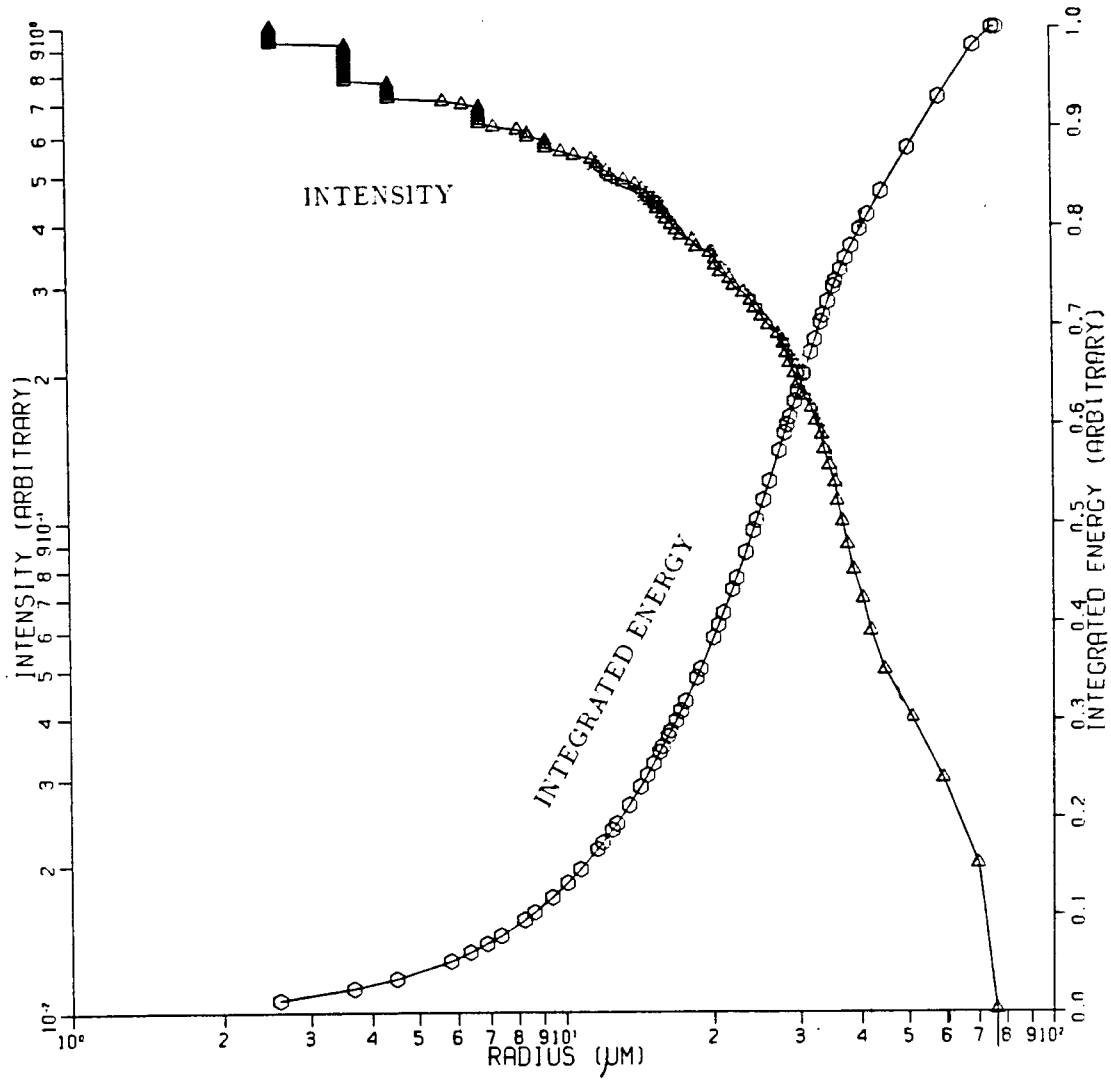


Figure 3.13: Equivalent symmetric profile of the laser spot of Figure 3.12

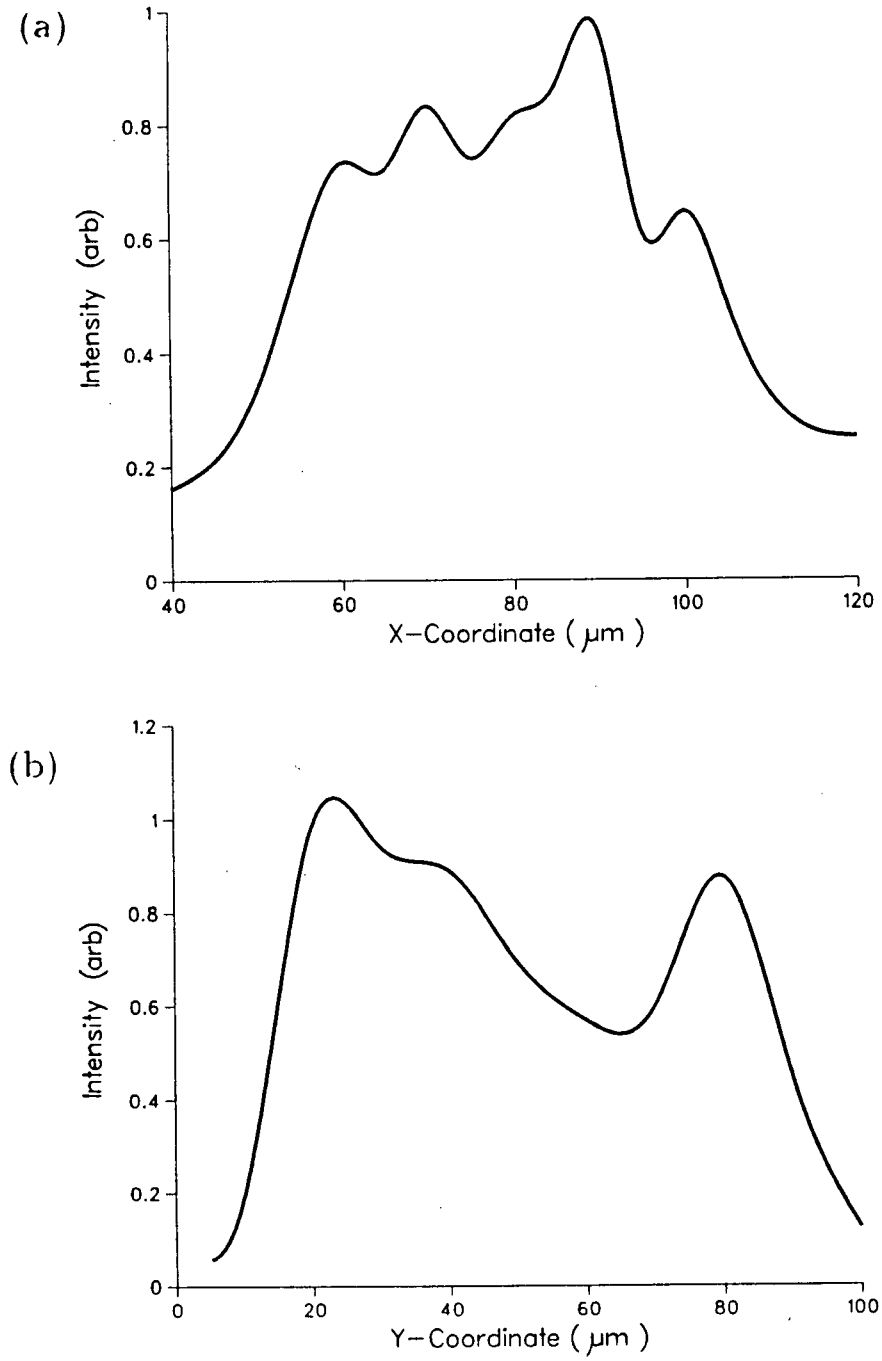


Figure 3.14: A cross section of the laser spot in Figure 3.12 across (a) the x-coordinate and (b) the y-coordinate, each spanning the central 5 $\mu$m of the spot

where $E_{laser}$ is the total laser energy, $\tau_{laser}$ the FWHM of the laser temporal profile, and $A_{80}$ ( $= \pi R_{80}^2$) the area where 80% of the laser energy is contained. The laser irradiance calculated using this procedure has been successfully used as an input parameter in previous hydrocode simulations, where the ablation pressure and shock trajectory thereby predicted agree well with experimental results (see [49, 55, 109]). In our experiments, the intensity distribution is approximately Gaussian in time, and using equation (3.32) (with $E_{laser} = 4.2 \pm 0.4J, \tau_{laser} = 2.3 \pm 0.2ns$), the incident intensity is therefore 2.6±0.7 x $10^{13}$ W/cm$^2$. The absorption of 0.53 $\mu$m laser on aluminum targets has been measured in previous studies[110, 111]. Based on those measurements, the absorbed irradiance is $\Phi_A = f_a \cdot \Phi_S = 2.3 \pm 0.6$ x $10^{13}$ W/cm$^2$, where $f_a$ is the absorption fraction[110].

## 3.3 Experimental Arrangements

Figure 3.15 shows the experimental arrangement inside the target chamber and the imaging optics for observation of the taget rear surface. This setup is used to record the luminous radiation emitted from the rear surface of the target as the shock wave emerges from this free surface. The target chamber is maintained at a pressure of about 60 mtorrs. In the experiment, planar targets of aluminum foils or doubled-layered aluminum-gold targets are irradiated with 0.53 $\mu$m, 2.3 ns FWHM laser pulses. This main laser pulse is directed into the chamber with a series of three dichoric mirrors, and is focussed onto the front aluminum surface of the target with f/6.7 optics at normal incidence.

The rear surface of the target is imaged onto the entrance slit of the streak camera with f/1.4 achromatic optics placed at target normal. The rear surface luminous emission

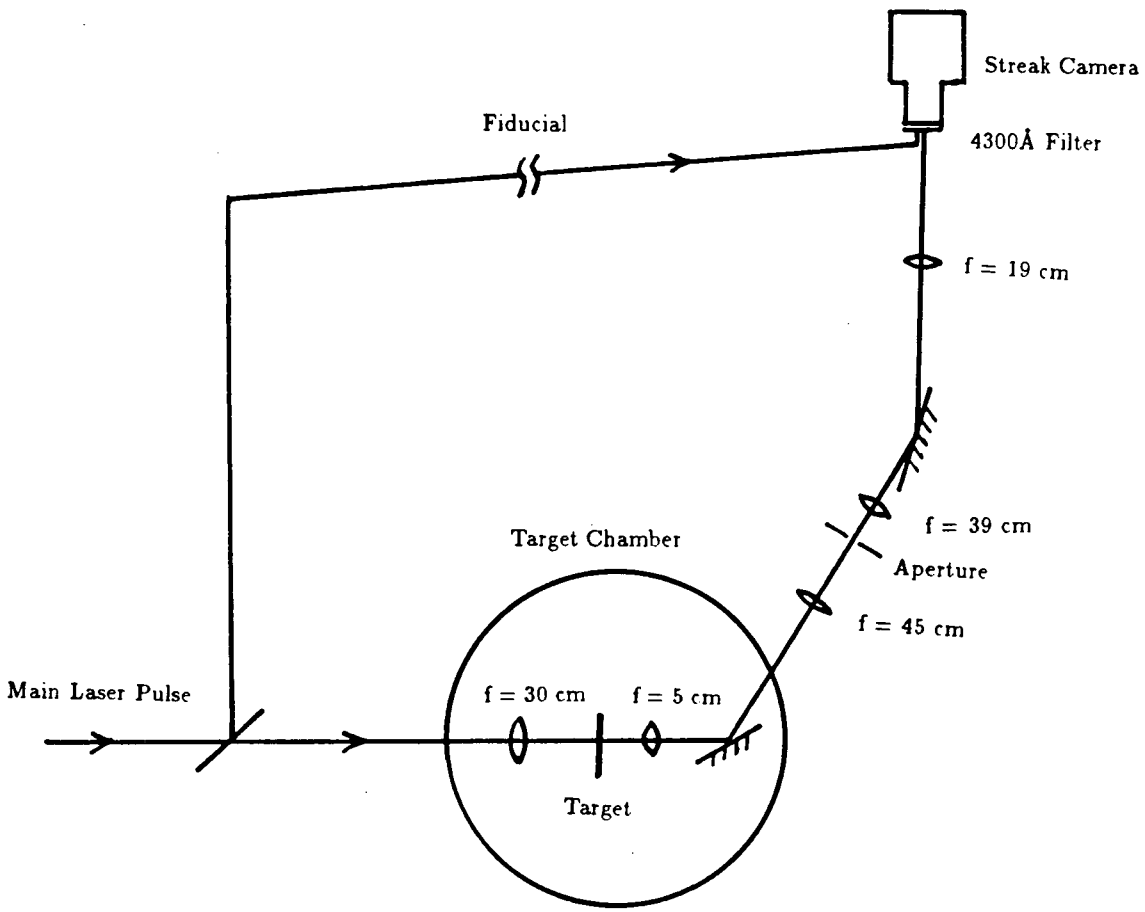


Figure 3.15: The experimental setup in the luminscence study

is observed through a 100Å-bandpass interference filter centered at $\lambda_0$=4300Å (rejection ratio outside the band between $0.82\lambda_0$ and $1.1\lambda_0$ is 0.01%) placed at the streak camera entrance. This eliminates laser stray light from entering the camera. The temporal history of the spatial distribution of the luminous emission is recorded by the streak camera and then displayed on the video monitor.

As there is a time jitter of up to 50 ps between the time the streak camera is triggered by a laser pulse derived from the main beam to the time when it actually begins its "streaking" operation, the timing of the free surface emission with respect to the laser pulse can only be determined using a reference laser pulse or fiducial which is recorded simultaneously by the streak camera. Such a fiducial is derived from the main laser beam as indicated in Figure 3.15. The optical pathlength of the fiducial from the exit of the laser chain (i.e. after the KD*P crystal) to the entrance of the streak camera is made nearly equal to that of the main laser beam going through the target and the imaging optics at the target rear side. Hence, the fiducial signal becomes an "effective" main laser pulse and the timing of the luminous emission from the free surface of the target can be correlated unambiguously with the incident laser pulse. Our experimental setup yields a fiducial reference which leads the main beam by 375±75 ps. This is taken into account in the analysis of shock velocity data.

In addition, the fiducial also provides a measure of the laser pulse shape on the streak camera monitor. Although the streak camera has a lower dynamic range ($\leq$ 100) than that of the photodiode (>1000), the pulse shape recorded by the streak camera nevertheless readily identifies the time of peak laser intensity, which is needed as the time reference (taken as time zero here) for any shock-related phenomenon under study.

Depending on the type of measurements, the duration of the streak may be set at 5.42 or 1.26 ns. The slower streak mode (5.42 ns) is used for shock velocity measurements where the entire fiducial pulse can be recorded. In the case of temperature measurements,

in which the laser fiducial is not necessary, the faster streak speed (1.26 ns) is chosen instead to improve the temporal resolution of the measurement.

In the experiment, an appropriate number of neutral density filters are inserted into the optical path of the fiducial pulse. This helps to reduce the light intensity to an acceptable level so as not to saturate the streak camera tube, which can lead to premature tube deterioration.

# Chapter 4

## Luminescence Measurements in Single and Doubled-Layered Targets

### 4.1 Shock Velocity Study

As a shock wave propagates through the target the region behind the shock front is heated. When the shock front reaches the back or free surface of the target, the luminous emission from the heated material can to be detected by a streak camera. Since the target is initially cold (i.e. at room temperature) and opaque, no radiation will be observed from the sample until the time of shock emergence. Actually, the radiation will become visible when the shock front is within a distance of several optical mean free paths $l$ from the free surface. For example, for radiation at 4300Å(2.88 eV), the mass absorption coefficient (opacity) $\kappa$ of aluminum under normal conditions is $\sim 5 \times 10^4$ cm$^2$/g and the corresponding mean free path is $l = (\rho\kappa)^{-1} \simeq 0.1$ $\mu$m. Therefore, the time of shock breakout at the free surface is signified by a sudden occurence of luminous emission. By measuring the shock breakout times in targets of different thicknesses, one can map out the shock trajeatory from which the shock speed $U_S$ can be determinedd. Such measurments can therefore be used as a diagnostics to study the laser-driven shock wave.

As discussed in chapter 2, equation of state studies using the impedance-mismatch technique requires the experimental determination of the shock velocity in either the standard material, or that in the sample of interest. However, in shock-induced luminous emission measurements with impedance-mismatched targets, one is restricted to measure the shock arrival times at the free surface of the sample only. This by itself is not sufficient

to yield the shock speed in either the standard or the sample, since it represents the total shock transit time through the two materials of the target. On the other hand, one can first characterize the shock produced in the standard.

In our experiments[112], aluminum (Z = 13, $\rho_0$ = 2.7 g/cm$^3$) is chosen as the low-impedance standard in the aluminum-on-gold targets (gold as the high-impedance sample, with Z = 79, $\rho_0$ = 19.3 g/cm$^3$) in the impedance-mismatch study. Aluminum is selected as our standard since its EOS data are well tabulated, both in terms of theoretical calculations[50] and experimental measurements[49].

### 4.1.1 Single Layer Aluminum Foil

#### 4.1.1.A Experimental Observations

Aluminum foils[113] of various thicknesses ranging from 25 to 53 $\mu$m are used. The luminous emission associated with shock breakout at the free surfaces of the targets are recorded by the streak camera. The overall magnification of the diagnostic system (including the imaging optics and the streak camera optics) is measured by placing a fine wire mesh of known spacing at the target plane, focussing it onto the streak camera, and noting the spacing of the magnified image displayed on the camera monitor. With a magnification of ~125, the spatial resolution achieved is approximately 8 $\mu$m. The entrance slit of the camera is set at 200 $\mu$m. This produces a streak image with good signal-to-noise ratio of ~50, however it degrades the time resolution to ~50 ps. This far exceeds the ideal streak camera resolution of 10 ps.

As discussed in chapter 3, the luminous emission is observed through a 100 Å band-pass filter centered at 4300 Å. Figure 4.16 shows spatially resolved streak records of the emission from the shock breakout regions in 38.4 and 53 $\mu$m aluminum targets. A fiducial signal is also recorded to allow determination of the shock breakout time with respect to

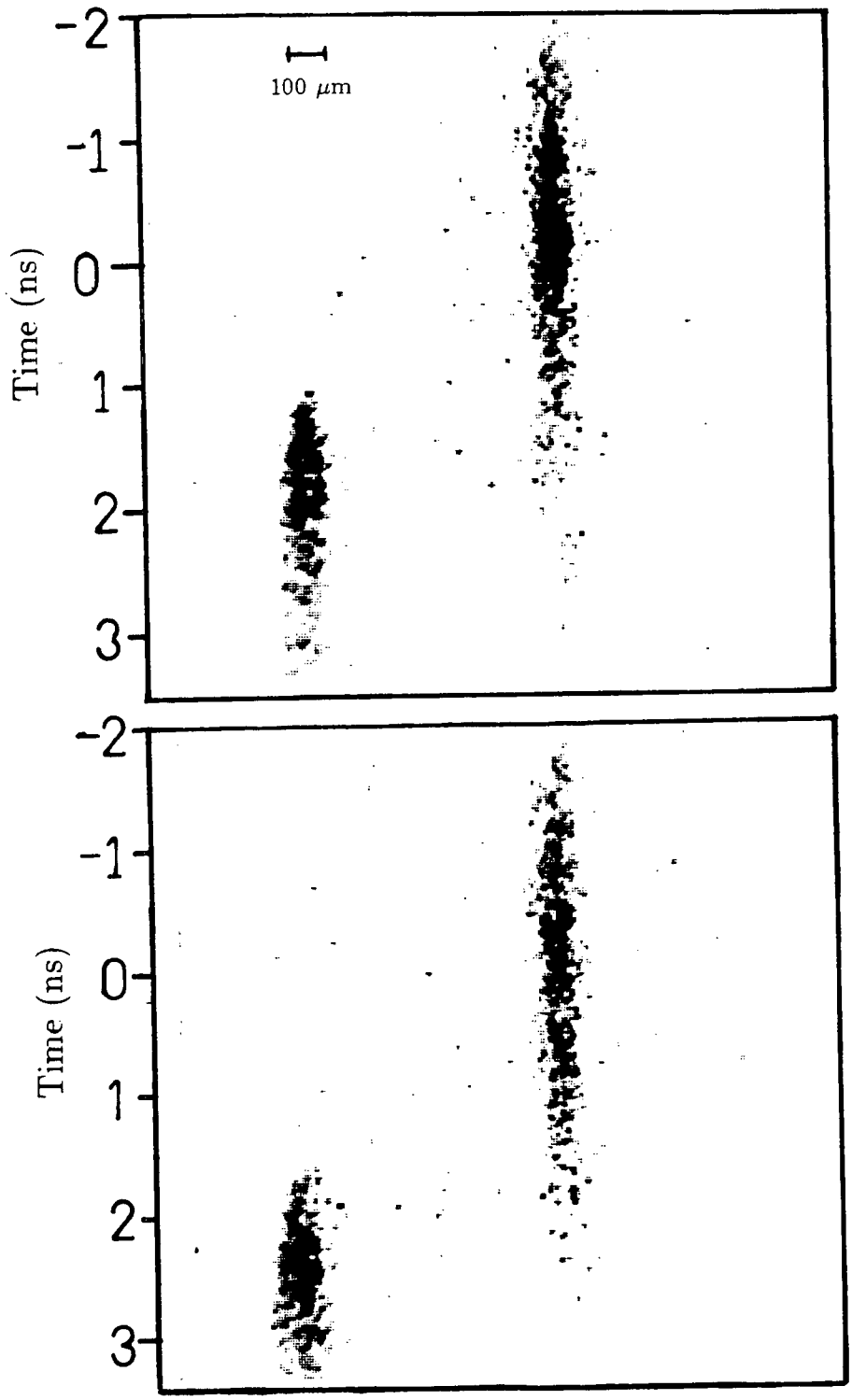


Figure 4.16: Streak records of shock breakout emission (left streak) and fiducial signal (right streak) in (a) 38.4 $\mu$m and (b) 53 $\mu$m aluminum target.

the main laser pulse. Time zero corresponds to the peak of the laser pulse. The shock is observed to emerge at the free surface in a region of ~80 ± 10 $\mu$m diameter. No hot spots (regions of very high intensities) are observed. In the analysis of the emission intensity, we consider the emission spatially integrated over the central 45 $\mu$m span in the shock breakout region which is wide enough to yield a sufficiently good signal to noise ratio, but narrow enough to ensure approximate shock planarity. Figure 4.17 shows the temporal history of the shock-induced luminous emission intensity and the fudicial for a 38.4 $\mu$m aluminum target. The rise times (between the 10% to 90% intensity of the initial peak) of the emission for all the targets are typically 230±70 ps. The shock breakout times in 25, 29.3, 38.4, and 53 $\mu$m aluminum are found to be respectively 0.0±0.1, 0.30±0.06, 1.03±0.05, and 1.89±0.11 ns after the time of the laser peak. No target preheat is observed as indicated by the fast rise times in the emission intensity.

#### 4.1.1.B Computer Simulations

To model the dynamics of the shock, the purely hydrodynamic code SHYLAC is used first. Although this code does not incoporate the laser-matter interaction processes, it is nevertheless fast and inexpensive. Our particular simulations assume a Gaussian pressure pulse of 2.5 ns FWHM with a peak pressure of 3.5 Mbar. This is to approximate the ablation pressure generated by our 0.53$\mu$m, 2.3 ns FWHM laser pulse at an absorbed irradiance of $\Phi_A$ = 2.3 x $10^{13}$ W/cm$^2$ according to the previously obtained experimental scaling law in equation (2.22). This approximation of the ablation pressure appears to be reasonable as seen from results of the more elaborate HYRAD simulations which include the laser-induced ablation process. A comparison of the calculated ablation pressure from HYRAD and the Gaussian pressure pulse assumed in SHYLAC is shown in Figure 4.18. The rising portions of the two pulses (which drive the shock) agree reasonably well, but the ablation pressure pulse has a longer FWHM (2.9 ns) than the assumed pressure pulse

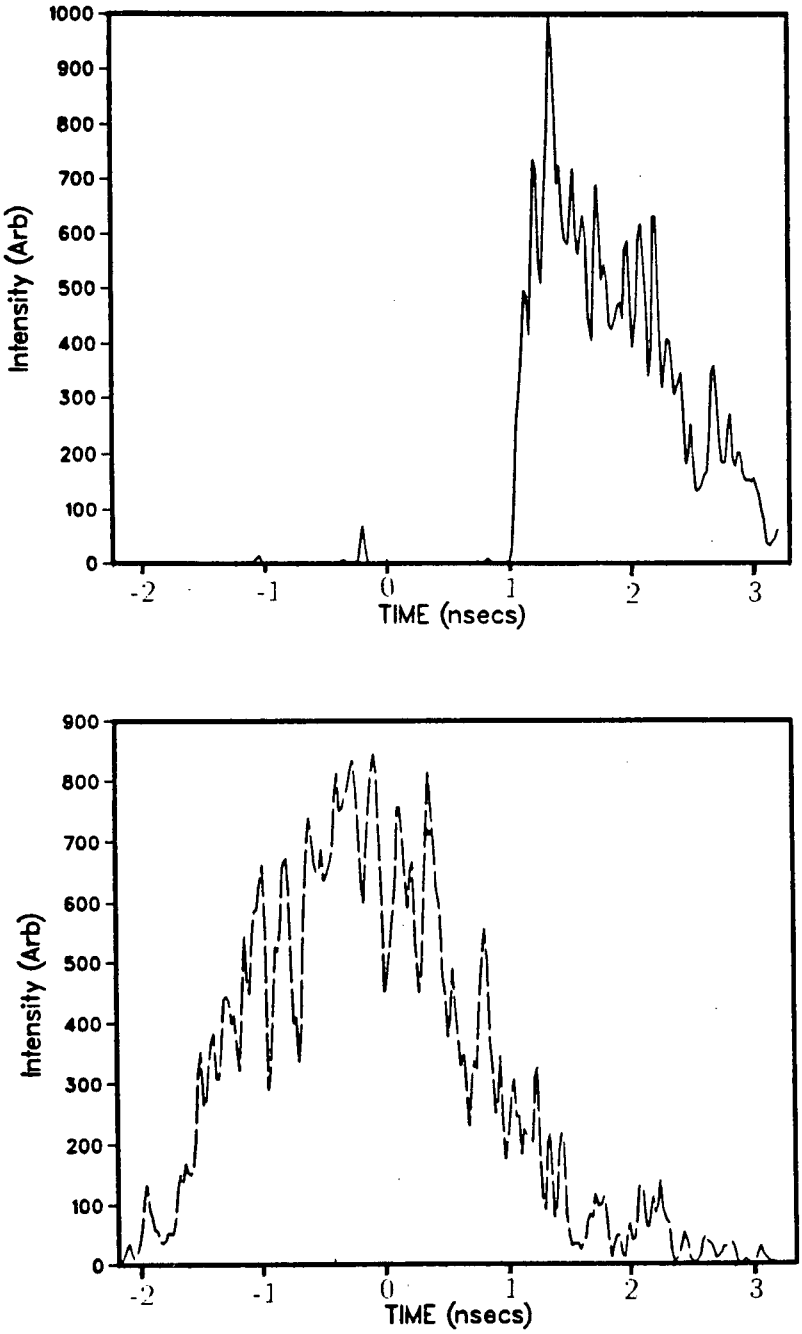


Figure 4.17: Temporal history of the (a) shock breakout and (b) fiducial streak in a 38.4 $\mu$m Al target

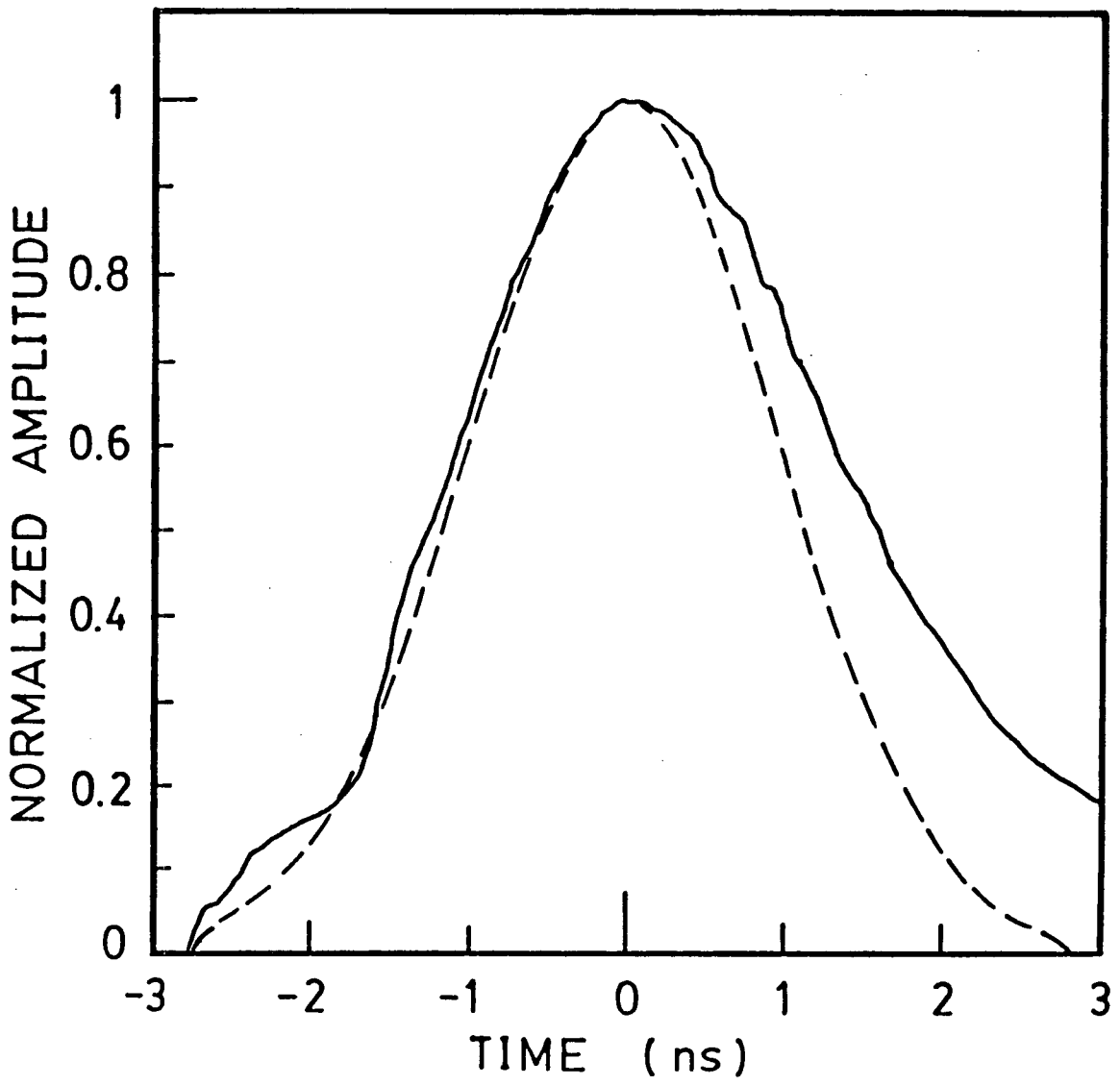


Figure 4.18: The calculated ablation pressure pulse from HYRAD (solid) and the Gaussian pressure pulse assumed in SHYLAC (dash)

used in SHYLAC (2.5 ns).

Figure 4.19 shows the measured shock transit time as a function of target thickness for the given absorbed irradiance as well as the calculated shock trajectory using SHYLAC. To test the accuracy of the SHYLAC simulation, we have also calculated the shock trajectory using HYRAD. Two different cases are considered in the HYRAD simulations, one where the process of radiation transport is taken into account, and the other where radiation transport is neglected. (In this and subsequent simulations where the radiation transport process is included, the radiation is divided into 10 energy groups from 0.3 to 10 keV, as described in the discussion of multigroup approximation in §2.5.2) From the simulations, we note that the shock is accelerating (i.e. non-steady) at early times. The shock then reaches a quasi-steady state when it has propagated to a depth of approximately 20 $\mu$m in the target. The quasi-steady shock speed is found to be (1.5 $\pm$ 0.1) x $10^6$ cm/s.

The agreement among the three calculated shock paths and experimental data are equally good, and there is no indication that one simulation is more preferable to another. Thus, the shock transit time measurement is not sensitive enough to discriminate one model (SHYLAC) against another (HYRAD) or to identify the significance of radiation transport in the shock process. It appears that SHYLAC is adequate in the prediction of shock path and velocity. However, we shall use HYRAD including the radiation transport process to simulate our subsequent experiments, as it has the most complete treatment of the laser-matter interactions.

It should be noted that the shock pressure can also be estimated by comparing the measured shock velocity with Hugoniot data. From the SESAME EOS library, the measured shock speed of (1.5 $\pm$ 0.1) x $10^6$ cm/s corresponds to a pressure of 3.1 $\pm$ 0.5 Mbar. This is in agreement with the pressure of 3.5 Mbar used in SHYLAC.

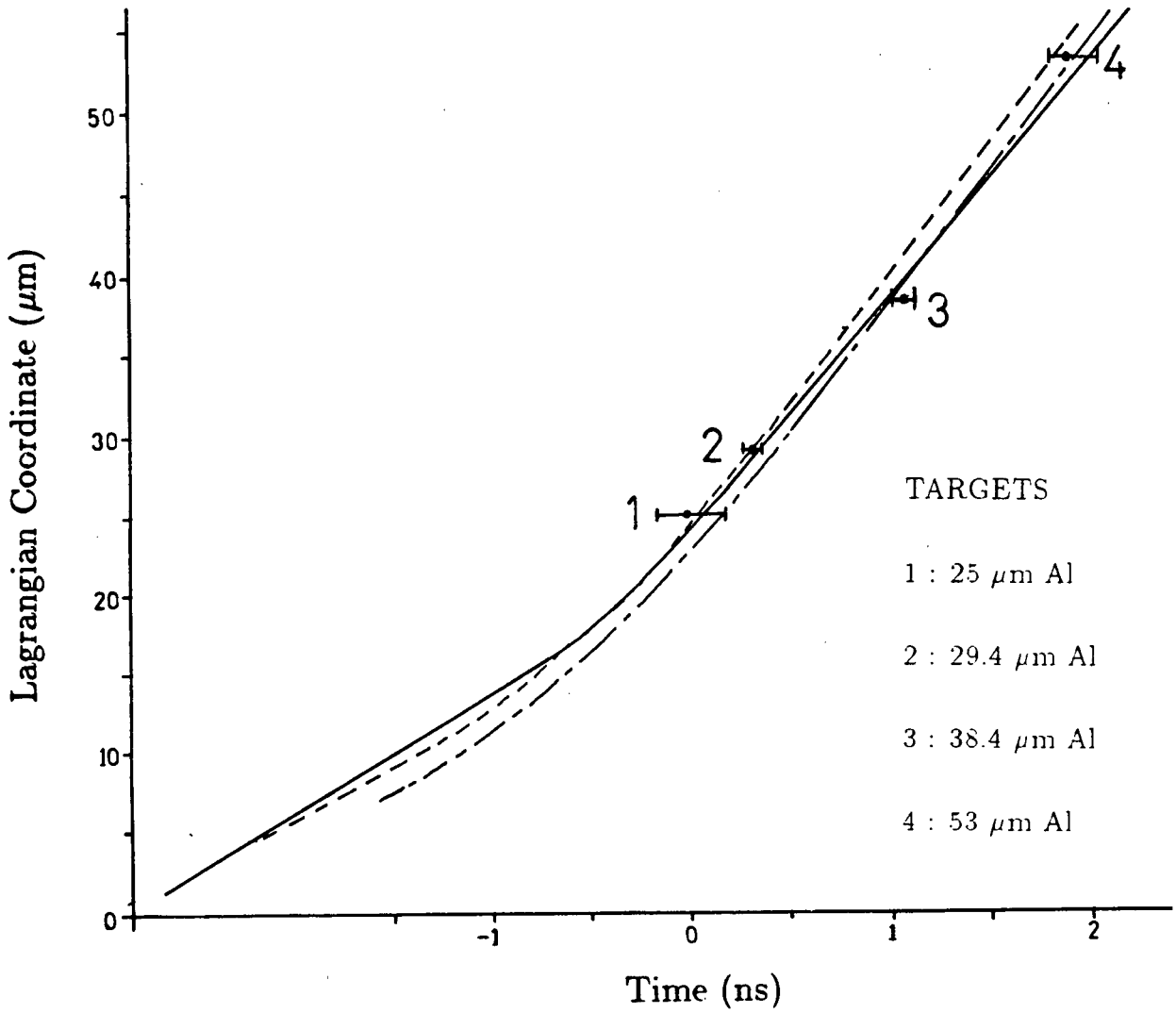


Figure 4.19: Calculated shock paths by SHYLAC (dot-dash), by HYRAD without radiation transport (dash), and with radiation transport (solid); also plotted are the experimental results in various aluminum targets

### 4.1.2 Aluminum-Gold Targets

#### 4.1.2.A Experimental Observations

The layered targets used in this experiment are manufactured commercially by vapor deposition, i.e. evaporation of gold onto aluminum substrate. These targets include a combination of either 19 or 26.5 $\mu$m of aluminum layers with either 8.4 or 13 $\mu$m of gold layers. In order to obtain pressure enhancement, the targets are irradiated on the aluminum side. For these targets, the shock arrival times at the back surfaces (the free surfaces of the gold layer) are measured by the same technique as described in § 4.1.1.A. Figure 4.20 shows a sample streak record of the shock-induced luminous emission and the laser fiducial for a 19 $\mu$m aluminum on 8.4 $\mu$m gold target. We see similar qualitative behaviors in the backside luminous emission as those in pure aluminum targets; again, no target preheat or hot spots are observed. The shock breakout times are 0.74 ns in 19 $\mu$m aluminum on 8.4 $\mu$m gold, 1.08 ns in 19 $\mu$m aluminum on 13 $\mu$m gold, 1.10 ns in 26.5 $\mu$m aluminum on 8.4 $\mu$m gold, and 1.89 ns in 26.5 $\mu$m aluminum on 13 $\mu$m gold. The uncertainities in the measured breakout times are $\pm$0.1 ns.

#### 4.1.2.B Computer Simulations

The simulations are performed in two parts. The first part is to examine the various issues and criteria governing the design of an impedance-mismatched target. Since a large number of aluminum-gold targets of different thicknesses need to be considered, we have selected the SHYLAC code because it is speedy to run and contains the relevant physics of shock propagation. HYRAD is used in the second part of the simulations to provide detailed calculations for the interpretation of experimental data for specific and a limited number of target configurations.

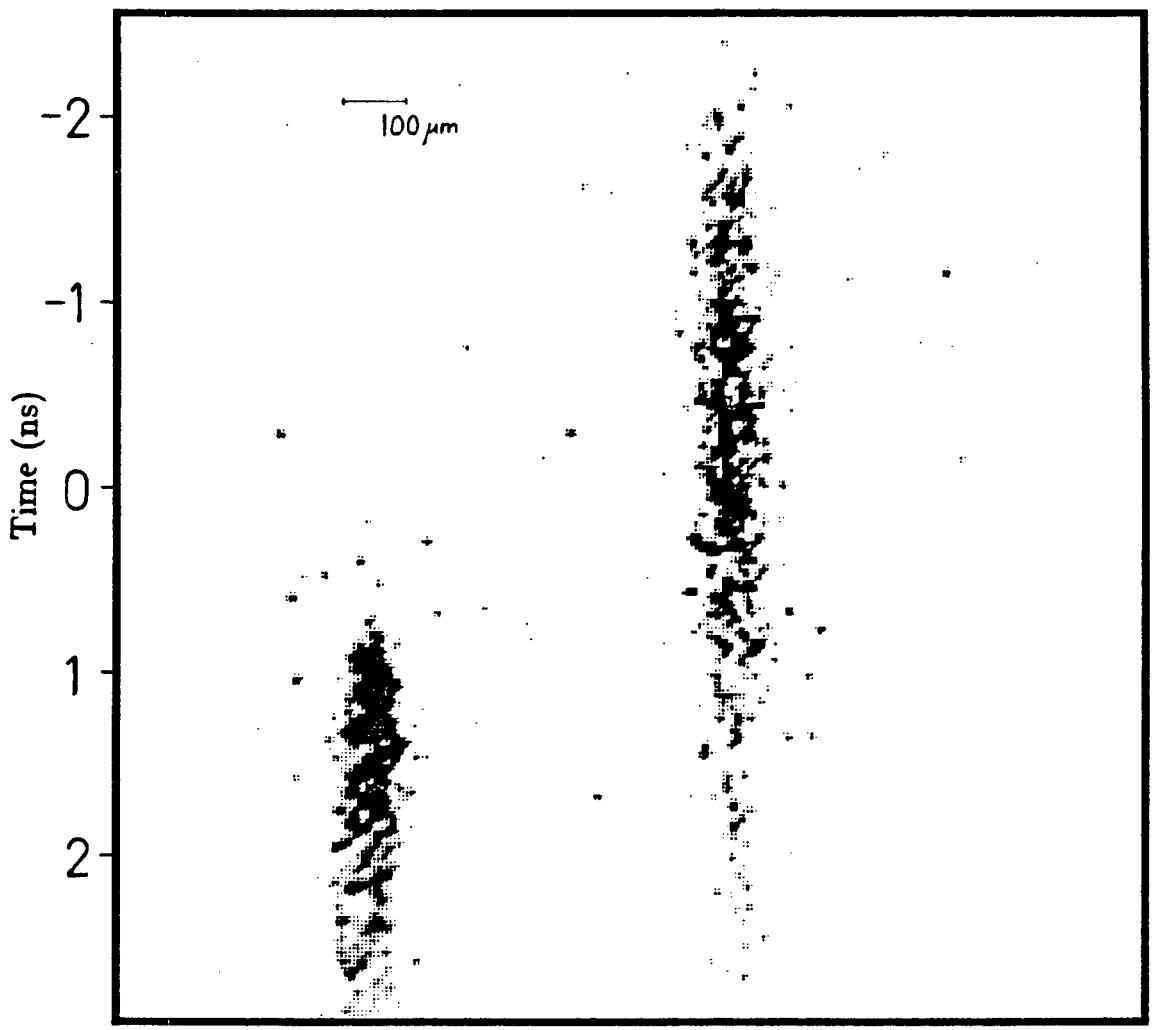


Figure 4.20: Streak record of free surface luminous emission (left streak) and fiducial signal (right streak) of a 19 $\mu$m aluminum on 8.4 $\mu$m gold target

**4.1.2.B.i SHYLAC simulations for Target Optimization** In SHYLAC, the Mie-Grüneisen equation of state models for aluminum and gold are used and the shock pressure is computed accordingly. As before, we have assumed that a Gaussian pressure pulse of 2.5 ns (FWHM) and peak pressure of 3.5 Mbar is applied on the front surface of the aluminum layer. In the simulations, the thicknesses of the gold layer are taken to be thick enough so that the shocks do not reach the free surfaces during the simulation periods. Equivalently, the gold layer thickness in these smulations can be taken to be infinity so that no free surface exists in the time duration of the simulations and no free surface rarefactions are produced. The resulting pressure profiles at different times in aluminum-gold targets for aluminum layers with thicknesses ranging from 5 $\mu$m to 50 $\mu$m are plotted in Figures 4.21 to 24. One can clearly see the leading edge of the strong shock wave, represented by the sharp increase in pressure, and the "dynamic" nature of the shock as it propagates into the target. The pressure at the shock front represents the shock breakout pressure if a free surface were at that position. For example, in the case of a 19 $\mu$m Al on 13 $\mu$m Au target (Fig. 4.23), the free surface pressure at shock breakout (i.e. when the shock front reaches a target distance of 32 $\mu$m) would be approximately 7.3 Mbar.

A number of conclusions can immediately be drawn from the figures. First of all, pressure enhancement can indeed be achieved at the interface with appropriate choices of the front aluminum thicknesses. Secondly, by no means is the shock truly steady. This is due to the fact that the driving pressure pulse is time-dependent. Shock buildup takes place during the time when the pressure pulse is increasing in amplitude. The formation of a single strong shock front has already been discussed in §2.1.3. Furthermore, as the pressure of the driving pulse drops and eventually ceases, a rarefaction or unloading wave develops at the front surface of the target. This propagates into the shocked medium with the velocity of sound in the shocked region, which is faster than the shock speed.

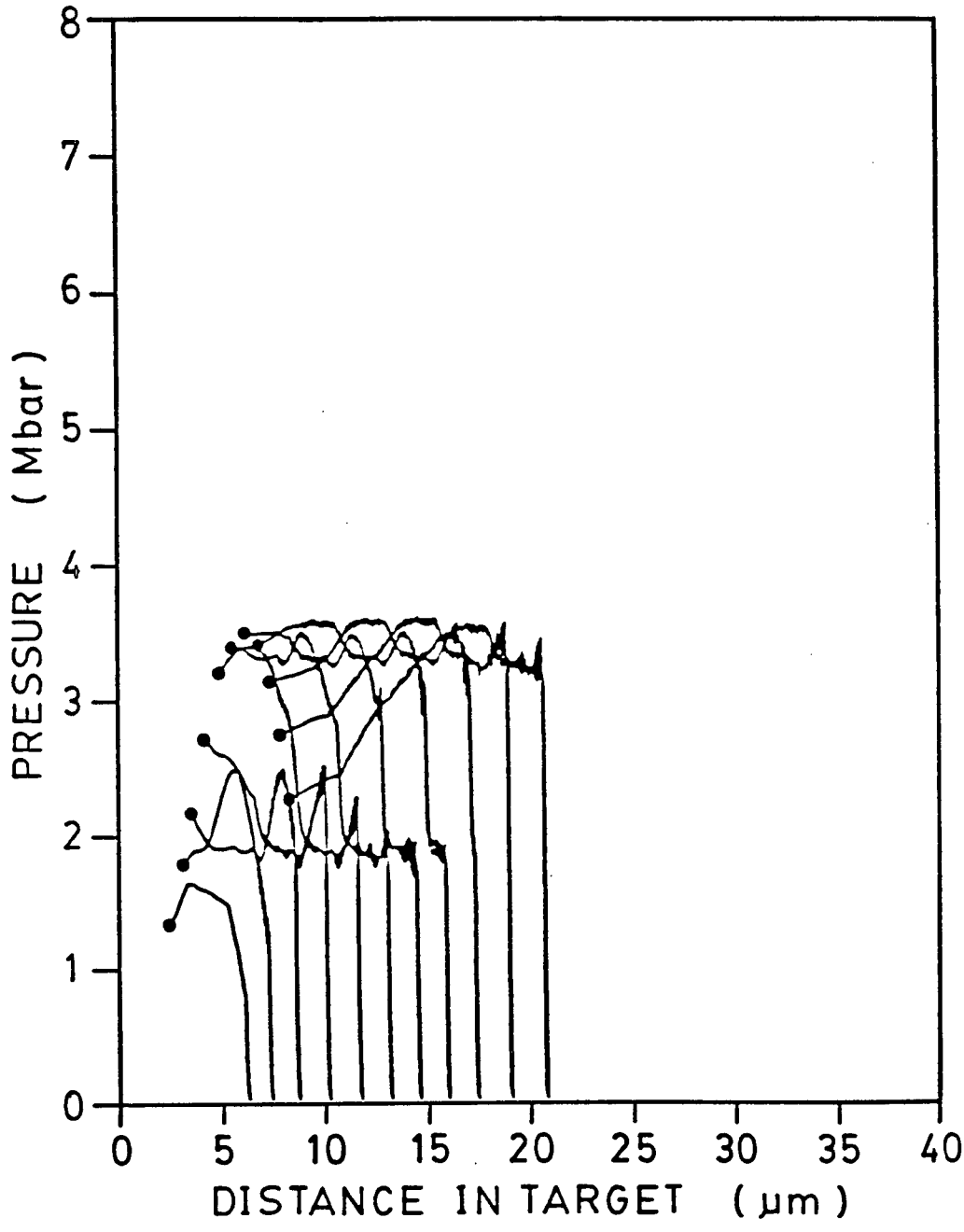


Figure 4.21: Shock pressure profiles in Al-Au targets with the front aluminum thickness equal to 5 $\mu$m. The initial profile corresponds to a time of 1.5 ns before the pressure pulse peak, and subsequent ones are 0.25 ns apart.

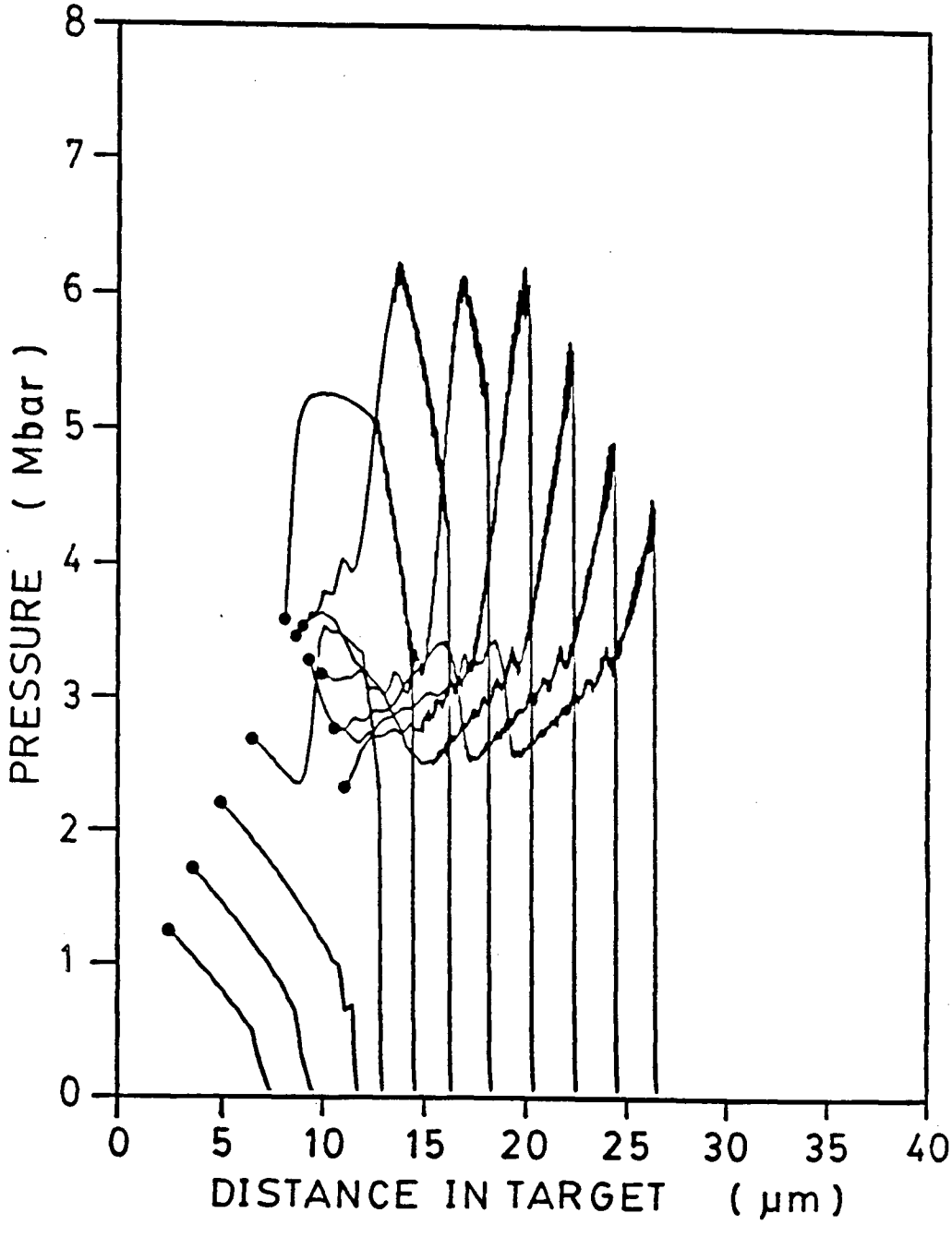


Figure 4.22: Same as Figure 4.21 but aluminum thickness is 11.5 $\mu$m

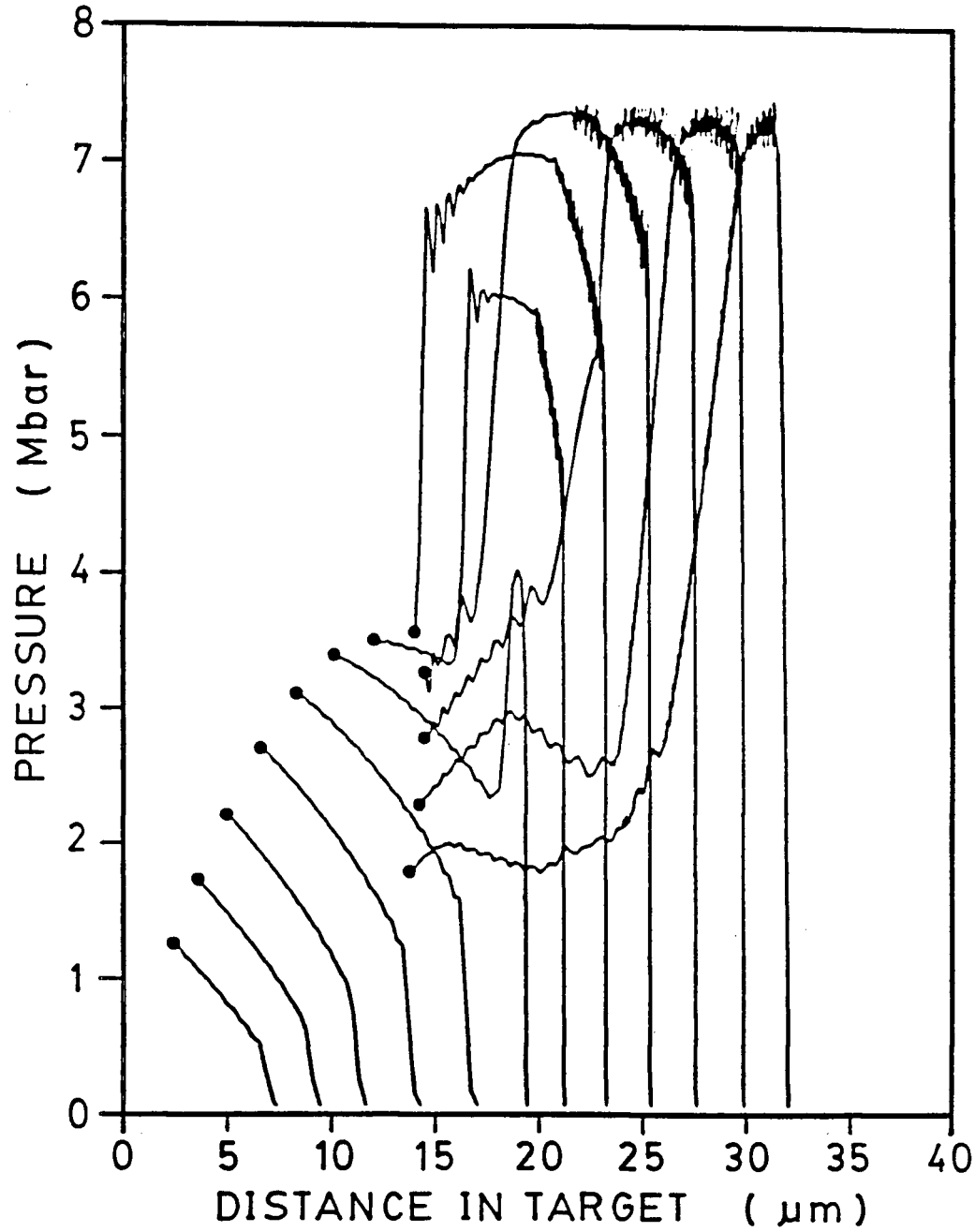


Figure 4.23: Same as Figure 4.21 but aluminum thickness is 19 $\mu$m

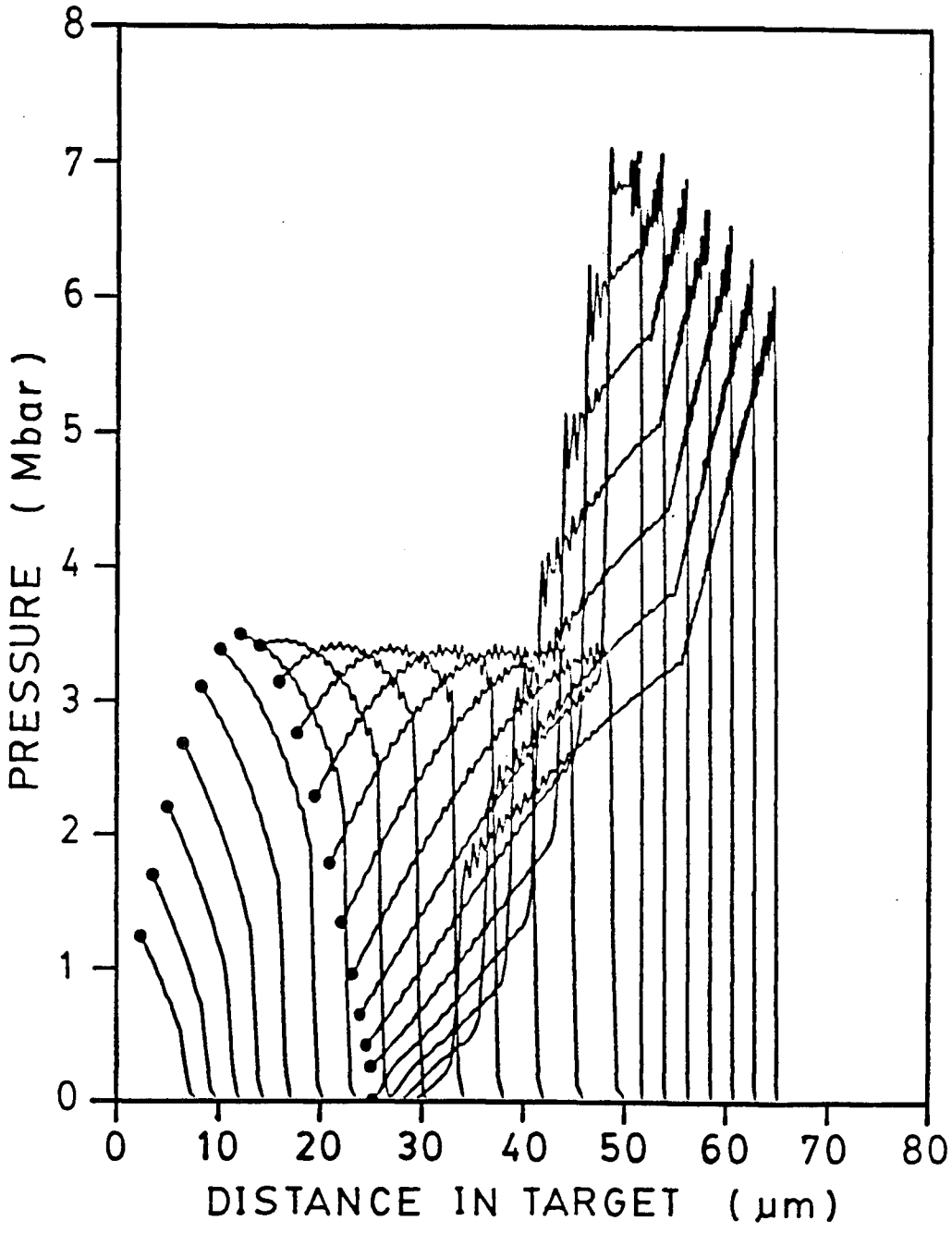


Figure 4.24: Same as Figure 4.21 but aluminum thickness is 50 $\mu$m

When it catches up with the shock front, the pressure at the sock front will be reduced. This is called shock attentuation or damping. Thus if the aluminum layer is too thick (Figure 4.24), the shock will be attentuated before it reaches the interface; hence the transmitted pressure into the gold layer will not be as high as it can be. On the other hand, if the aluminum layer is too thin (Figure 4.21), an incompletely formed shock front will impinge too early on the interface to benefit significantly from the pressure enhancement by shock reflection. Furthermore, if the shock waves reach the interface too soon, the backward-moving reflected wave, propagating back into the aluminum layer, will therefore effect premature shock attentuation in the aluminum layer (Figure 4.22), and again one will not have derived the maximum benefit from impedance-mismatching. As for the gold layer, if it is too thin, then the transmitted shock may not have been completely formed (cf. the process of shock steepening in gold in figures 4.22 and 22) whereas if it is too thick, shock attentuation will occur before the shock reaches the free surface.

Figure 4.25 illustrates the effects of the aluminum and gold thicknesses on the free surface pressure induced in gold. These effects are complicated, and the final free surface pressures certainly cannot be calculated on the basis of equation (2.11) alone. (N.B. In the case of an ideal steady shock, the transmitted shock pressure as given in eq. (2.11) equals the free surface pressure in gold.) Also plotted in the figure is the maximum pressure $P_{SW}$ which can be induced in the gold layer for the given initial pressure pulse if the incident shock were ideal, i.e. a steady shock of 3.5 Mbar.

As stated in previous discussions, the shock-induced pressure in the gold layer is influenced by the thicknesses of both the front aluminum layer and the rear gold layer. Hence pressure optimization, or alternatively thickness optimization, represents the optimization between incomplete shock buildup in thin targets and shock attentuation in thick ones. Previous studies using computer simulations include the work of Salzmann et al.[54]

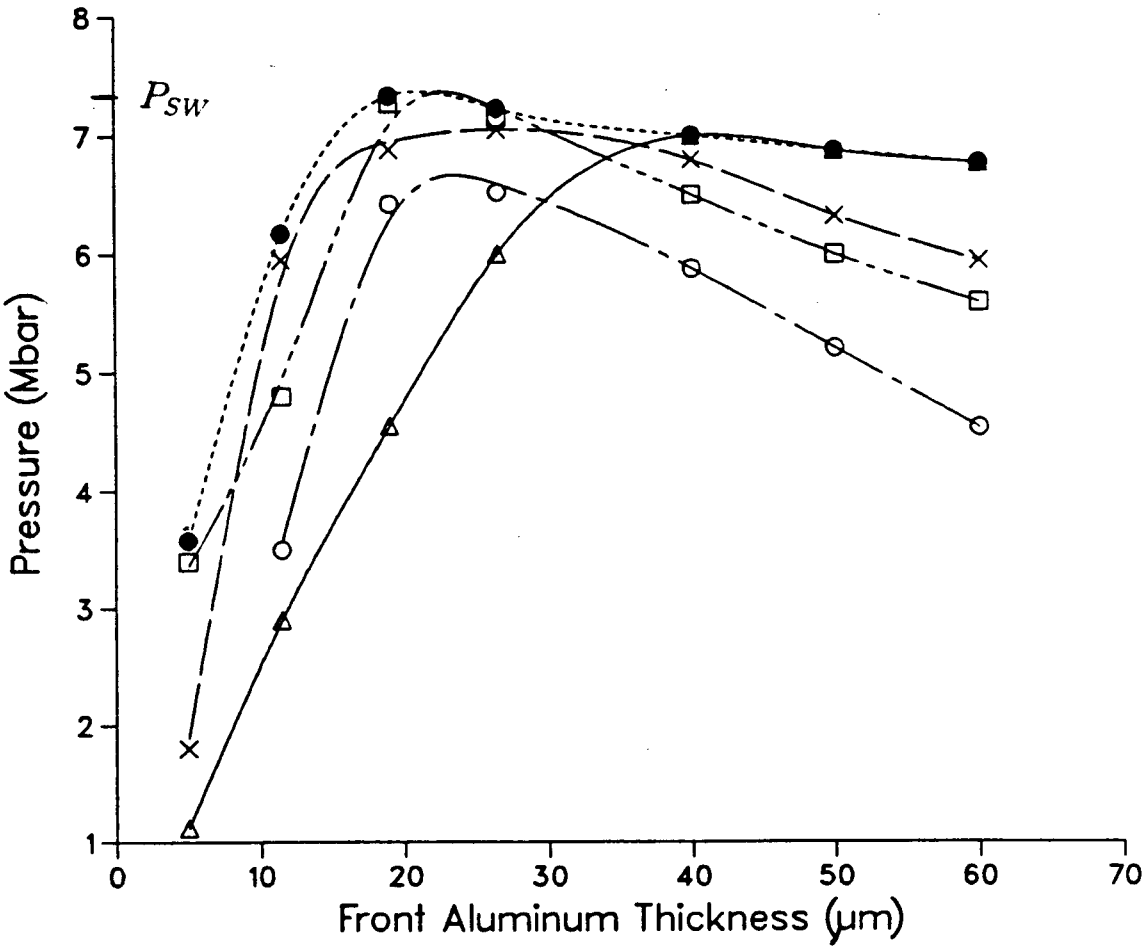


Figure 4.25: Shock induced pressure in the free surface of gold as a function of the aluminum thickness. The various lines denote different gold thicknesses: 2 $\mu$m (solid), 8.4 $\mu$m (dash), 13 $\mu$m (dot-dot-dot-dash), 20 $\mu$m (dot-dash). Also shown is the maximium pressure reached somewhere in a gold layer of infinite thickness (dot)

on $CH_2$-aluminum targets irradiated by modified Gaussian pulses of 1.06 $\mu$m as well as that of Kausik and Godwal[114] with $CH_2$-platinum targets and 1.06 $\mu$m laser pulses. In addition to aasessing pressure enhancement, they concluded that pressure maximization at the interface can be achieved by optimizing the thickness of the standard.

However, as it is not possible to measure directly the pressure at the interface, we shall instead adopt another criterion. Taking the optimization criterion as one of maximum pressure at the free surface of the gold layer and referring to Figure 4.25, one can see that for every gold layer thickness, there exists a corresponding optimal thickness in the aluminum layer. For example, the optimal aluminum thickness for a 2 $\mu$m gold layer is about 40 $\mu$m, while in the case of an 8.4 $\mu$m gold layer, one would choose an aluminum layer of about 26 $\mu$m. Note that the peak pressures achieved at the free surfaces in the above two cases are never as high as $P_{SW}$. This is because the front aluminum layers are already thick enough to allow shock attentuation to occur. Similarly, if the gold layer is 20 $\mu$m thick, then the optimal aluminum thickness is around 23 $\mu$m. Once again, $P_{SW}$ is not reached at the free surface since, in this case, the rear gold layer is too thick and shock damping dominates.

Is the best optimization then achieved when the formation of the strong shock occurs at the instant when it reaches the interface? If so, the best solution would seem to be solely dependent on the front aluminum thickness, given an initial driving pulse. This would be the case if one were to derive the maximum interface pressure[114], and is satisfied (i.e. $P_{SW}$ is reached) when the aluminum thickness approximately equals to 19 $\mu$m as seen in Figure 4.23. However, from Figure 4.25, it is clear that setting the aluminum thickness to be 19 $\mu$m is no guarantee that the optimal pressure $P_{SW}$ would be induced at the free surface of the gold layer. This is because the gold layer also plays a significant role in determining the final pressure attained at its free surface. This point is best illustrated in Figure 4.26, where the shock pressure at the free surface is plotted

against the thickness of the gold layer, with the aluminum thicknesses ranging from 11.5 to 50 $\mu$m. The non-uniformity of the shock pressure in the gold layer is evident. For instance, for a 19 $\mu$m aluminum layer, the shock pressure at the free surface of a 2 $\mu$m gold layer is smaller than that in a 8.4 $\mu$m gold layer, which in turn is less than that in a 13 $\mu$m gold layer. This seemingly strange situation of increasing shock pressure with increasing gold layer thickness arises since, notwithstanding the adverse effect of shcok decay which has begun in the front aluminum layer (cf. Figure 4.23), the shock front continues to steepen as it propagates in the gold layer, culminating in a shock front of greater amplitude. Of course, this process cannot carry on indefinitely as shock attentuation must eventually dominate once the frontside rarefaction wave catches up with the shock, and the pressure is not sustained. This can be seen by comparing the pressure at the free surface in the case of a 11.5 $\mu$m Al on 8.4 $\mu$m Au target with that of a 11.5 $\mu$m Al on 13 $\mu$m Au target (Figure 4.22), where shock damping starts to take over at a depth of $\sim$9 $\mu$m in the gold layer. In fact, if the front aluminum layer were already too thick (such as 50 $\mu$m in Figure 4.24), the free surface pressure in gold will decrease monotonically with increasing gold thickness. Thus pressure maximaization is a rather involved process, and one needs to take into account both the front and back layer thicknesses of the target.

Figure 4.26 also serves to bring up another interesting point, namely the role of shock uniformity in determining optimal thicknesses. The present criterion of having a maximum pressure at the free surface will not be appropriate if one's aim is EOS study, where it is more desirable to have an as uniformly compressed region as possible, i.e. as uniform a shock as possible. A nonuniformly shocked material experiences density and temperature gradients, consequently affecting measurements such as shock transit times. From this point of view a 34 $\mu$m aluminum front layer in an aluminum-on-gold target yields the most uniform shock pressure in gold extending from 2 to 13 $\mu$m, although at

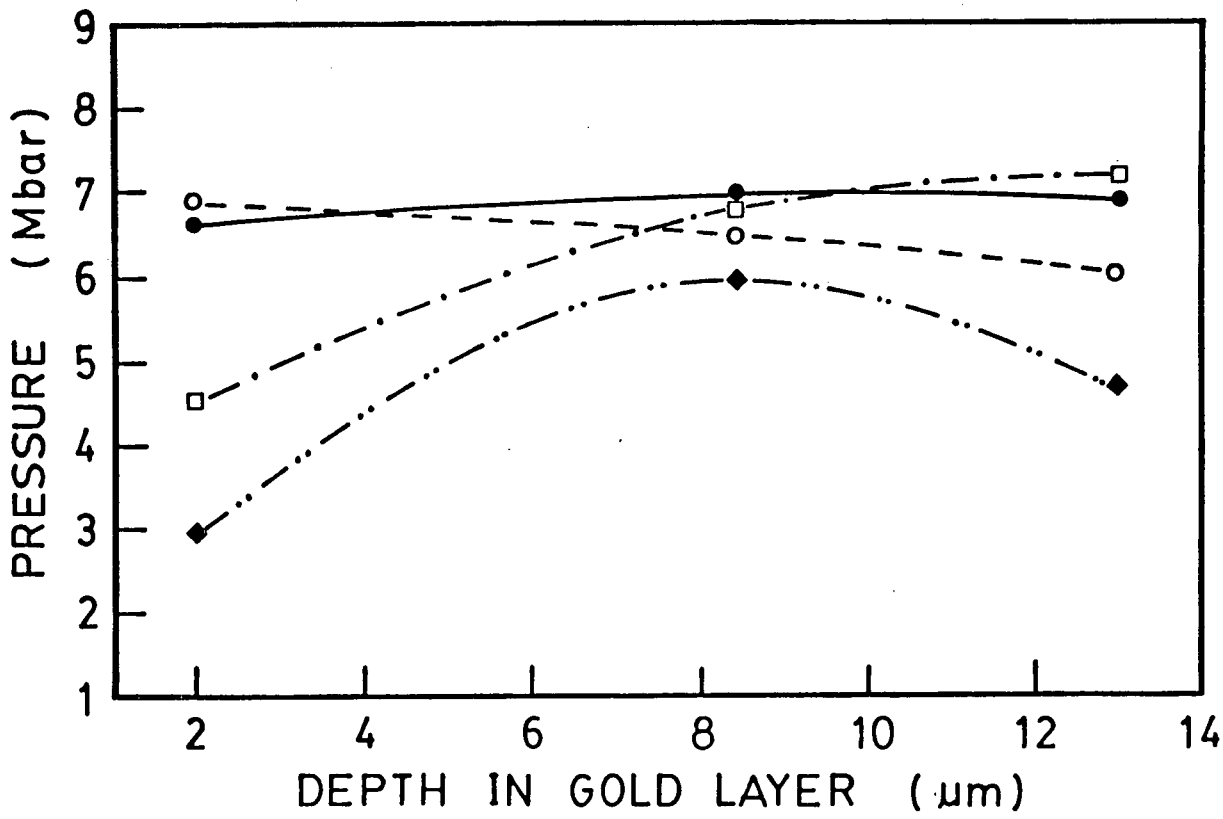


Figure 4.26: Shock pressure at the free surface of gold as a function of thickness in the gold layer for various front aluminum thicknesses: 11.5 $\mu$m (dot-dot-dash), 19 $\mu$m (dot-dash), 34 $\mu$m (solid), and 50 $\mu$m (dash)

the expense of lower free surface pressure.

In summary, we have seen that thickness optimization in an impedance-mismatched target needs to adopt different criteria depending on whether the free surface pressure is to be maximized, or whether the shock pressure is to be as uniform as possible. In addition, we have found that both the front aluminum and the rear gold layer play a role in the pressure evolution, and must both be taken into account.

**4.1.2.B.ii HYRAD Simulations** In this part of the simulations, we calculate the shock trajectories in 19 or 26.5 $\mu$m aluminum on 8.4 or 13 $\mu$m gold using HYRAD including the process of radiation transport. We have performed the simulations using two different EOS models of gold: SESAME and the new calculation incoporating melting transition. Figure 4.27 shows the calculated shock trajectories together with the measured shock transit times for various targets. The agreement between experimental data and both calculated shock paths is good, indicating the validity of both EOS models for gold, at least insofar as shock velocity is concerned.

## 4.2 Brightness Temperature Study with Aluminum-Gold Targets

Another important thermodynamical parameter characterizing the equation of state of a shocked material is the shock temperature $T$ (which is related to the internal energy $E$ of equation (2.7).) As suggested in §1.1 and §2.4.2, the measurements of $T$ is expected to clarify our understanding of shock melting in gold, and also to place a constraint on the predictions based on various theoretical EOS models. Here we shall refer to the shock

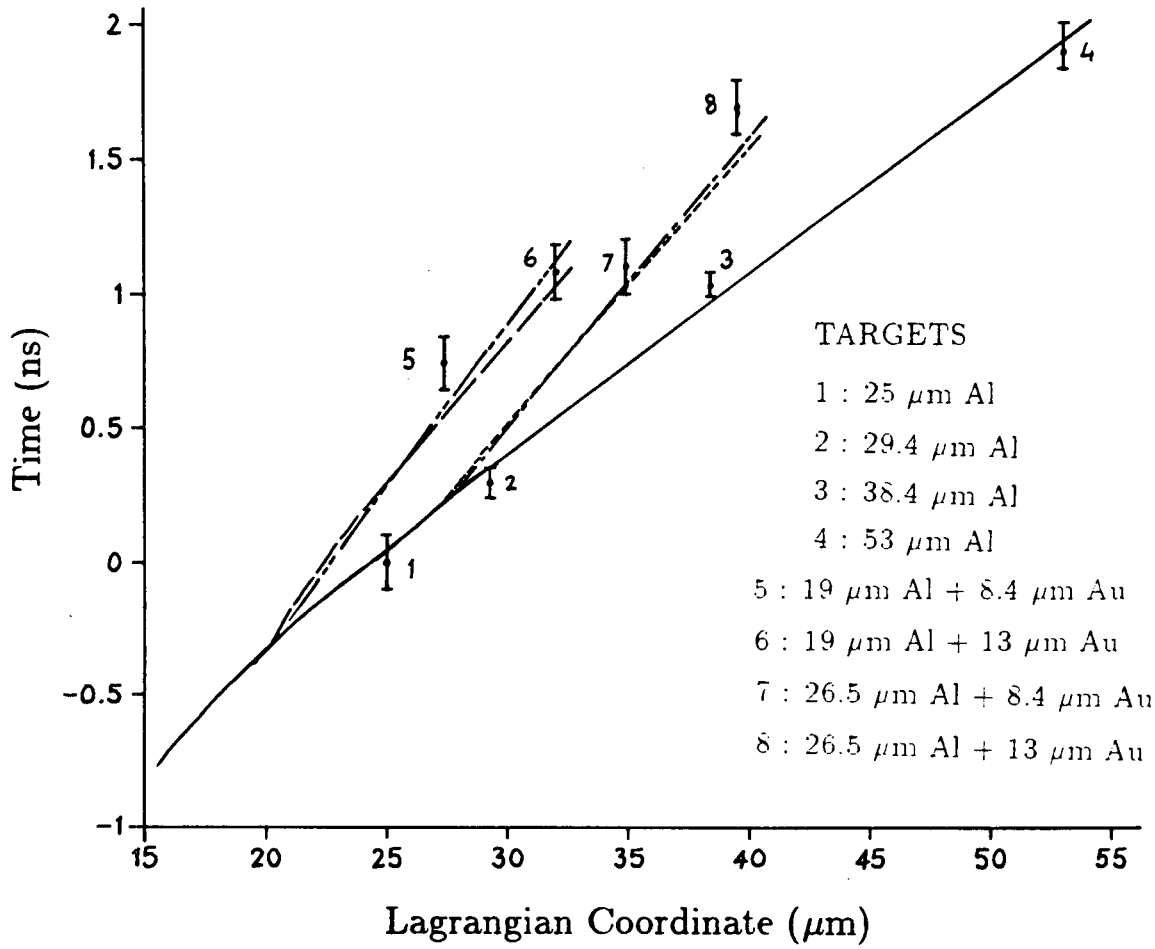


Figure 4.27: Shock paths as calculated by HYRAD in 19 $\mu$m Al and 13 $\mu$m Au target using SESAME EOS (dot-dot-dash), and using new gold EOS (dash); in 26.5 $\mu$m Al and 13 $\mu$m Au target using SESAME EOS (dot-dash), and using new gold EOS (dot). The shock path in 53 $\mu$m Al (solid) is included. Also plotted are the experimental points for various Al-Au targets and pure Al targets.

temperature as the brightness temperature because it is obtained from the intensity of the shock-induced luminous emission. This measurement technique has previously been used to yield temperature data in aluminum[109] and liquid argon[115].

### 4.2.1 Experimental Observations

In this experiment, the brightness temperature is inferred from measurements of the intensity of the shock-induced luminescence at the free surface of the target. The emission is recorded by the streak camera at a faster streak speed than that used in the shock transit time measurements in §4.1 since we are primarily concerned with the measurement of the luminous emission at very early times to reduce the effect of the opacity of the plasma expanding from the free surface into the surrounding vacuum.

Measurements are made in targets with a 19 or 26.5 $\mu$m aluminum layer on either an 8.4 or 13 $\mu$m gold layer. These four targets are expected to achieve almost the highest shock pressure in gold (see Figure 4.25). We have also obtained data for 38.4 $\mu$m pure aluminum targets, which will serve as the EOS standard. Figures 4.28 to 4.32 show the typical time-resolved and time-integrated emission from a pure 38.4 $\mu$m Al foil, a 19 $\mu$m Al on 13 $\mu$m Au target, a 19 $\mu$m Al on 8.4 $\mu$m Au target, a 26.5 $\mu$m Al on 8.4 $\mu$m Au target, and a 26.5 $\mu$m Al on 13 $\mu$m Au target respectively. No significant hot spots are observed in the shock breakoput regions. The typical rise times in the intensity of the shock-induced luminous emission are found to be ~250 ps, which can be attributed to the combined effects of surface roughness (~60 ps), irradiation nonumiformity (~600 ps), and streak camera entrance slit height (~80 ps). The subsequent rapid decrease in the intensity results from the rearside material being released by the rarefaction wave, which forms an optically thick medium attentuating the radiation from the hot material behind[116].

In our study, we have taken advantage of the fact that both our measurements on

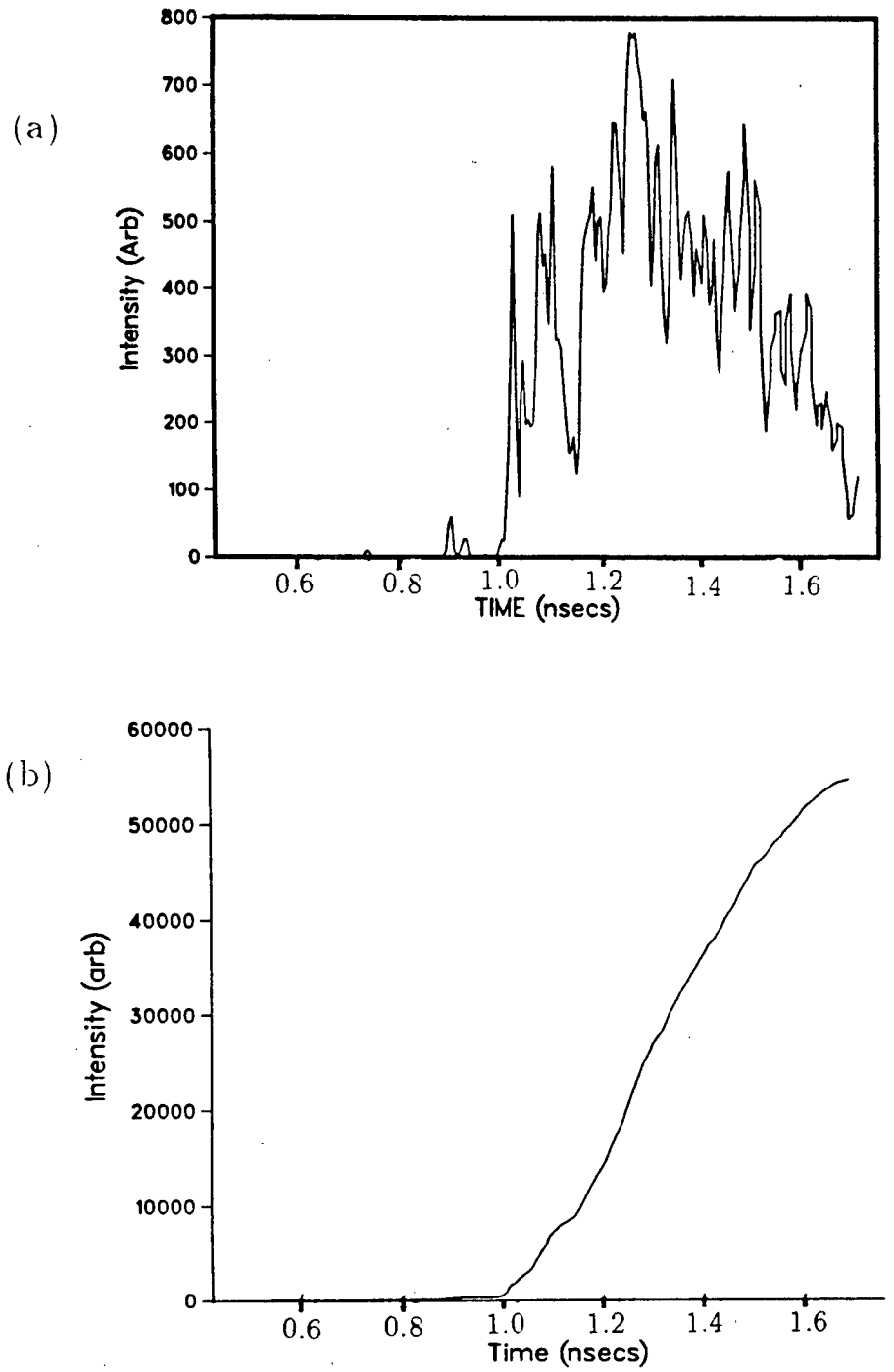


Figure 4.28: Temporally resolved and integrated plot of the backside emission intensity of a 38.4 $\mu$m Al target, with time zero being the peak of the laser pulse.

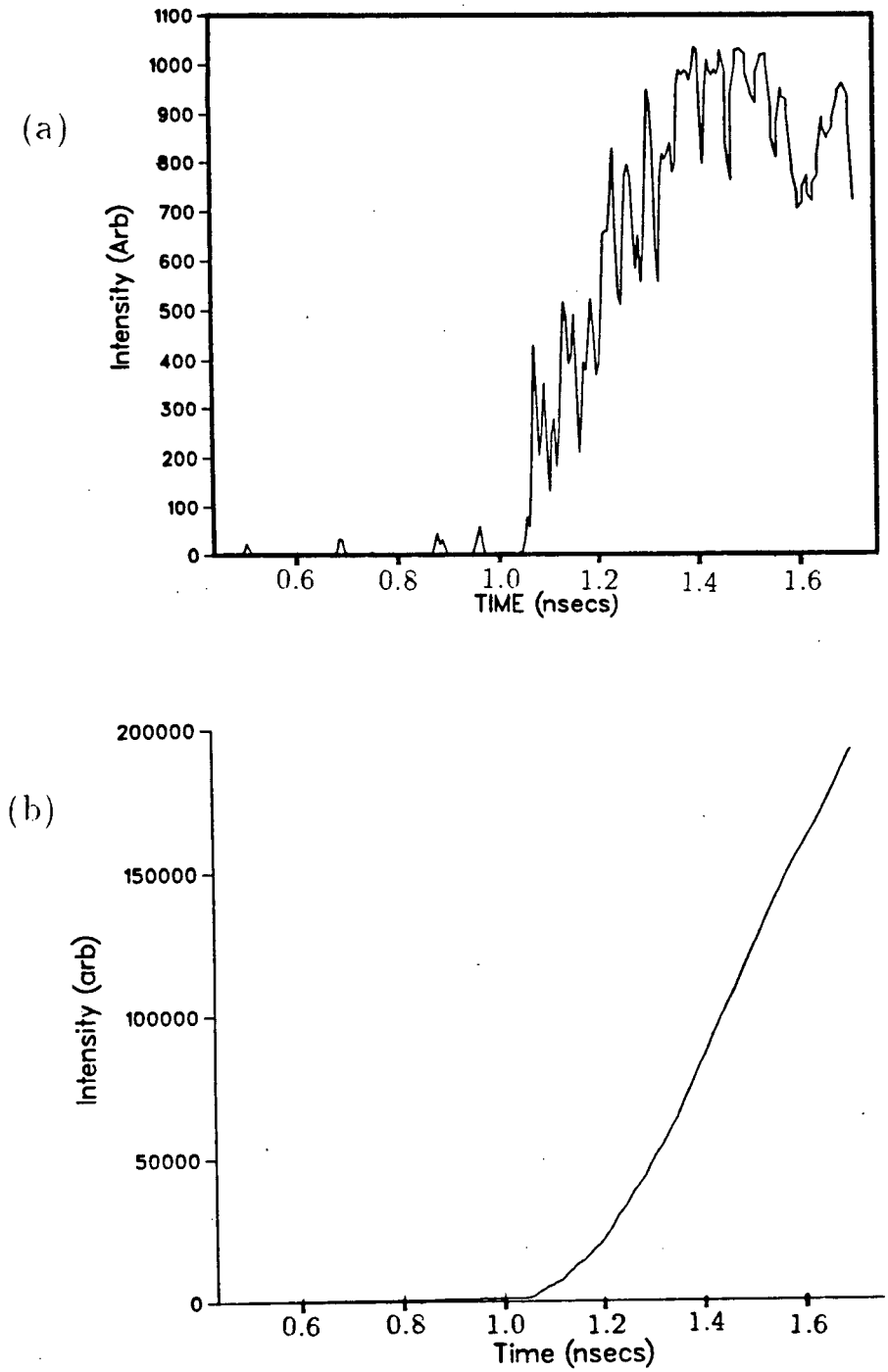


Figure 4.29: Same as Figure 4.28except target is 19 $\mu$m Al on 13 $\mu$m Au

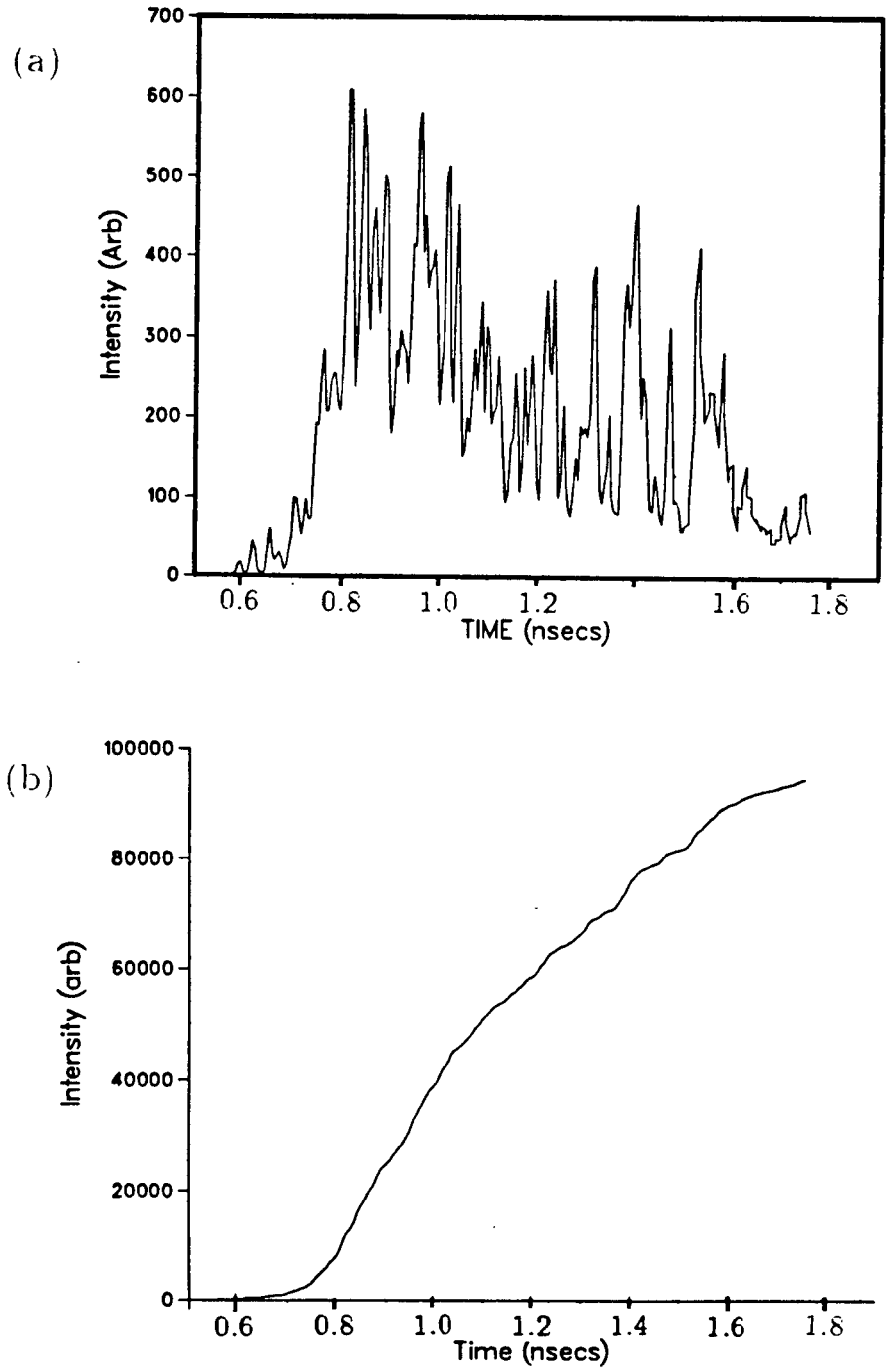


Figure 4.30: Same as Figure 4.28except target is 19 $\mu$m Al on 8.4 $\mu$m Au

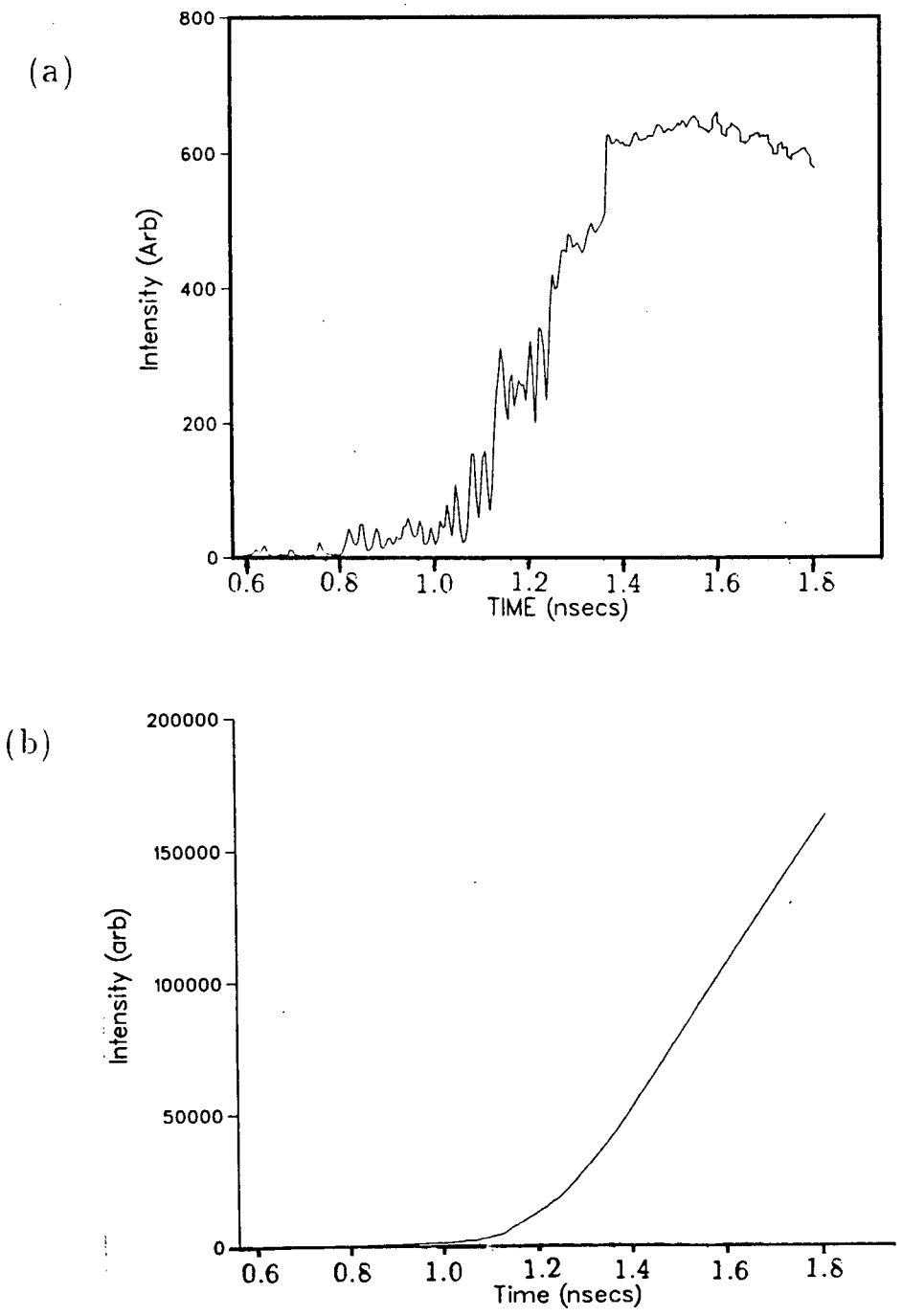


Figure 4.31: Same as Figure 4.28except target is 26.5micron Al on 8.4 $\mu$m Au

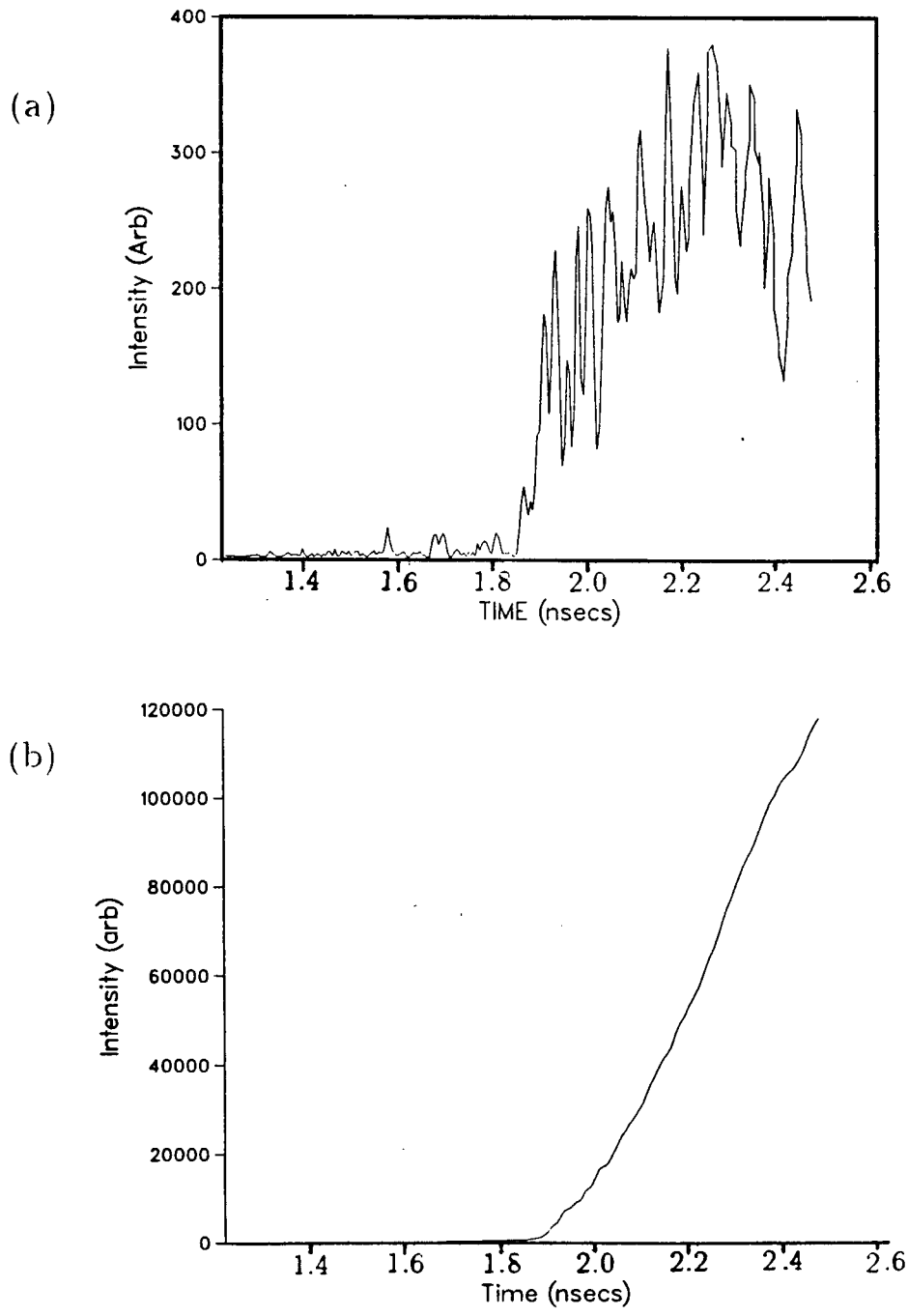


Figure 4.32: Same as Figure 4.28except target is 26.5 $\mu$m Al on 13 $\mu$m Au

the single and double layered targets are done using the same imaging system, and that the shock breakout regions in both types of targets are similar. Therefore, knowing the temperature of the shock-heated aluminum, the brightness temperature of gold can be obtained by comparing the intensity of emission from gold to that from aluminum, without the need for an absolute intensity calibration of the streak camera and optics system. From Figures 4.28 to 4.32, it can be seen that the instantaneous emission intensity is highly spiky and modulated, consequently the ratio of the emission intensity cannot produce any meaningful results. On the other hand, the ratio of the time-integrated intensity does allow for an objective and umambiguous analysis of the data.

### 4.2.2 Computer Simulations

The simulation of this experiment is performed in two steps. First, we use the HYRAD code to follow the entire history of the target from the onset of the laser pulse to the time of shock arrival at the free surface. Then, to simulate properly the measurement of the shock-induced luminous emission from the target rear surface, the PUC code is used to calculate the emission intensity from the rarefying plasma at the rear side of the target as detected by the streak camera.

#### 4.2.2.A HYRAD Simulations

HYRAD is used since it allows for not only a more complete treatment of the laser-target interactions, but also the possibility of accessing the effect of radiation transport in the experiment. In the code, the EOS of aluminum is obtained from the SESAME data library, and the atomic physics model has been described in §2.4.1. For gold, the atomic and opacity data used are taken from the SESAME library, but two sets of EOS data (SESAME and the new solid/liquid state calculation) are used. The spatial resolution in these simulations is less than 0.25 $\mu$m.

**4.2.2.A.i Effect of Radiation Transport** In this section we consider the effects of radiation transport in more detail, and examine the shock profiles in a 19 $\mu$m Al on 13 $\mu$m Au target using SESAME EOS data, emphasizing on how radiative transfer may affect the shock temperature. Radiative heating is expected to play only a minor role in the gold layer as already remarked in section §2.3.2. Figures 4.33 shows the spatial profiles of density, pressure, and temperature at a time of 1.26 ns before the laser peak when the process of radiation transport is neglected (henceforth referred to as case [A]). Figure 4.34 shows simular profiles in the presence of radiation transport (case [B]). The shock front is marked by a sharp increase in density, pressure and temperature (which occurs at a depth of $\sim$10 $\mu$m in the target in figures 4.33 and 4.34). We note that the different initial temperatures, 400K in Al and 130K in Au, are necessary due to limitations in the models of the ground state temperature in the SESAME data, and are chosen so that the initial pressures in both materials are the same. Therefore the initial temperature difference in the two materials does not signify a real temperature discontinuity at their interface. We have also indicateded the X-ray power absorption profile in the target in Figure 4.34. We see that although most of the X-ray energy is deposited in the first 7 $\mu$m of the aluminum layer, some radiation is deposited well into the target also, even ahead of the shock front and hence preheating the aluminum (note the slight temperature and pressure increase above ambient temperature and pressure in aluminum ahead of the shock). Consequently, the temperature gradient is less in case [B] than [A]. This preheating of the cold aluminum layer ahead of the shock front will not have been desirable in EOS studies since the pre-shocked state of a material will depend on the radiation transport process. Also, due to the large opacity increase of gold over aluminum (e.g. at 1 keV, opacity of gold is five times that of aluminum), gold is a much better absorber of radiation than aluminum and the remaining X-radiation is deposited in the first 2 to 3 $\mu$m of the gold layer. There is still preheating in gold, but the level is

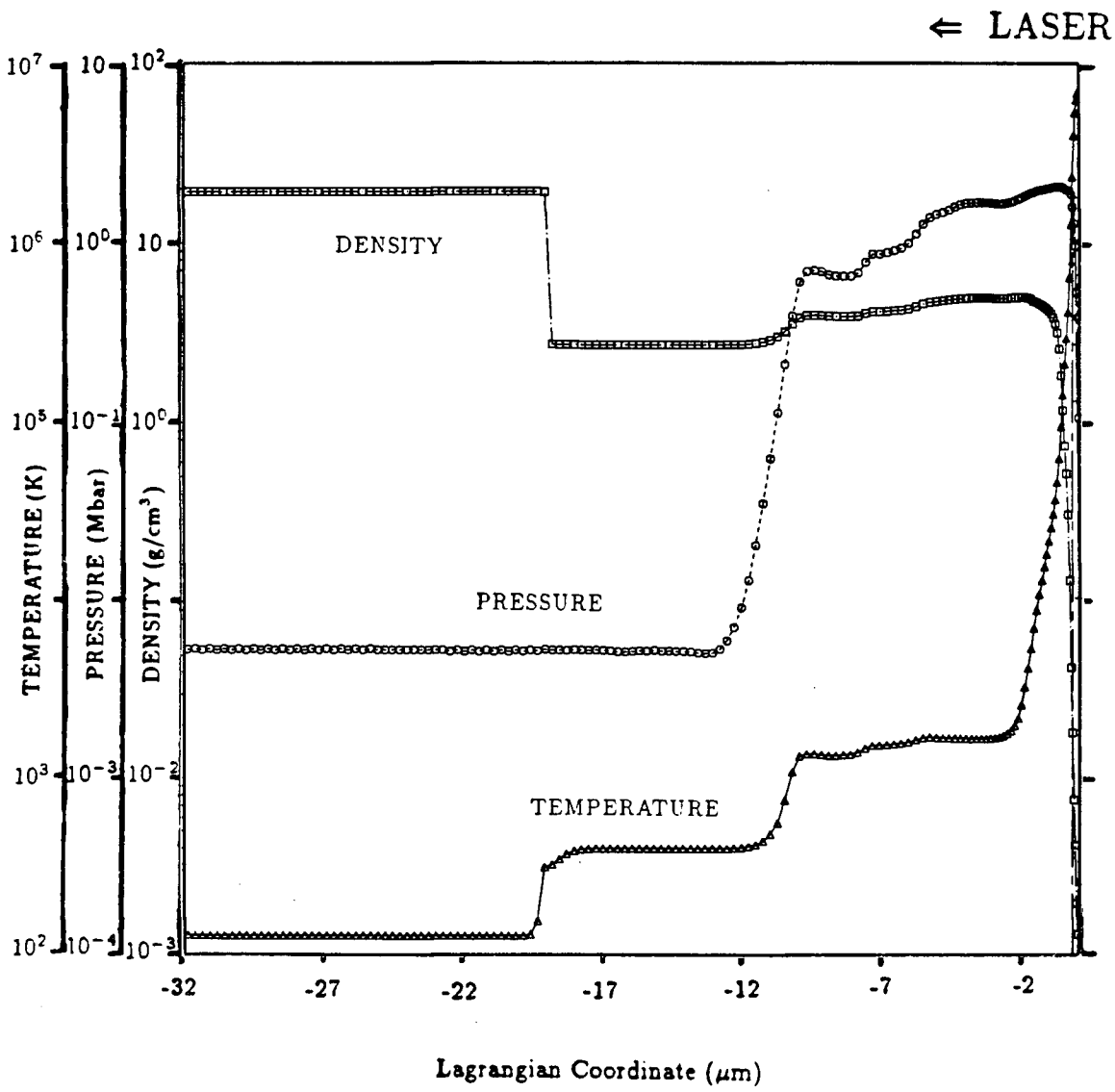


Figure 4.33: A snapshot of the hydrodynamic profile in a 19 $\mu$m Al on 13 $\mu$m Au target at t = -1.26 ns. Radiation transport process is neglected, and both Al and Au EOS data are from SESAME.

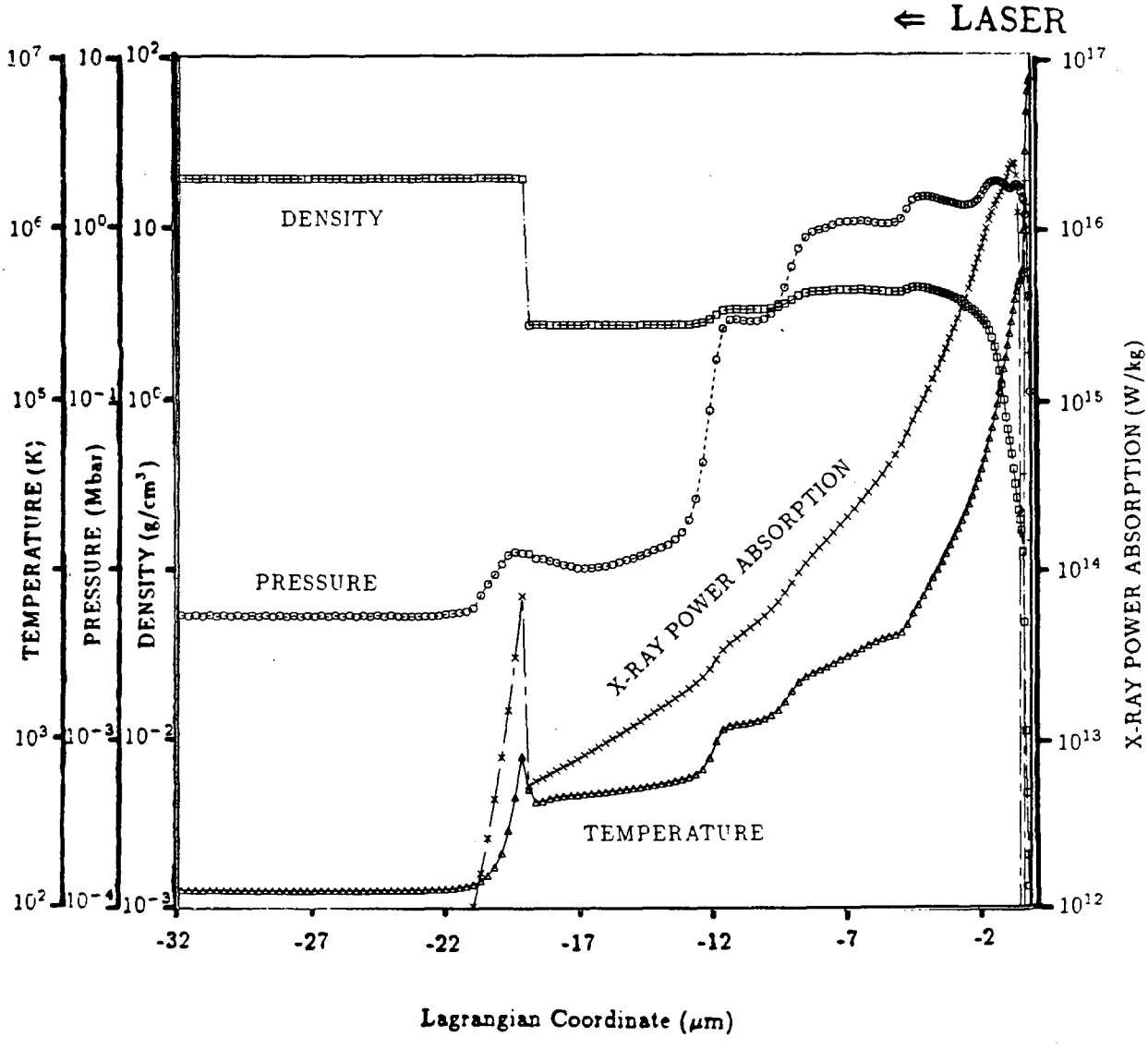


Figure 4.34: Same as Figure 4.33 except radiation transport process is included. The absorbed X-ray power is also plotted.

very low since most of the radiation have been absorbed in aluminum, and the extent of the preheated region is very small.

Next, we show in figures 4.35 and 4.36 the corresponding two cases at 0.24 ns after the laser peak when the shock has crossed the aluminum-gold interface into the gold layer. As before, the gradient in the temperature profile in case [B] is more gradual than in case [A] due to radiation deposition. We also note the pressure continuity across the interface, as required by the boundary condition. A decrease of the shock pressure, temperature, and to a lesser extent, density, in case [B] can also be observed as a result of radiative energy loss from the hot plasma leading to a lower ablation pressure. Finally, the shock front has propagated past the first few microns of the gold layer where there is X-ray energy absorption. As a result, radiation transport no longer constitutes a preheat problem, and the subsequent shock structure become much more well-defined, comparable to that in case [A]. In this manner we have achieved a "clean" shock, i.e. a quasi- steady shock entering the cold material without significant preheat. The advantage of the impedance mismatch method in radiative preheat suppression in high-Z material is realized.

Table 4.1 summarizes results of the simulations at the time of shock breakout at the free surface of gold. We should emphasize the significant drop in shock temperature ($\sim$23%) as radiation transport is taken into account, and this should lead to a corresponding decrease in the rear surface emission.

**4.2.2.A.ii EOS Models** In this section we will compare the effects of the two different EOS models of gold on the shock parameters in the same 19 $\mu$m Al on 13 $\mu$m Au target. The two EOS models of gold are respectively the SESAME tabulated data and the new calculation incoporating the melting transition. Table 4.2 presents the simulation results. We see similar qualitive behavior in the shock propagation, but the

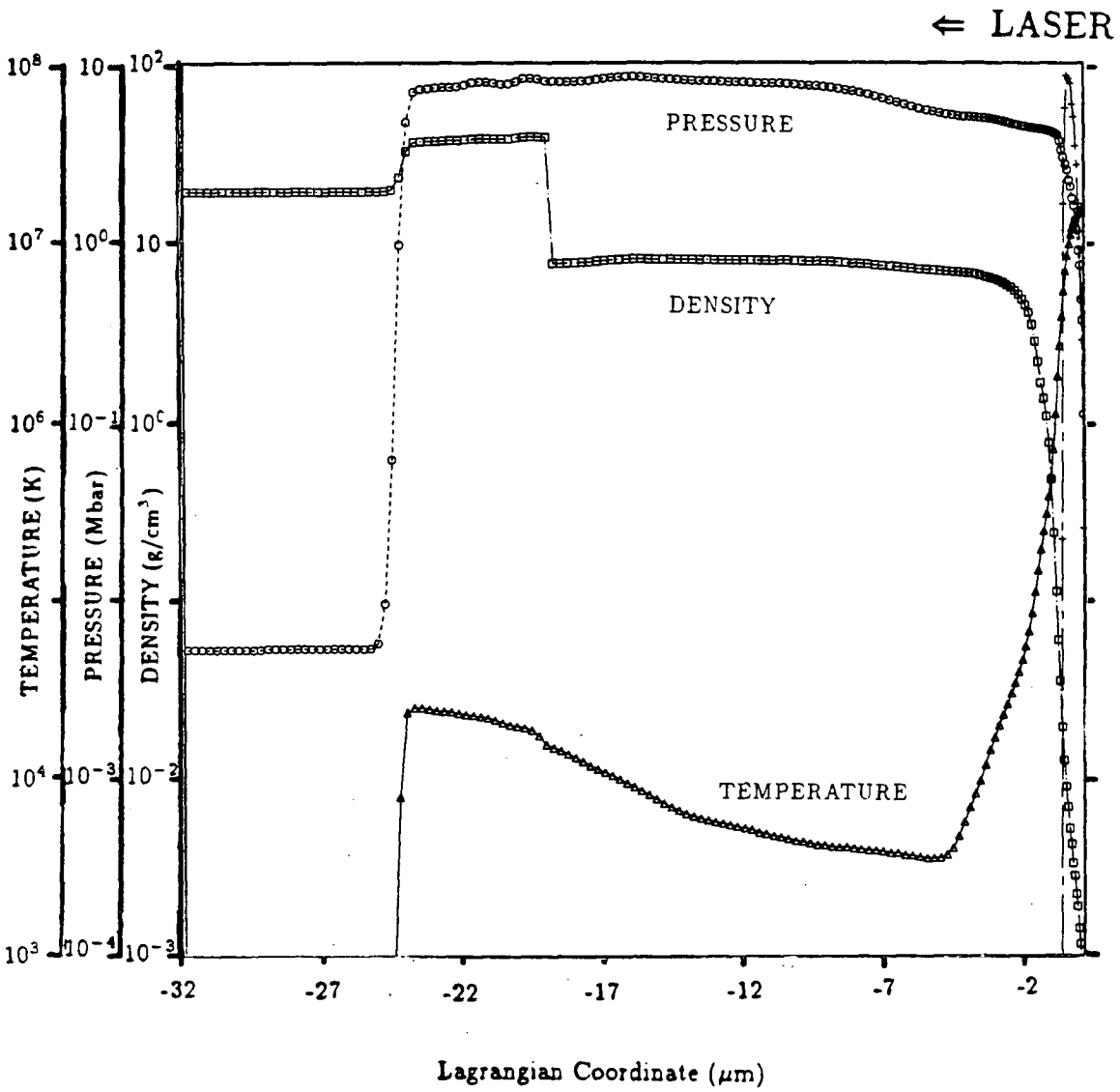


Figure 4.35: Same as Figure 4.33 except time is at t = 0.24 ns

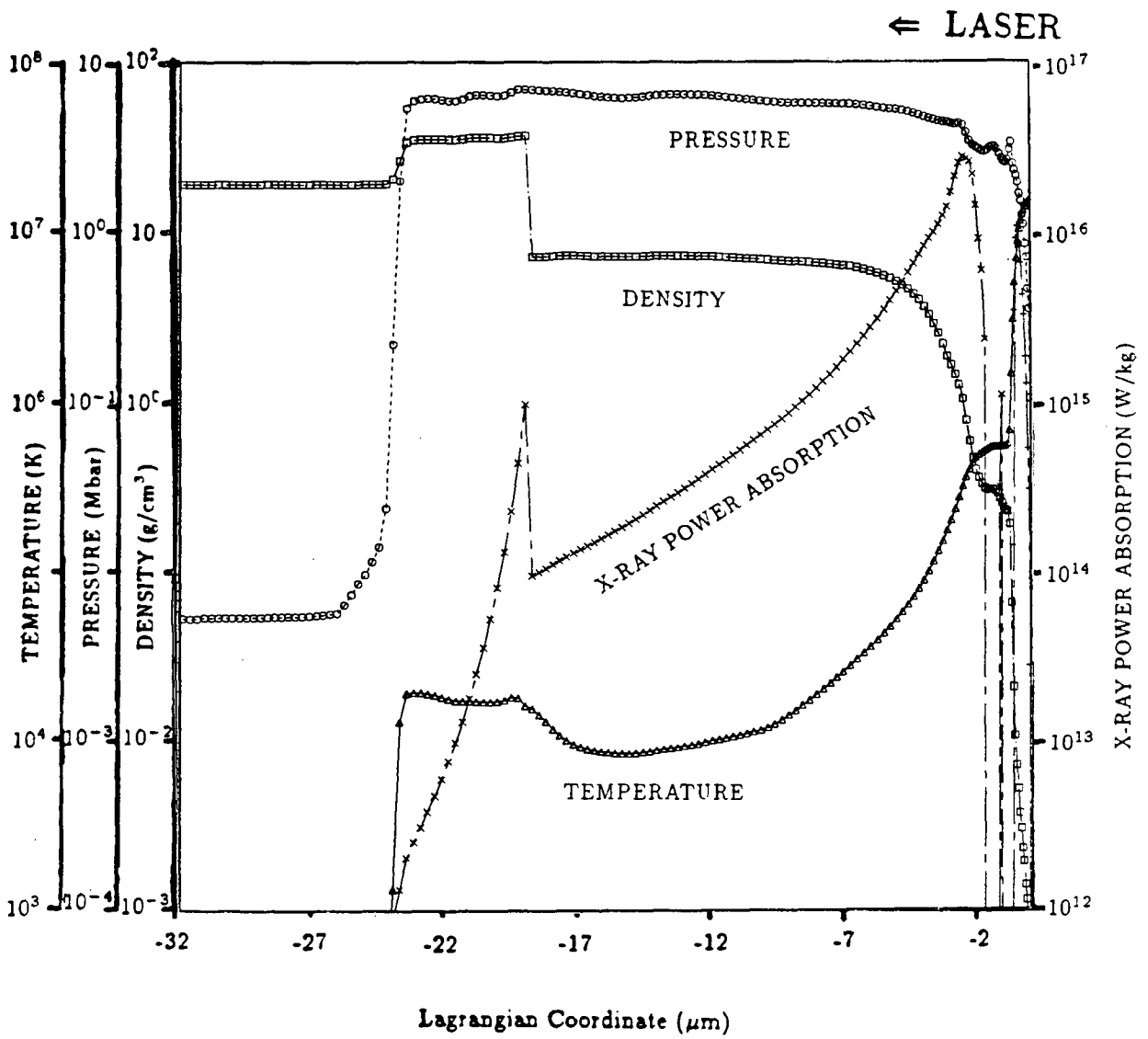


Figure 4.36: Same as Figure 4.35 but radiation transport process is included

| $\Phi$ = 2.3 x $10^{13}$ W/cm$^2$ | No Radiation Transport | With Radiation Transport |
|---|---|---|
| steady shock velocity in gold (x $10^6$ cm/s) | 0.88±0.02 | 0.85±0.02 |
| shock breakout time (ns) | 1.08±0.02 | 1.19±0.02 |
| shock breakout compression ratio | 1.86±0.05 | 1.80±0.05 |
| shock breakout pressure in gold (Mbar) | 7.1±0.2 | 6.0±0.2 |
| shock breakout temperature in gold (eV) | 2.46±0.04 | 2.00±0.04 |

Table 4.1: comparative study of the effects of radiation transport on free surface shock parameters for a 19 $\mu$m Al on 13 $\mu$m Au target

| $\Phi$ = 2.3 x $10^{13}$ W/cm$^2$ | SESAME Gold data (2700) | New Gold data (2788) |
|---|---|---|
| steady shock velocity in gold (x $10^6$ cm/s) | 0.85±0.02 | 0.95±0.02 |
| shock breakout time (ns) | 1.19±0.02 | 1.04±0.02 |
| shock breakout compression ratio | 1.80±0.05 | 1.71±0.05 |
| shock breakout pressure in gold (Mbar) | 6.0±0.2 | 6.1±0.2 |
| shock breakout temperature in gold (eV) | 2.00±0.04 | 1.54±0.04 |

Table 4.2: comparative study of the effects of our new gold EOS data on free surface shock parameters for a 19 $\mu$m Al on 13 $\mu$m Au target, radiation transport is included

| $\Phi$ = 2.3 x $10^{13}$ W/cm$^2$ | | SESAME Gold EOS | New Gold EOS |
|---|---|---|---|
| 19 $\mu$m Al + 8.4 $\mu$m Au | $t_b$ (ns) | 0.58±0.02 | 0.55±0.02 |
| | $\rho/\rho_0$ | 1.79±0.05 | 1.70±0.05 |
| | $P$ (Mbar) | 5.8±0.2 | 5.9±0.2 |
| | $T$ (eV) | 1.83±0.04 | 1.46±0.04 |
| 26.5 $\mu$m Al + 8.4 $\mu$m Au | $t_b$ (ns) | 1.03±0.02 | 1.02±0.02 |
| | $\rho/\rho_0$ | 1.76±0.05 | 1.68±0.05 |
| | $P$ (Mbar) | 5.4±0.2 | 5.4±0.2 |
| | $T$ (eV) | 1.68±0.04 | 1.28±0.04 |
| 26.5 $\mu$m Al + 13 $\mu$m Au | $t_b$ (ns) | 1.51±0.02 | 1.48±0.02 |
| | $\rho/\rho_0$ | 1.75±0.05 | 1.62±0.05 |
| | $P$ (Mbar) | 5.3±0.2 | 5.3±0.2 |
| | $T$ (eV) | 1.67±0.04 | 1.20±0.04 |

Table 4.3: comparative study of the effects of our new gold EOS data on the shock breakout times ($t_b$), the compression ratio ($\rho/\rho_0$), the shock pressure ($P$), and the shock temperature ($T$) at breakout for various Al-Au targets. Radiation transport is included.

shock breaks out sooner (see Figure 4.27) and the shock temperature is decreased (see Table 4.2). This result we attribute to the "softer" nature of the liquid, as the liquid phase can attain a greater shock velocity under the same pressure than the solid. The lower temperature is also expected since energy is expended during melting without a corresponding temperature increase. Table 4.3 presents the simulation results for the remaining three tagets, which are 19 $\mu$m Al on 8.4 $\mu$m Au, 26.5 $\mu$m Al on 8.4 $\mu$m Au, and 26.5 $\mu$m Al on 13 $\mu$m Au.

### 4.2.2.B PUC Simulations

The second step of the simulation for the brightness temperature study uses PUC to calculate the time evolution of the intensity of emission from the target rear surface at and subsequent to shock breakout. The shock density, pressure, and temperature at the rear surface of the target (aluminum or gold) at breakout as calculated by HYRAD

in §4.1.1.B and §4.1.2.B.ii are used as the initial conditions of the shocked medium in PUC which then calculates the radiation emitted at 4300Å as the target rarefies into the vacuum. The spatial resolution in these calculations is less than 0.05 $\mu$m.

A plot of the rearside emission from gold (from a 19 $\mu$m Al on 13 $\mu$m Au target) and aluminum (from a 38.4 $\mu$m Al target) is shown in Figure 4.37. Here time zero corresponds to the time of shock breakout at the free surface. We have also used both the SESAME and our new gold EOS data. We see that the rearside emission decreases rapidly (dropping 2 orders of magnitude in the first 30 ps). This is because as the rear surface unloads, the expanding cooler material rapidly shields the hot plasma behind, so that the intensity of the emission that can be detected also drops rapidly. Figure 4.38 is a plot of the time-integrated emission for the same two targets. We see that the initial rapid rise in the emission reflects the large amount of radiation at the beginning of the shock unloading. An absolute comparison of the rearside emission intensity between experimental and simulation results cannot be made since an absolute intensity calibration of the streak camera is not made. We have instead compared the ratio of the time-integrated emission intensities for gold to aluminum. The results for 19 $\mu$m Al on 13 $\mu$m Au and 38.4 $\mu$m Al targets are plotted in Figure 4.39(a). We consider those data between 50 to 300 ps to be more reliable, since at very early times we are limited by experimental uncertainties in determining the times of shock breakout, while at late times the effects of the rarefaction wave and the increasing absorption by the released plasma become increasingly more dominant. In addition, we have also best-fitted a measured emission ratio by varying the shock temperature in PUC. The results are shown in Figures 4.39(b). Results from other target sots are presented in Figures 4.40 to 4.42. The results for the remaining 19 $\mu$m Al on 8.4 $\mu$m Au, as well as 26.5 $\mu$m Al on 19 and 8.4 $\mu$m Au targets are plotted respectively in figures 4.43 to 45.

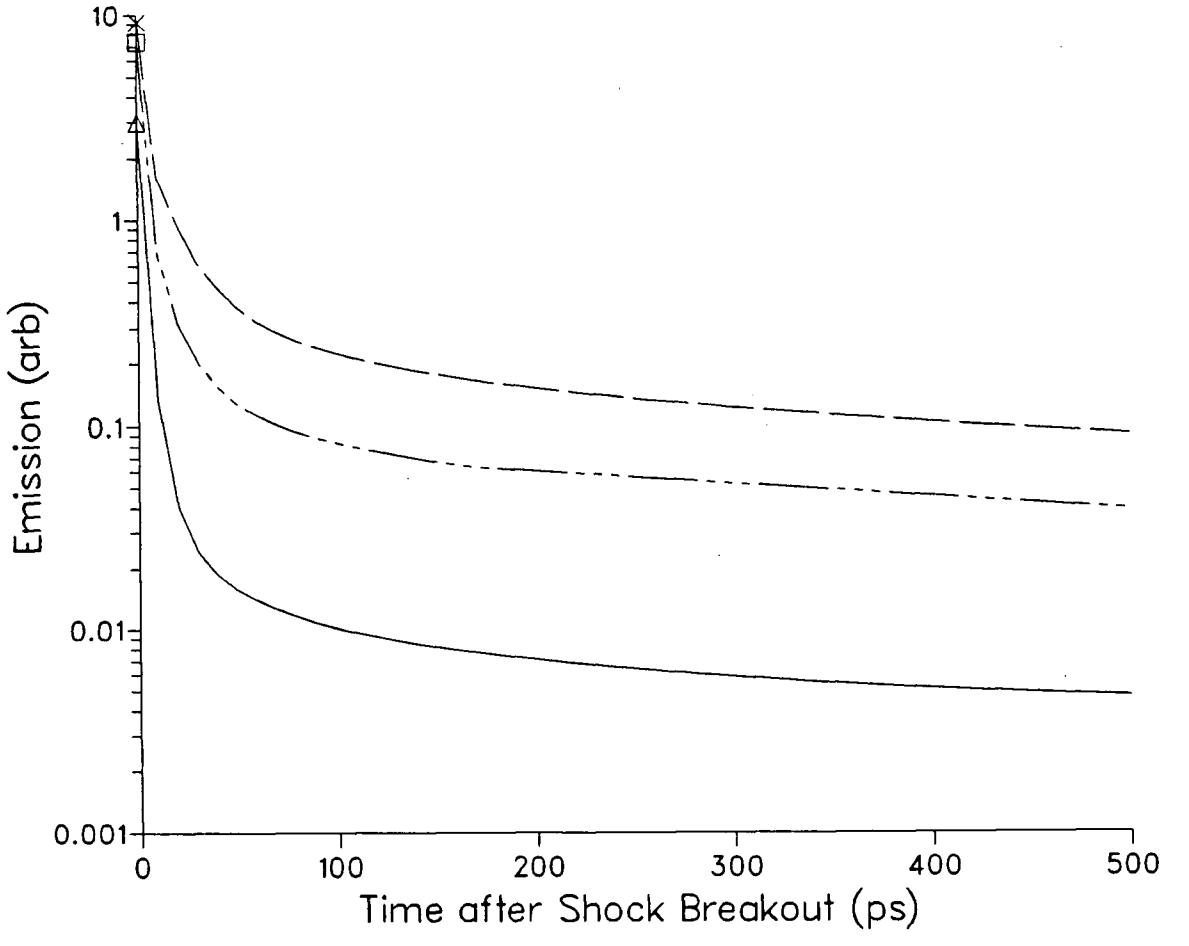


Figure 4.37: Backside emission from a 19 $\mu$m Al on 13 $\mu$m Au target using SESAME (dash) and our new (dot-dot-dot-dash) gold EOS data, as well as from a 38.4 $\mu$m Al (solid) target, with time zero corresponding to shock breakout

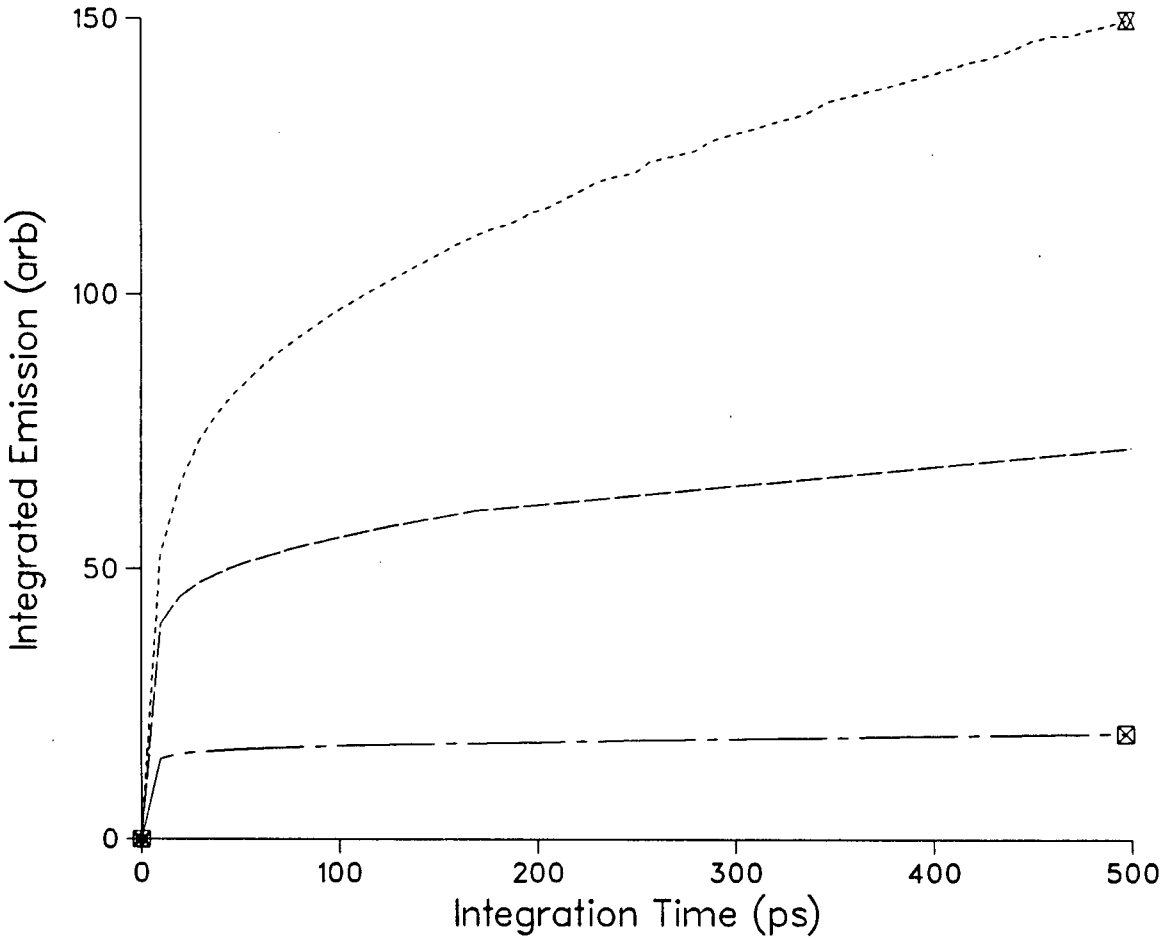


Figure 4.38: Time-integrated emission intensity of the previous Figure 4.37: that of a 19 $\mu$m Al on 13 $\mu$m Au target using SESAME (dot) and the new (dash) gold data; that of a 38.4 $\mu$m Al target (dot-dash).

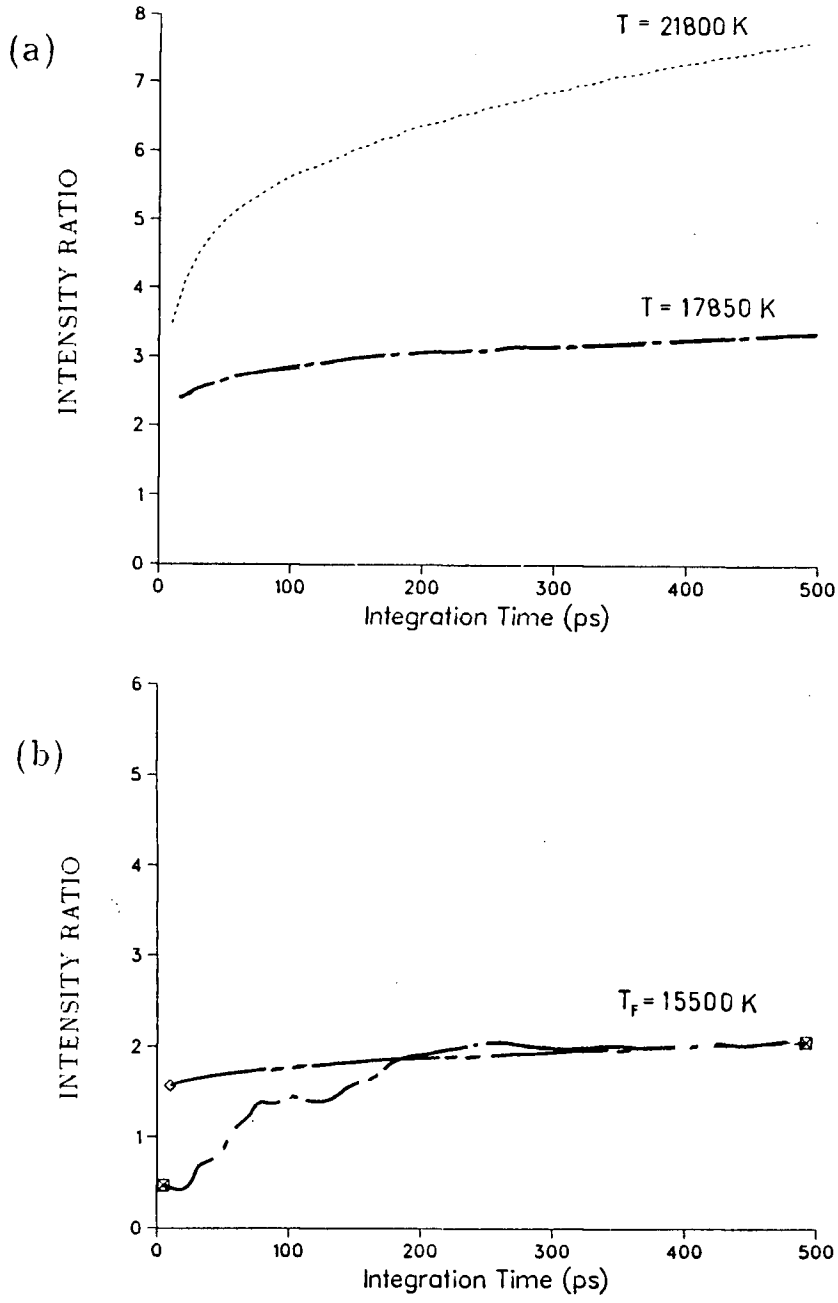


Figure 4.39: Time-integrated emission intensity ratio for a 19 $\mu$m Al on 13 $\mu$m Au target to a 38.4 $\mu$m Al target: (a) using SESAME (dot), and new gold (dot-dash) EOS data; and (b) best-fitted temperature $T_F$ curve (dot-dot-dash) to an experimental curve (dot-dash).

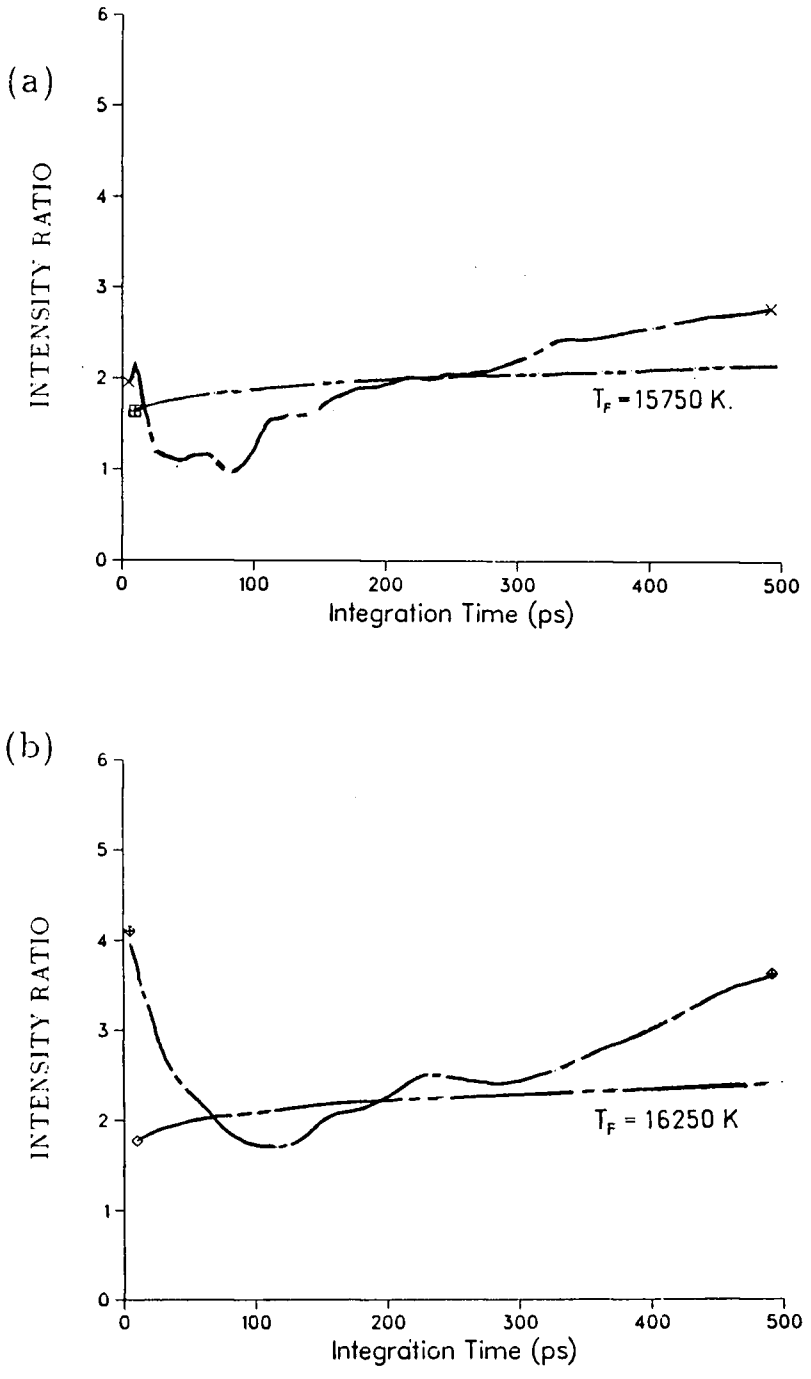


Figure 4.40: Similar to Figure 4.39(b): an experimental time-integrated emission intensity ratio is best-fitted with a shock temperature $T_F$.

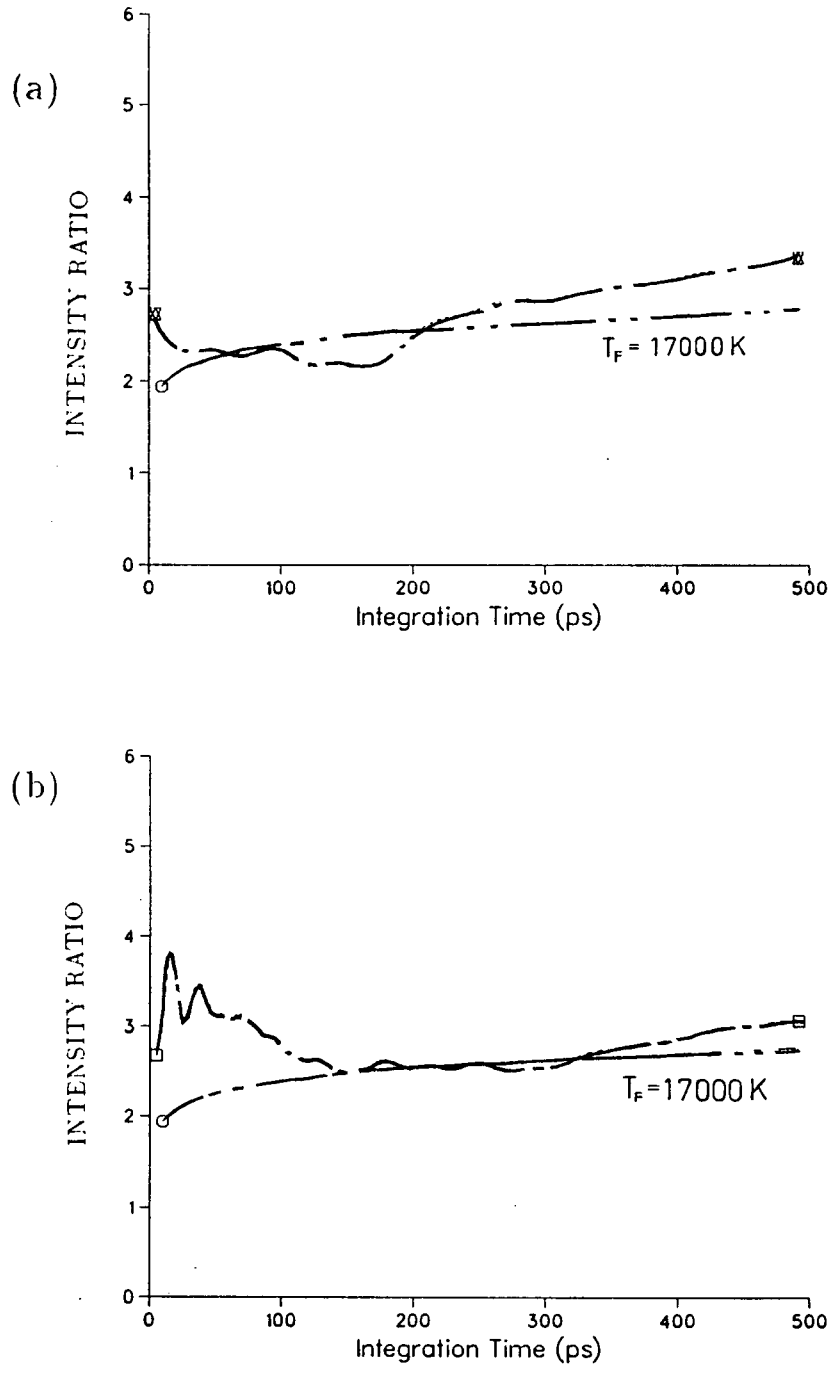


Figure 4.41: Similar to Figure 4.39(b): an experimental time-integrated emission intensity ratio is best-fitted with a shock temperature $T_F$.

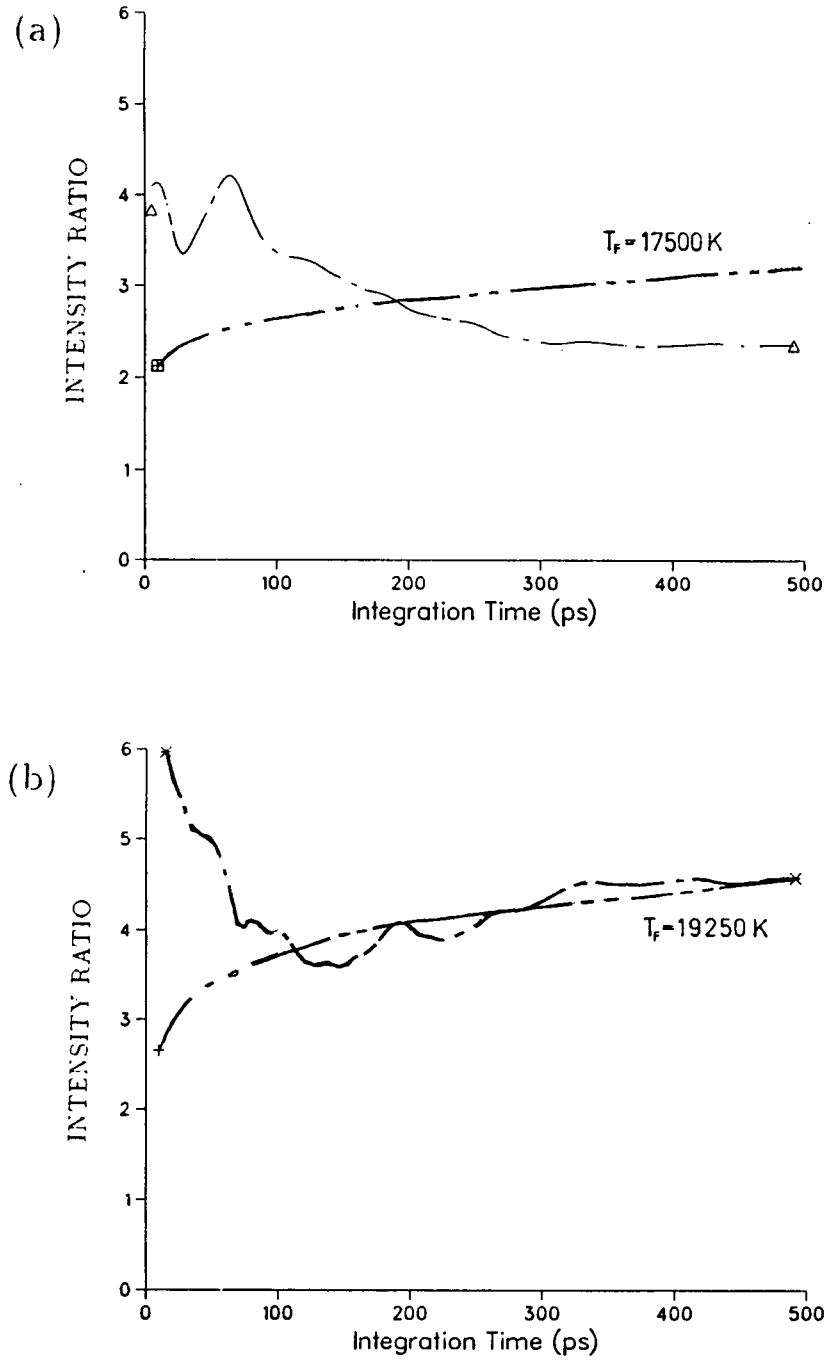


Figure 4.42: Similar to Figure 4.39(b): an experimental time-integrated emission intensity ratio is best-fitted with a shock temperature $T_F$.

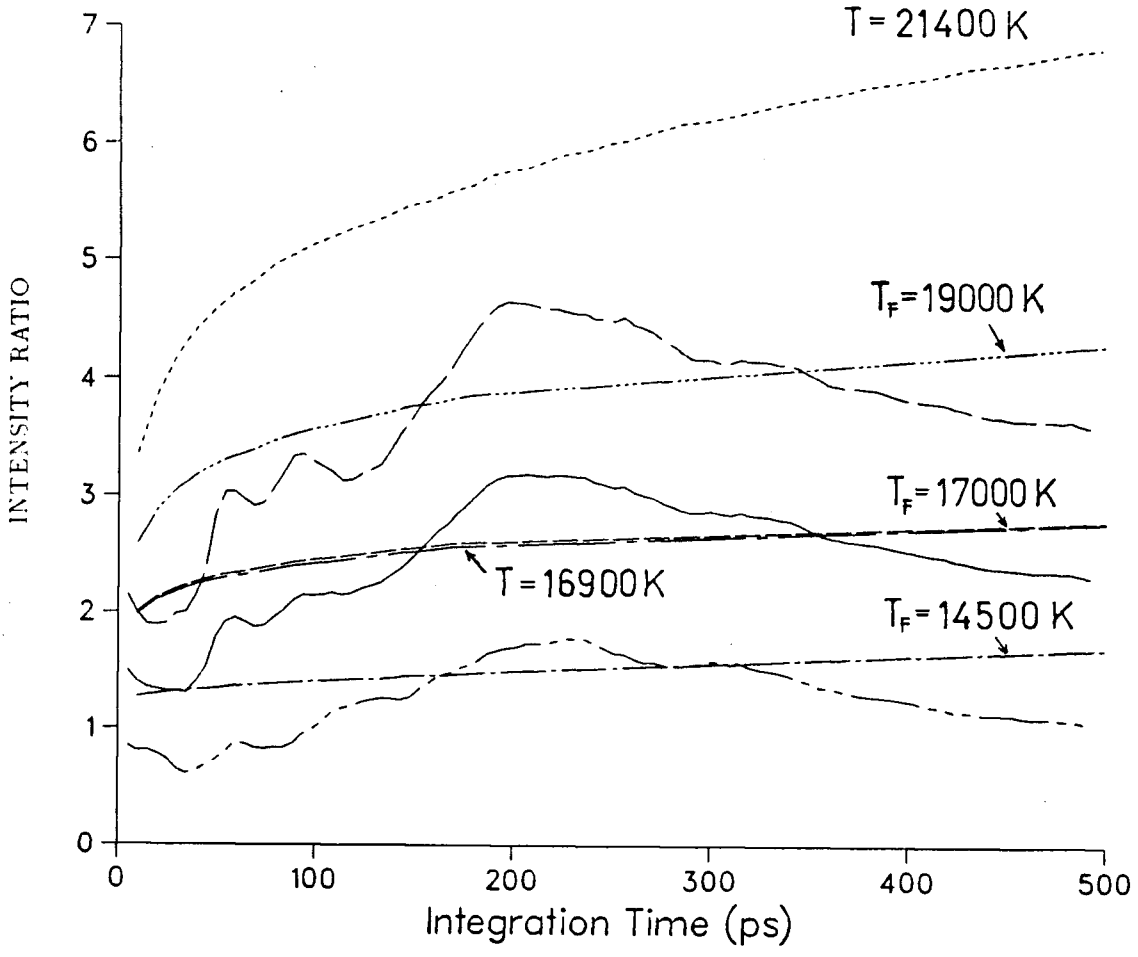


Figure 4.43: Time-integrated emission intensity ratio for a 19 $\mu$m Al on 8.4 $\mu$m Au target to a 38.4 $\mu$m Al target using SESAME (dot), and the new (long dot-dash) gold EOS data. The experimental data (long dash, solid, long dot-dot-dot-dash) are individually best-fitted with a shock temperature $T_F$ (short dot-dot-dot-dash, short dash, short dot-dash)

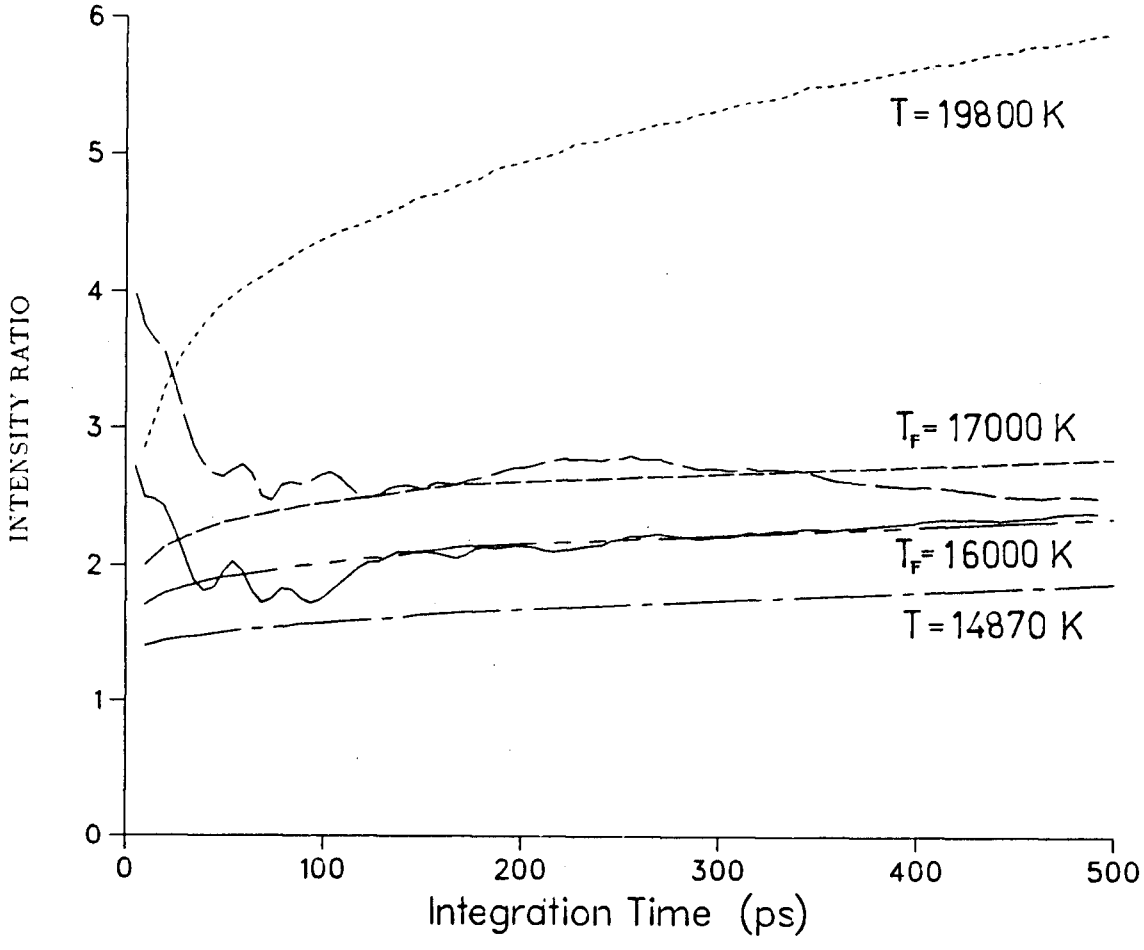


Figure 4.44: Time-integrated emission intensity ratio for a 26.5 $\mu$m Al on 8.4 $\mu$m Au target to a 38.4 $\mu$m Al target using SESAME (dot), and the new (dot-dash) gold EOS data. The experimental data (long dash, solid) are individually best-fitted with a shock temperature $T_F$ (dot-dot-dot-dash, short dash)

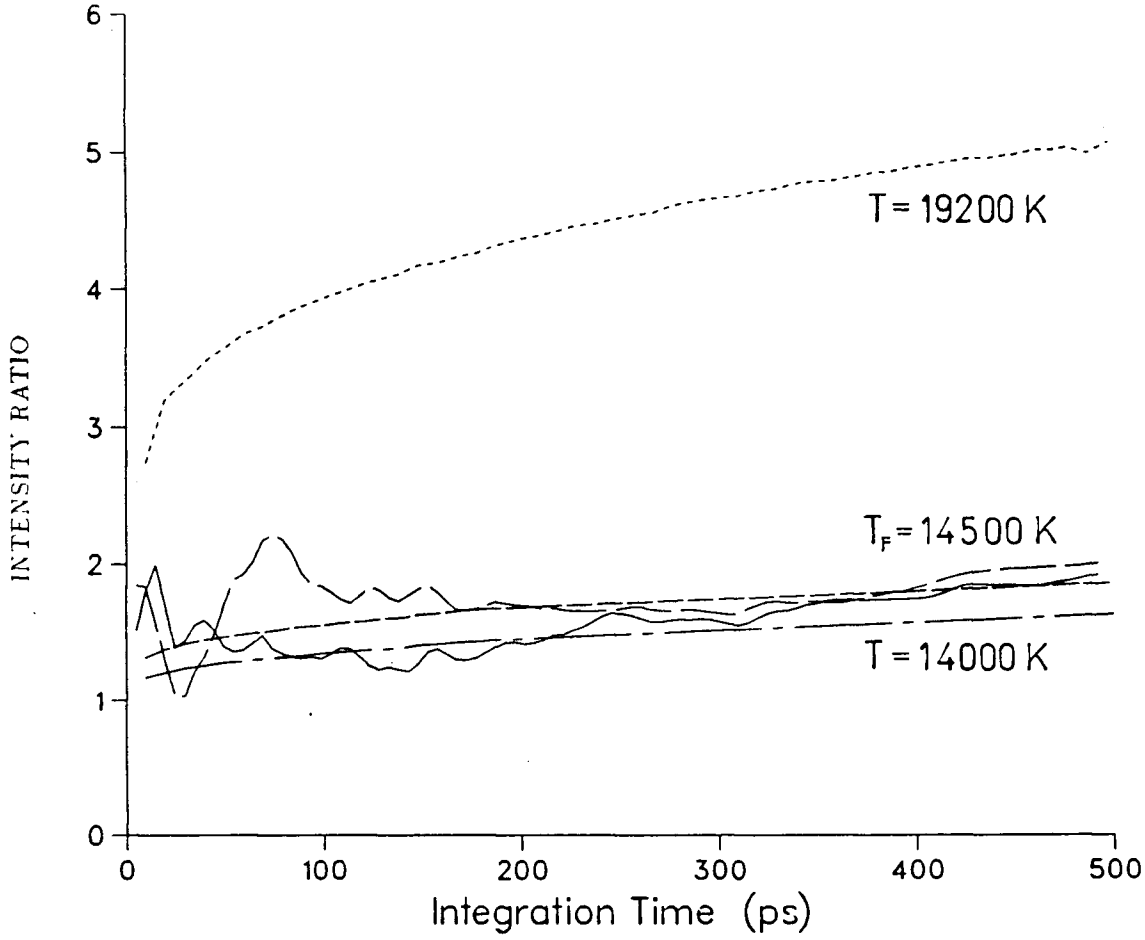


Figure 4.45: Time-integrated emission intensity ratio for a 26.5 $\mu$m Al on 13 $\mu$m Au target to a 38.4 $\mu$m Al target using SESAME (dot), and the new (dot-dash) gold EOS data. One experimental data (long dash) is best-fitted with a shock temperature $T_F$ (short dash) while the other (solid) coincides with the calculated curve (dot-dash).

It can be seen that calculations using the SESAME EOS data for gold seem to overestimate the observed time-integrated intensity ratio, while those using the new EOS for gold appear to be in much closer agreement with experimental observations. Since the latter calculation includes the liquid phase of gold, the melting phenomena is treated in the simulation. The experimental results thus clearly indicate that gold exists in the liquid phase at high pressure. Figure 4.46 shows the Hugoniot of gold from SESAME and that from the new EOS calculations, as well as the deduced shock pressure-temperature points in the studies. These points are obtained as follows. The pressures are the free surface pressures as calculated in the simulations by HYRAD in §4.2.2.A, using the new gold EOS data. They are, respectively, 6.1 Mbar in the 19 $\mu$m Al on 13 $\mu$m Au target, 5.9 Mbar in the 19 $\mu$m Al on 8.4 $\mu$m Au target, 5.5 Mbar in the 26.5 $\mu$m Al on 8.4 $\mu$m Au target, and 5.3 Mbar in the 26.5 $\mu$m Al on 13 $\mu$m Au target. The corresponding temperatures are the best-fitted temperatures to each set of experimental time-integrated intensity ratio curves. The agreement of these experimental points with the liquid Hugoniot is very good.

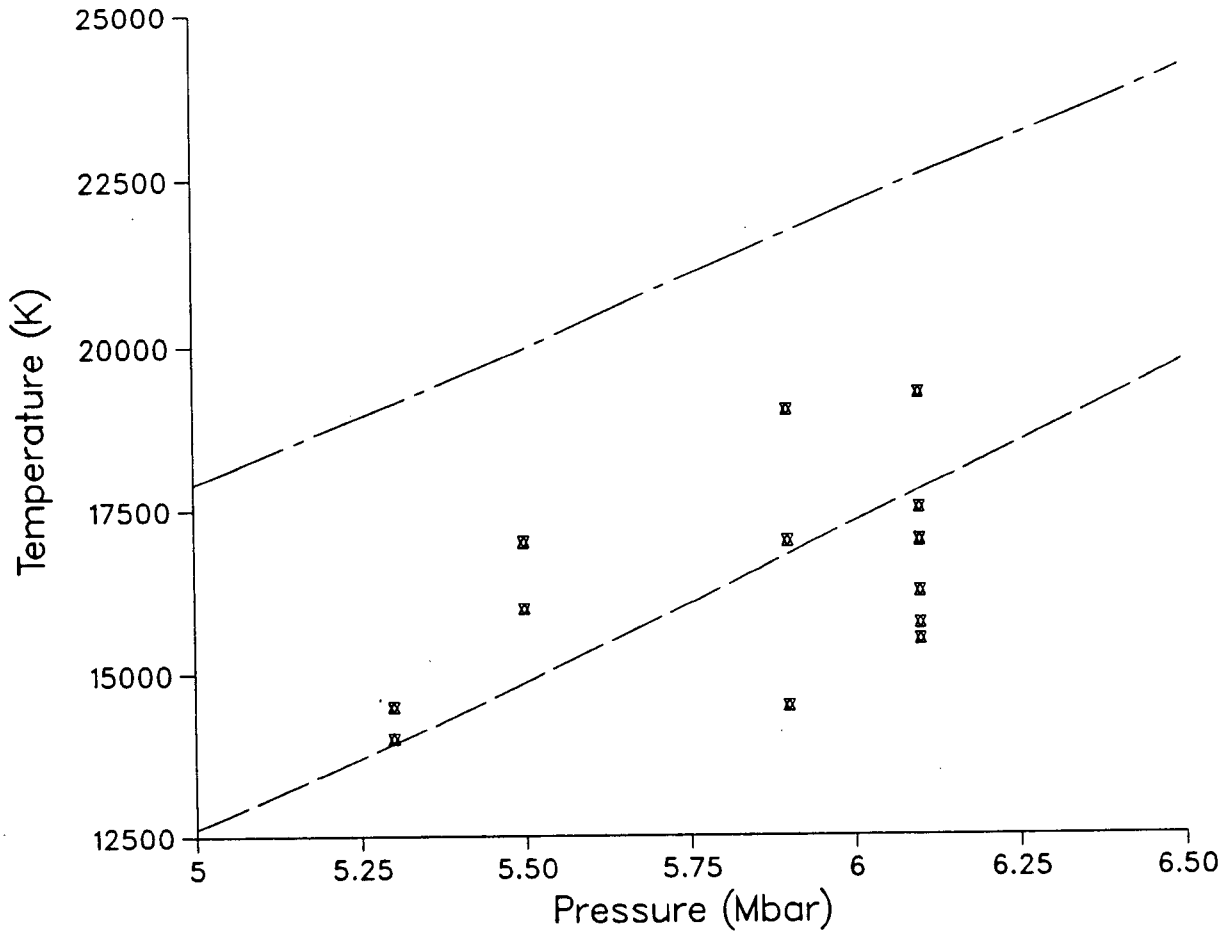


Figure 4.46: A plot of the Hugoniot of gold from SESAME (dot-dash), the liquid Hugoniot in our new calculations (dash) and the experimentally deduced points.

# Chapter 5

# Summary

## 5.1 Conclusions

We will now summarize some of the major results in these laser-driven shock experiments. We have utilized the impedance-mismatch technique to study the properties of shock compressed gold using aluminum as the reference standard. Our studies have involved both experimental measurements and computer simulations of the shock transit through targets of various thicknesses. In particular, the pyrometric technique in which we measure the luminous emission intensity from the free surface of the target is used to to detect the onset time of shock breakout and also to deduce the shock temperature.

We have shown how a proper design of an impedance-mismatched layered target (low-impedance aluminum in front of high-impedance gold) can lead to pressure enhancement and also reduction of radiative preheat in the high-Z gold layer. In addition, the maximazation of the free surface pressure is found to be dependent on the thicknesses of both layers of the target, and that it involves an optimization between an incomplete buildup of the shock when the target is too thin and shock attentuation when the target is too thick. On the other hand, we have shown that the requirement of maximum free surface pressure is not necessarily commensurate with that in high pressure EOS studies, where it is more important to achieve an uniform and steady shock.

In the shock velocity study, we have mapped out the shock trajectory in a target by measuring the shock breakout times in various thicknesses. However, these data are

not accurate enough to discriminate among various equation of state predictions, and are unable to assess the significance of the process of radiation transport in the target. Nonetheless, these simulations have indicated the adequacy of using a one-dimensional and purely fluid code in predicting the shock trajectories. The use of a less complex (hence faster and cheaper to run) hydrocode is of course attractive to those faced with limited computing resources.

In the shock temperature study, we have initiated a new EOS calculation of gold incoporating both solid and liquid state theories, and therefore accounting for shock melting in gold. It is found that the measurement of shock temperature is much more sensitive to the equation of state, in other words, we are able to discriminate between two equation of state predictions. Our measurements of the brightness temperature in gold favor the new EOS prediction over that obtained from the SESAME EOS library where the process of shock melting is absent. In particular, we have found that whereas those simulations using the SESAME EOS have overestimated the time-integrated luminous emission (and hence temperature) of the target rear surface, the simulations using the new gold are in much better agreement with the experimental measurements. We therefore conclude that shock melting of gold has occured. The present measurement of gold (in its liquid phase) at a pressue of $\sim$6 Mbar and $\sim$17500 K represents a first reported measurement of gold under shock melting.

## 5.2 Future Research

A natural extension is to perform impedance-mismatch experiments on high-Z materials other than gold in order to determine their equation of state under shock compression. It is also expected that by using a standard with a lower impedance than that of aluminum, a higher pressure enhancement at the material interface can be attained. Furthermore, triple-layered targets may be considered and their thicknesses optimized to the laser irradiance and pulse condition in order to achieve perhaps still higher pressure and compression. The criterion used here for determining the optimal thickness of a particular layer should still be valid in multi-layered targets, i.e. the thickness of a target layer in front of the interface should be thick enough so that the propagating shocks have time to coalesce into a strong shock front when they reach the interface, and the thickness of the layer behind the interface should be thin enough so that shock damping will not cause the shock to decay significantly when it encounters the free surface (or another interface). Nevertheless, one should also be careful to ensure that the resulting shock profile should be as steady and uniform as possible in order to obtain an unambiguous interpretation of the EOS data.

The brightness temperature study can be extended to involve intensity measurements as a function of wavelength. For example, the peak of the Planck blackbody distribution at these high temperatures (17500 K) is approximately 1650Å, and spectral measurements made at around this wavelength should yield a much higher signal. However, one must then develop an imaging and detector system which is sensitive in this spectral range. In addition, the brightness temperature over a wider range of pressure should be measured so to gain a better understanding of the range of appliability of the theoretical EOS method. It would be especially interesting, for instance, if one can obtain temperature measurements in the pressure range where melting of gold occurs.

## Bibliography


[1] J.Nuckolls, L.Wood, A.Theisson, and G.Zimmerman, Nature **239**, 139 (1972); K.A.Brueckner and S.Jorna, Rev. Mod. Phys. **46**,325 (1974).

[2] J.Duderstadt and G.A.Moses, *Inertial Confinement Fusion* (Wiley & Sons, New York, 1982).

[3] W.J.Nellis, J.A.Moriarty, A.C. Mitchell, M.Ross, R.G.Dandrea, N.W.Ashcroft, N.C.Holmes, and G.R.Gathers, Phys. Rev. Lett. **60**, 1414 (1988).

[4] H.K.Mao, R.J.Hemley, Y.Wu, A.P.Jephcoat, L.W.Finger, C.S.Zha, and W.A.Bassett, Phys. Rev. Lett. **60**, 2649 (1988); or J.S.Olsen, L.Gerward, U.Benedict, S.Dabos, and O.Vogt, Phys. Rev. **B37**, 8713 (1988).

[5] M.Ross, in *High Pressure Chemistry and Biochemistry*, edited by R.van Eldik and J.Jonas (D.Reidel, Dordrecht, 1987), p.9.

[6] M.Ross, F.H.Ree, and D.A.Young, J.Chem. Phys. **79**, 1487 (1983).

[7] H.B.Radousky and M.Ross, Phys. Let. A **129**, 43 (1988).

[8] A.M.Bratkovsky, Phys. Let. A **130**, 151 (1988).

[9] J.W.Shaner, in *Physics of Solids under High Pressure*, edited by J.S.Schilling and R.N.Shelton (North-Holland, Amsterdam, 1981), p.93.

[10] V.E.Fortov, Sov. Phys. Usp. **25**, 781 (1982).

[11] A.Jayaraman, Rev. Mod. Phys. **55**, 65 (1983).

[12] J.M.Walsh and R.H.Christian, Phys. Rev. **97**, 1544 (1955).

[13] M.H.Rice, R.G.McQueen, and J.M.Walsh, Solid St. Phys. **6**, 1 (1958).

[14] R.G.McQueen and S.P.Marsh, J. Appl. Phys. **31**, 1253 (1960); and **33**, 654 (1962).

[15] L.V.Al'tshuler, K.Krupnikov, B.Ledenev, V.Zhuchikhin, and M.Brazhnik, Sov. Phys. JETP **7**, 606 (1958); L.V.Al'tshuler, S.B.Kormer, A.A.Bakanova, and R.F.Trunin, Sov. Phys. JETP **11**, 573 (1960); L.V.Al'tshuler, A.A.Bakanova, and R.F.Trunin, Sov. Phys. JETP **15**, 65 (1962); for a summary article, see L.V.Al'tshuler, Sov. Phys. Usp. **8**, 52 (1965).

[16] L.V.Al'tshuler, B.N.Moiseev, L.V.Popov, G.V.Simakov, and R.F.Trunin, Sov. Phys. JETP **27**, 420 (1968).

[17] C.E.Ragan III, M.G.Silbert, and B.C.Diven, J. Appl. Phys. **48**, 2860 (1977); C.E.Ragan III, Phys. Rev. **A21**, 458 (1980), **A25**, 3360 (1982); and **A29**, 1391 (1984).

[18] W.J.Nellis and A.C.Mitchell, J. Chem. Phys. **73**, 6137 (1980); A.C.Mitchell and W.J.Nellis, J. Appl. Phys. **52**, 3363 (1981).

[19] R.Arnold, Nature **276**, 19 (1978); for a recent review, see R.Arnold and J.Meyer-ter-Vehn, Rep. Prog. Phys. **50**, 559 (1987).

[20] for a recent review article, see S.I.Anisimov, A.M.Prochorov, and V.E.Fortov, Sov. Phys. Usp. **27**, 181 (1984);
for the laser option in ICF, see T.H.Johnson, Proc. IEEE **72**, 548 (1984).

[21] A.S.Vladimirov, N.P.Voloshin, V.N.Nogin, A.V.Petrovtsev, and V.A.Simonenko, Sov. Phys. JETP Lett. **39**, 82 (1984).

[22] W.J.Nellis, in *High Pressure Measurement Techniques*, edited by G.N.Peggs (Appl. Sciences, New York, 1983), p.69.

[23] N.Metzler and J.Meyer-ter-Vehn, Laser & Particle Beams **2**, 27 (1984).

[24] R.J.Trainor, J.W.Shaner, J.M.Auerbach and N.C.Holmes, Phys. Rev. Lett. **42**, 1154 (1979).

[25] F.Cottet, M.Hallouin, J.P.Romain, R.Fabbro, B.Faral, and H.Pepin, Appl. Phys. Lett. **47**, 678 (1985).

[26] see for example, P.D.Goldstone, R.F.Benjamin, and R.B.Shultz, Appl. Phys. Lett. **38**, 223 (1981);
C.Garban-Labaune, E.Fabre, C.E.Max, R.Amiranoff, J.Virmont, M.Weinfeld, and A.Michard, Phys. Rev. Lett. **48**, 1018 (1982);
W.Seka, R.S.Craxton, J.Delettrez, L.Goldman, R.Keck, R.L.McCrory, D.Shvarts, J.M.Soures, and R.Boni, Opt. Commun. **40**, 437 (1982);
R.J.Trainor, N.C.Holmes, R.A.Anderson, E.M.Campbell, W.C.Mead, R.J.Olness, R.E.Turner, and F.Ze, Appl. Phys. Lett. **43**, 542 (1983).

[27] R.Malone, R.L.McCrory, and R.L.Morse, Phys. Rev. Lett. **34**, 721 (1975).

[28] W.D.Phillion, E.M.Campbell, K.G.Estabrook, R.A.Lerche, G.E.Philips, and F.Ze, Phys. Rev. Lett. **49**, 1405 (1982).

[29] W.C.Mead, E.M.Campbell, K.G.Estabrook, R.W.Turner, W.L.Kruer, P.H.Y.Lee, B.Pruett, V.C.Rupert, K.G.Tirsell, G.L.Stradling, F.Ze, C.E.Max, and M.D.Rosen, Phys. Rev. Lett. **47**, 1289 (1981).

[30] L.R.Vesser, J.Solem, and A.Lieber, Appl. Phys. Lett. **35**, 761 (1979).

[31] V.N.Mineev and A.G.Ivanov, Sov. Phys. Usp. **19**, 400 (1976).

[32] A.Ng, D.Parfeniuk, P.Celliers, L.Da Silva, R.More and Y.T.Lee, Phys. Rev. Lett. **57**, 1595 (1986).

[33] J.S.Wark, R.R.Whitlock, A.Hauer, J.E.Swain and P.J.Solone, Phys. Rev. **B35**, 9391 (1987).

[34] D.K.Bradley, J.Kilkenny, S.J.Rose, and J.D.Hares, Phys. Rev. Lett. **59**, 2995 (1987).

[35] T.A.Hall, A.Djaoui, R.W.Eason, C.L.Jackson, B.Shiwai, S.L.Rose, A.Cole, and P.Apte, Phys. Rev. Lett. **60**, 2034 (1988).

[36] S.B.Kormer, M.V.Sinitsyn, G.A.Kirillov, and V.D.Urlin, Sov. Phys. JETP **21**, 689 (1965); S.B.Kormer, Sov. Phys. Usp. **11**, 229 (1968).

[37] D.A.Young and M.Ross, Phys. Rev. **B29**, 682 (1984);
J.A.Moriarty, D.A.Young and M Ross, Phys. Rev. **B30**, 578 (1984).

[38] R.G.McQueen, J.N.Fritz, and C.E.Morris, in *Shock Waves in Condensed Matter - 1983 Proceedings of the APS topical conference, Santa Fe*, (North-Holland, Amsterdam, 1984), p. 95.

[39] H.B.Radousky, M.Ross, A.C.Mitchell, and W.J.Nellis, Phys. Rev. **B31**, 1457 (1985).

[40] P.Mora, Phys. Fluids **25**, 1051, (1982).

[41] K.Eidmann, F.Amiranoff, R.Fedosejevs, A.G.M.Maaswinkel, R.Petsch, R.Sigel, G.Spinder, Y.L.Teng, G.Tsakiris, and S. Witkowski, Phys. Rev. **A30**, 2568 (1984).

[42] L.Spitzer and R.Härm, Phys. Rev. **89**, 977 (1953); L.Spitzer, *Physics of Fully Ionized Gases*, 2nd ed. (Interscience, New York, 1962).

[43] C.E.Max, C.F.McKee, and W.C.Mead, Phys. Fluids **23**, 1620 (1980).

[44] F.C.Young, R.R.Whitlock, R.Decoste, B.H.Ripin, D.J.Nagel, J.A.Stamper, J.M.McMahon, and S.E.Bodner, Appl. Phys. Lett. **30**, 45 (1977).

[45] D.Shvarts, J.Delettrez, R.L.McCrory, and C.P.Verdon, Phys. Rev. Lett. **47**, 247 (1981).

[46] M.A.Stroscio, Opt. Commun. **21**, 267 (1977).

[47] B.K.Godwal, S.K.Sikka, and R.Chidambaram, Phys. Rep. **102**, 121 (1983).

[48] M.Ross, Rep. Prog. Phys., **48**, 1 (1985).

[49] A.Ng, D.Parfeniuk, and L.Da Silva, Phys. Rev. Lett. **54**, 2604 (1985).

[50] SESAME EOS is from Los Alamos National Laboratory. see e.g. J.Abdallah, R.C.Albers, B.I.Bennett, F.Dowell, B.L.Holian, W.F.Huebner, J.D.Johnson, D.A.Liberman, S.P.Lyon, G.K.Straub, and K.S.Trainor, LANL Report No.83-4, 1983; K.S.Holian, editor., LANL Report No.LA-10160-MS, Vol.1C. 1984. The aluminum data are taken from material table 3715, and gold data from material table 2700.

[51] A.P.French, *Vibrations and Waves* (Norton, New York, 1973), Chapter 8.

[52] N.L.Hickerson, in *High-Velocity Impact Phenomena* , edited by R.Kinslow (Academic, New York, 1970), p.23.

[53] N.C.Holmes, R.J.Trainor, R.A.Anderson, L.R.Vesser, and G.A.Reeves, in *Shock Waves in Condensed Matter*, edited by W.J.Nellis, L.Seaman, and R.D.Graham (AIP, New York, 1982), p.160.

[54] D.Salzmann, S.Eliezer, A.Krumbein, and L.Gitter, Phys. Rev. **A28**, 1738 (1983).

[55] A.Ng, Y.Gazit, F.P.Adams, D.Parfeniuk, P.Celliers, and L.Da Silva, Plasma Phys. & Cont. Nul. Fus. Res. **3**, 187 (1986).

[56] J.Mizui, N.Yamaguchi, and S.Tagaki, J. Quant. Spect. Rad. Trans. **27**, 253 (1982).

[57] E.A McLean, S.H.Gold, J.A.Stamper, R.R.Whitlock, H.R.Griem, S.P.Obenschain, B.H.Ripin, S.E.Bodner, M.J.Herbst, S.J.Gitomer, and M.K.Matzen, Phys. Rev. Let. **45**, 1246 (1980).

[58] D.Duston, R.W.Clark, J.Davis, and J.P.Apruzese, Phys. Rev. **A27**, 1441 (1983).

[59] H.R.Griem, *Plasma Spectroscopy* (McGraw-Hill, New York, 1964).

[60] R.C.Mancini and C.F.Hooper Jr.,J. Phys. D: Appl. Phys. **21**, 1099 (1988).

[61] R.F.Schmalz, J.Meyer-ter-Vehn, and R.Ramis, Phys. Rev. **A34**, 2177 (1986).

[62] Ya.B.Zel'dovich and Y.P.Raizer, *Physics of Shock Waves and High-Temperature Hydrodynamic Phenomena* (Academic, New York, 1966), Vol.II, Chap.11.

[63] J.F.Barnes, Phys. Rev. **153**, 269 (1967).

[64] R.D.Cowan and J.Ashkin, Phys. Rev. **105**, 144 (1957); for a general review of the TFD model, see A.K.Ghatak and S.Eliezer, Laser & Particle Beams **2**, 309 (1984).

[65] N.W.Ashcroft and N.D.Mermin, in *Solid State Physics* (Saunders College, Philadelphia, 1976), Chapter 38.

[66] F.J.Rogers and H.E.DeWitt, Phys. Rev. **A8**, 1061 (1973); F.Rogers, Phys. Rev. **A10**, 2441 (1974).

[67] D.A.Young, LLNL Report, UCRL-52352 (1977).

[68] C.A.Rouse, Astrophys. J. **136**, 636 (1962).

[69] R.Grover, in *Proceedings of the Seventh Symposium on Thermodynamic Properties*, edited by A.Cezairliyan (ASME, New York, 1977), p.67; R.Grover, J. Chem. Phys. **55**, 3435 (1971).

[70] J.S.Dugale and D.K.MacDonald, Phys. Rev. **89**, 832 (1953).

[71] F.A.Lindemann, Phys. Z. **11**, 609 (1910); for a modern derivation, see M.Ross, Phys. Rev. **189**, 233 (1969).

[72] see for example, T.L.Loucks, *Augmented Plane Wave Method* (Benjamin, New York, 1967).

[73] S.L.MaCarthy, LLNL Report, UCRL-14362 (1965).

[74] D.A.Kirzhnitz, Y.E.Lozovik, and G.V. Shpatakovskaya, Sov. Phys.-Usp. **18**, 649 (1976).

[75] F.Ree, D.Daniel and G.Haggin, LLNL Internal Document, HTN-291 (1978).

[76] M.Ross, Phys. Rev. **B21**, 3140 (1980).

[77] O.K.Anderson and O.Jepsen, Physica **B91**, 317 (1977); O.K.Andersen, Phys. Rev. **B12**, 3060 (1975); O.K.Andersen and R.V.Kasowski, Phys. Rev. **B4**, 1064 (1971); R.V.Kasowski and O.K.Andersen, Solid State Commun. **11**, 799 (1972). For computation uses,see H.L.Skriver, *The LMTO Method* (Springer-Verlag, New York, 1984).

[78] P.Hohenberg and W.Kohn, Phys. Rev. **136**, B864 (1964);
W.Kohn and L.J.Sham, Phys. Rev. **140**, A1133 (1965).

[79] U. von Barth and L Hedin, J. Phys. C **5**, 1629 (1972).

[80] D.Glötzel and A.K.McMahan, Phys. Rev. **B20**, 3210 (1979).

[81] S.K.Sikka and B.K.Godwal, Phys. Rev. **B35**, 1446 (1987).

[82] G.I.Kerly, J. Chem. Phys. **73**, 469 and 478 (1980).

[83] H.Brysk, P.M.Campbell, and P.Hammerling, Plasma Phys. **17**, 473 (1975).

[84] L.Marty, These de l'Universite de Poitiers, France ,1988 (unpublished).

[85] D.Parfeniuk, Ph.D. Thesis, U.B.C. ,1987 (unpublished).

[86] Ya.B.Zel'dovich and Y.P.Raizer, *Physics of Shock Waves and High-Temperature Hydrodynamic Phenomena* (Academic, New York, 1966), Vol.I, Chap.3 and Vol.II, Chap.7.

[87] R.D.Richtmyer and K.W.Morton, *Difference Methods for Initial Value Problems*, (Interscience, New York, 1967).

[88] J.von Neumann and R.D.Richtmyer, J. Appl. Phys. **21**, 232 (1950).

[89] P.Celliers, Ph.D. Thesis, U.B.C. ,1988 (unpublished).

[90] L.Da Silva, Ph.D. Thesis, U.B.C. ,1988 (unpublished).

[91] J.P.Christiansen, D.E.Ashby, and K.Roberts, Comp. Phys. Commun. **7**, 271 (1974).

[92] D.R.Bates, A.E.Kingston, and R.W.P.McWhirter, Proc. R. Soc. (Lond.) **A267**, 297 (1962); and **A270**, 155 (1962).

[93] see for example, D.Duston, Can. J. Phys. **64**, 998 (1986); M.Busquet, Phys. Rev. **A25**, 2302 (1982); S.Atzeni, Plasma Phys. and Contr. Fusion **29**, 1535 (1987).

[94] M.J.Seaton, in *Atomic and molecular processes*, edited by D.R.Bates (Academic, New York, 1962), p.374.

[95] L.Da Silva, A.Ng, B.K.Godwal, G.Chiu, F.Cottet, M.Richardson, P.Jannimagi, and Y.T.Lee, submitted for pub.

[96] A.Ng, P.Celliers, and D.Parfeniuk, Phys. Rev. Lett., **58**, 214 (1987).

[97] P.Colella and P.R.Woodward, J. Comp. Phys. **54**, 174 (1984).

[98] S.K.Godunov, Mat. Sb. **47**, 271 (1959).

[99] P.R.Woodward and P.Colella, J. Comp. Phys. **54**, 115 (1984).

[100] C.E.Max, in *Laser Plasma Interaction*, edited by R.Balian and J.C.Adam (North-Holland, Amsterdam, 1982) p.301.

[101] T.Mochizuki, T.Yabe, K.Okada, M.Hamada, N.Ikeda, S.Kiyokawa, and C.Yamanaka, Phys. Rev. **A33**, 525 (1986).

[102] R.Marchand, C.E.Capjack, and Y.T.Lee, Phys. Fluids **31**, 949 (1988); and R.Marchand, R.Fedoseyevs, C.E.Capjack, and Y.T.Lee, Laser & Particle Beams, **6**. 183 (1988).

[103] D.Duston, R.W.Clark, and J.Davis, Phys. Rev. **A31**, 3320 (1985).

[104] D.Salzmann, H.Szichmann, A.D.Krumbein and C.E.Capjack, Phys. Fluids **30**, 515 (1987).

[105] Ya.B.Zel'dovich and Y.P.Raizer, *Physics of Shock Waves and High-Temperature Hydrodynamic Phenomena* (Academic, New York, 1966), Vol.I, Chap.2.

[106] Gentec joulemeter, Model ED-200, calibrated at 8.52 V/J, S/N=19874, manufactured by Gentec Inc., 2625 Dalton St., Ste-Foy, Quebec, Canada.

[107] Hamamatsu photodiode, Model R1193U, with 350 ps rise time.

[108] Hamamatsu Corp., 420 South Ave., Middlesex, NJ 08846.

[109] A.Ng, D.Parfeniuk, L.Da Silva, and D.Pasini, Phys. Fluids **28**, 2915 (1985).

[110] D.Pasini, Ph.D. Thesis, U.B.C., 1984 (unpublished).

[111] M.H.Key, Phil. Trans. R. Soc.London A, **300**, 599 (1981).

[112] A.Ng, F.Cottet, L.Da Silva, G.Chiu, and A.R.Piriz, Phys. Rev. A, (accepted for publication).

[113] Goodfellow Metal Ltd., Cambridge Science Park Milton Road, Cambridge, England.

[114] T.C.Kaushik and B.K.Godwal, Phys. Rev. **A36**, 5095 (1987).

[115] F.V.Grigoriev, S.B.Kormer, O.L.Mikhailova, M.A.Mochalov, and V.D.Urlin, Sov. Phys. JETP **61**, 751 (1985).

[116] L.Da Silva, A.Ng, and D.Parfeniuk, J. Appl. Phys. **58**, 3634 (1985).